Etude des systèmes $\eta\pi^(0)$ et $\eta\pi^(-)$ formés dans les réactions de production centrale

Andrei E. Sobol

Institute for High Energy Physics (IHEP)
and
Institut National de Physique Nucléaire et de Physique des Particules (IN2P3)
Laboratoire d'Annecy-le-vieux de Physique des Particules (LAPP)

Andrei E. Sobol

A study of the centrally produced $\eta\pi^o$ and $\eta\pi^-$ systems in pp interactions

Doctor thesis

Protvino – Annecy-le-Vieux
2001

Contents

List of Figures

List of Tables

Chapter 1

Introduction

Our modern understanding of the structure of matter is reflected in the Standard Model. According to this model the hadron matter consists of quarks (q) and gluons (g). The interactions of quarks and gluons are described by the quantum field theory which is called Quantum Chromodynamics (QCD). Two basic groups of hadrons are mesons ($q\bar{q}$) and baryons (qqq). Pursuant to the quantum numbers, isospin I, spin J, space P and charge C parity, they are classified into multiplets according to group theory. Mathematically QCD is a non-Abelian theory, physically it means a capability of gluon-gluon interactions and the formation of new types of hadrons: glueballs ($2g$, $3g$, ...). QCD also predicts the existence of hybrids ($q\bar{q}g$), fourquark states $q\bar{q}q\bar{q}$ and molecules consisting of two hadrons, for example, $K\bar{K}$. All these objects are called exotic. The purposes of the hadron spectroscopy are the detection of hadron states, both exotic and ordinary, measurements of their quantum numbers, studies of their inner structure, mechanisms of production and lastly their classification.

The searches for the exotic hadron states encounter some difficulties. It is enough to mention that while the basic meson and baryon multiplets are already practically filled, there are no exotic state which has been strictly proved. Only the last few years of intensive experimental studies in this area have led to the observation of some candidates which we can refer to as exotic with a greater degree of confidence. The problem consists in separating ordinary and exotic particles because the masses of the exotic states predicted by the theory and by the numerical calculations lie in the same region as the masses of the ordinary mesons, and physicists do not have many criteria for their separation. Let's enumerate the main ones.

1. At first, it is a direct observation of resonant states with quantum numbers which are impossible for $q\bar{q}$. It is known that $q\bar{q}$ states with the orbital moment l and a spin s should have a spin-parity $P = (-1)^{(l+1)}$ and a charge parity $C = (-1)^{(l+s)}$. So the states with quantum numbers $J^{PC} = 0^{-}, 0^{+-}, 1^{-+}, 2^{+-}, ...$ cannot belong to mesons and hence they are exotic. This way is the most reliable: if we find a resonance with such quantum numbers, we have no doubt that it is an exotic state. However, exotic particles, e.g. glueballs, can have the same quantum numbers as ordinary states. They can be recognised indirectly.

2. Observation of extra-particles in already filled multiplets. For example, in the framework of the naive quark model only four $J^{PC} = 0^{+}0^{++}$ states can exist: two in the lowest and two in the first radially excited state. 5 scalar resonances are observed experimentally. According to the predictions of the theoretical models, one of them should be the lightest glueball.

3. As glueballs do not bear an electric charge they cannot decay to a pair of photons directly. The process can go only through a $q\bar{q}$ exchange. It has 2 vertices and therefore is strongly supressed, as well as the reverse process $\gamma\gamma \rightarrow q\bar{q} \rightarrow gg$. Therefore, if the resonance is produced in two-photon interactions then it is most likely not a glueball.

4. The probability of the glueball decay to quarks should be identical for miscellaneous quarks accurate to phase space, that is incorrect for mesons. The typical example is the pair of vector mesons $\omega(782)$ and $\phi(1020)$. $\phi(1020)$ decays to $K\bar{K}$ well (83%) and to $\pi\pi\pi$ (16%) poorly, vice-versa $\omega(782)$ decays to $\pi\pi\pi$ (89%) predominantly. It is explained by the quark structure of these mesons: $\phi(1020)$ is a clean $s\bar{s}$ state, while $\omega(782)$ consists of a mixing of u and d quarks: $u\bar{u} + d\bar{d}$.

5. Exotic particles containing valence gluons, i.e. hybrids and glueballs, should have matrix elements of decays to η' meson larger than to η due to the stronger connection of the η' with the gluon [17]. The same is true for decays to channels with η and π mesons: the decay to η for the hybrid or the glueball is more

preferential. Measuring relative probabilities of decays, for example, to $\pi\pi$, $\eta\eta$, $\eta\eta'$, $\eta'\eta'$ we can estimate the contribution of the gluon component in exotic states.

There is a number of processes where the exotic states containing valence gluons are produced more intensively than in other ones. The diagrams of these processes are shown in the figure 1.1. Let's discuss them.

1. J/ψ decays, 1.1(a,c), have a limited number of channels and so a low level of background processes.

2. The central production in the proton-proton interactions 1.1(b) is realized by the exchange of two virtual particles. The intensity of Pomeron-Pomeron exchange increases in comparison with Reggeon-Pomeron and Reggeon-Reggeon vs energy. The nature of Pomeron is still unknown but it is supposed that this Regge trajectory is formed by two or more gluons. So double Pomeron exchange is expected to be a gluon rich channel.

3. The proton-antiproton annihilation 1.1(d) can also be a source of glueballs.

4. Some hadron reactions taking place with OZI-rules violation[1]. In the figure 1.1(e) one such reaction is shown: the production of the $\phi\phi$ system goes through the intermediate state containing gluons.

The work presented in this thesis was made on the experimental data obtained by the WA102 Collaboration studying reactions of the central production in the proton-proton collisions:

$$pp \to p_f X^o p_s, \tag{1.1}$$

where the indices f and s mean fastest and slowest particles in the laboratory system, X^o is the central particle. The X^o is produced in the interaction of two exchanged particles (see fig.1.1(b)) which can be Reggeons (R) or Pomerons (P). The experiment WA102 was performed at incident beam momentum 450 GeV/c that corresponds to $\sqrt{s} = 29$ GeV. Before, the reaction 1.1 was studied by the experiments WA76 and WA91 at momentums 85 and 300 GeV/c ($\sqrt{s} = 12.7$ and 23.8 GeV). There are

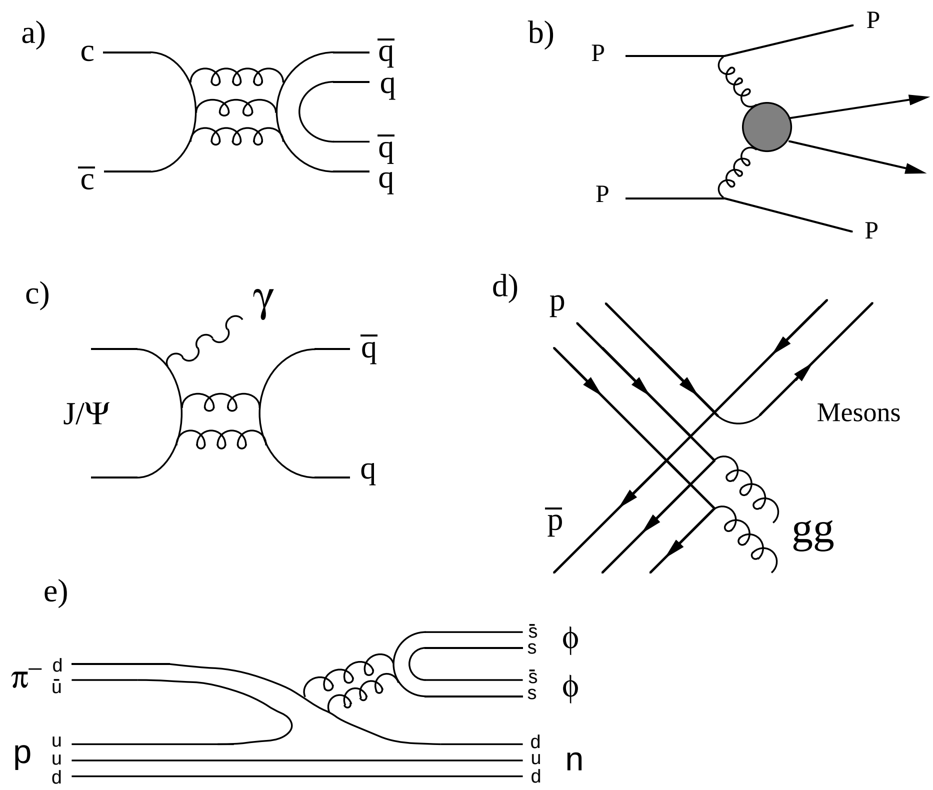

Figure 1.1: Diagrams of gluon rich channels.

theoretical predictions [2] for intensities of different types of exchange depending on the centre of mass energy 1.1:

$$\begin{aligned} \sigma(RR) &\sim s^{-1}, \\ \sigma(RP) &\sim s^{-0.5}, \\ \sigma(PP) &\sim \mathit{constant}, \end{aligned} \tag{1.2}$$

where RR, RP and PP mean respectively Reggeon-Reggeon, Reggeon-Pomeron and Pomeron-Pomeron exchanges. Equations 1.2 show that the contribution of the double Pomeron exchange in relation to the Reggeon-Reggeon and Pomeron-Pomeron exchanges in the cross-section of reaction 1.1 increases with the increase of energy. So the production of central resonances with gluon component also increases. The results obtained by the experiments WA76, WA91 and WA102 at different energies confirm the theoretical predictions 1.2 [3]. For example, the production of $\rho^o(770)$, which has an isospin 1 and cannot be produced in a double Pomeron exchange, decreases with the increase of s. Thus the $\eta'(958)$ production does not depend on s, that can be explained naturally by the production of this meson in a double Pomeron exchange.

In the last few years the WA102 Collaboration has performed an intensive experimental programme which has produced a large and detailed data set in the meson spectroscopy [4]. Many new results have been obtained, in particular, efforts have been made to find new kinematic variables which could separate states with a strong gluon component from ordinary mesons. Two interesting effects observed by the Collaboration should be developed.

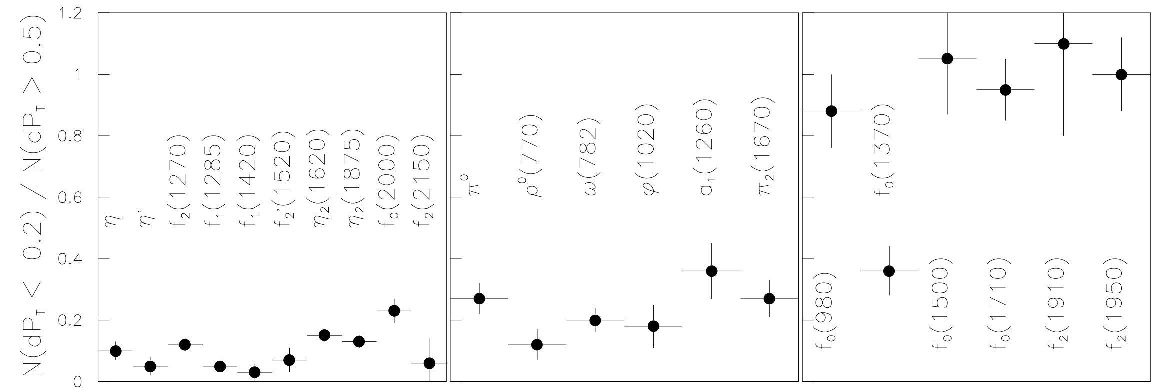

Figure 1.2: The ratio R of the production cross-section for the small dP_T (≤ 0.2 GeV) and large dP_T (≥ 0.5 GeV) for different resonances.

<u>**Glueball-filter.**</u> In the work [5] it was proposed to analyse the data at different values of the kinematic variable dP_T, representing the difference between the transverse momentum vectors of the exchanged particles[1]. The Collaboration obtained the ratio R of the production cross-section for the small (≤ 0.2 GeV) and large dP_T (≥ 0.5 GeV) for different resonances [4]. It was observed that all studied resonances can be separated into 3 groups according to R. The values of R for different resonances are shown in the figure 1.2. It is interesting to note that all undisputed $q\bar{q}$ state, namely those with positive G parity and $I = 0$, have a very small value for this ratio (≤ 0.1). Some of the states with $I = 1$ or negative G parity, which cannot be produced by double Pomeron exchange, have a slightly higher value (≈ 0.25). All the states which can be considered as candidates for glueballs have a large value for this ratio, close

[1] $dP_T = \sqrt{(P_1^x - P_2^x)^2 + (P_1^y - P_2^y)^2}$, where P_1 and P_2 are the momenta of the exchanged particles.

to 1. This effect, the so-called "glueball-filter", has not had a convincing theoretical explanation until now. Only one theoretical work [6] had been published, in which the attempt was made to qualitatively explain the phenomenon.

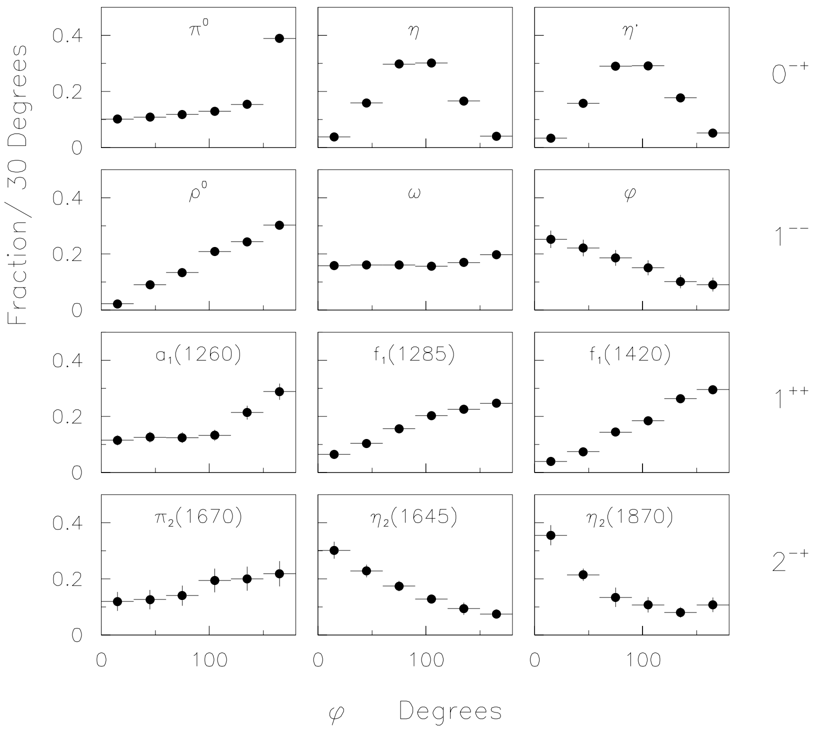

Figure 1.3: Azimuthal angle ϕ between the transverse momentum vectors for outgoing protons for resonances with $J^{PC} = 0^{-+}, 1^{--}, 1^{++}$ and 2^{-+}.

Effect of a non-flat azimuthal angle. In the work [4] an interesting behaviour of the azimuthal angle ϕ between the transverse momentum vectors of the outgoing protons was observed. Naively, it would be expected that this angle should be flat irrespective of the resonances produced. The experimentally observed ϕ dependences are clearly non-flat and considerable variations are found between resonances with different J^{PC}. Figure 1.3 shows the ϕ-dependences for several studied resonances. Several theoretical papers have been published on the ϕ-dependence [7, 8]. All agree that the exchanged particle (it can be Pomeron) must have $J > 0$ and that $J = 1$ is the simplest explanation. Using $\gamma\gamma$ collisions as an analogy, Close and Schuler have calculated the ϕ and t^2 dependences for the production of resonances with different

[2] t is the transverse momentum squared between the incoming and outgoing protons.

J^{PC} [8]. In their model of double Pomeron exchange the Pomeron acts as a non-conserved vector current. In the work [9] this model was tested for some resonances with $J^{PC} = 0^{-+}, 1^{++}, 2^{-+}, 0^{++}, 2^{++}$. A good description of the experimental data was obtained.

Purposes of the thesis

The work presented in this thesis was made within the framework of the experiment WA102 whose purposes were the study of all kinematically accessible resonances formed in central pp collisions at 450 GeV, the search of exotic states, the analysis of the interesting kinematical variables, in particular, dP_T, ϕ and t dependences for different resonances, which could help to separate exotic states and give the information about the Pomeron nature. The purpose of this work was the study of the $\eta\pi^0$ production in the central pp collisions:

$$pp \to p_s(\eta\pi^0)p_f \tag{1.3}$$

with the subsequent decays $\eta \to 2\gamma$ and $\pi^0 \to 2\gamma$, and the $\eta\pi^-$ production:

$$pp \to p_s(\eta\pi^-)\Delta^{++}(1232), \tag{1.4}$$

with the subsequent decays $\eta \to 2\gamma$ and $\Delta^{++}(1232) \to p_f\pi^+$. In the framework of this study a partial-wave analysis in the model of S, P, D waves has been performed, where the P wave has the exotic quantum numbers $J^{PC} = 1^{-+}$. Furthermore the measurements of dP_T, ϕ and t dependences have been made for the resonances in the $\eta\pi^0$ and $\eta\pi^-$ systems.

The scientific novelty of the thesis

As it will be discussed in the chapter 2 the analysis of the $\eta\pi$ system has a long history and causes a special interest in connection with the observation of exotic waves in this system. However, in the central pp collisions, which should have high production of particles with gluon component, the $\eta\pi$ system was not investigated in detail. Actually a mass spectrum of the $\eta\pi^0$ system was only obtained [38]. In this work the $\eta\pi^-$ system is studied in central pp interactions for the first time. The partial-wave analysis of the $\eta\pi^-$ and $\eta\pi^0$ systems in these reactions are also performed for the first time. The number of experimental events in this study is more than the double of those in the previous works. Also for the first time the ratios of the $a_0(980)$ and $a_2(1320)$ cross-sections in reactions 1.3 and 1.4 are obtained that allow some conclusions to be made about the dynamics of the resonances production in the central pp collisions.

The practical significance of the thesis

A technique of events selection for the reactions 1.3 and 1.4 is designed. It is based on the computer program of the kinematical data analysis which can also be applied to the analysis of other reactions. A set of programs for the partial-wave analysis for the systems with two pseudoscalar mesons produced in the central pp collisions is created. All basic algorithms, beginning with the approximation of multidimensional efficiency and finishing with calculations of all nontrivial solutions for the partial-wave analysis are realised in these programs.

The structure of the thesis

The thesis consists of the 8 chapters and the conclusion, including 67 figures and 11 tables. The first chapter gives the introduction to the thesis. In the second chapter a historical review of the $\eta\pi$ study is given for different reactions and experimental groups. A special emphasis is given to the last activities dedicated to the searches of the exotic 1^{-+} state. Also is discussed the present status of the $a_0(980)$ resonance and the discovery of new particles in the $\eta\pi$ system: the isovector scalar $a_0(1450)$ and the tensor $a_2(1650)$.

In the third chapter the setup of the WA102 experiment and the organization of the trigger are described, and a brief description of tracks and γ reconstruction is given.

In the fourth chapter the theoretical foundations for the analysis is described: the procedure of the kinematical analysis, the procedure of the efficiency calculation by a Monte-Carlo method and the approximation of the efficiency by Fourier series. A theoretical basis of the partial-wave analysis of two pseudoscalar mesons in central pp collisions is presented using a model of S, P and D waves. The ambiguity problem in this analysis and the procedure for calculations of all unambiguous solutions are described in detail. Also the procedure of the angular distribution fit is described, and the functionals are adduced.

The fifth and sixth chapter are respectively dedicated to the analysis of the reactions 1.3 and 1.4. Events selection, background, results of the partial-wave analysis are presented. The parameters of the resonances, their relative cross-sections and dP_T, ϕ and t dependences are obtained.

In the seventh chapter the obtained results are discussed, in particular, the mixing between the $a_0(980)$ and $f_0(980)$ resonances through the intermediate $K\bar{K}$ state is suggested for the explanation of the different $a_0(980)$ and $a_2(1320)$ relative cross-sections in the reactions 1.3 and 1.4.

In the eighth chapter a further study of central production in pp collisions is proposed at energies of LHC (CERN) in the experiment CMS. The possible setup of the experiment and the organization of the trigger is described, the results of the numerical calculations by a Monte-Carlo method for some decay channels of the central particle are presented, the backgrounds are estimated.

In the conclusion the main results of the thesis are listed.

Chapter 2

History of the $\eta\pi$ study

The history of the $\eta\pi$ system study spans more than three decades. Its origins lie in the bubble chambers experiments at the end of the sixties. In 1968 two experimental groups from CERN[1] and ANL[2] reported the observation of a narrow resonance with a mass 980 MeV in the mass spectrum of the η and $\pi^-(\pi^+)$ mesons. Both groups have used liquid hydrogen bubble chambers for their research. A group of European scientists worked on the CERN-PS beam studied the reaction of the proton-antiproton annihilation $p\bar{p} \to \eta 2\pi^+ 2\pi^-$ [10]. Some american physicists studied the charge exchange reaction $K^- p \to \Lambda\eta\pi^+\pi^-$ [11]. The observed particle was associated with the one observed earlier in the $K\bar{K}$ σ resonance [12]. Now this particle is called $a_0(980)$. These two works became the first in a long series of published research.

Fixing a system of two particles for its analysis, the experimental physicist defines thus the quantum numbers I^G of this system. For two pseudoscalar mesons, η and π, $I^G = 1^-$. The set of possible J^{PC} states is also fixed, according to the conservation laws. In the $\eta\pi$ system, states with the following quantum numbers are possible: $J^{PC} = 0^{++}, 1^{-+}, 2^{++}, 3^{-+}, 4^{++}$ and so on. So, the analysis in the frame of hadron spectroscopy intends to look for answers to the following questions:

- how many resonant states are there in this system;
- which masses, widths, production cross-sections and quantum number J^{PC} have the observed resonances;

[1] European Organization for Nuclear Research, France and Switzerland.
[2] Argonne National Lab, USA.

- what is the inner structure of the resonances and the mechanism of their production.

To find the answer to the first and second questions it is necessary to plot the invariant mass of the investigated system and to study the angular distributions with the help, for example, of a partial-wave analysis. The answer to the third question is a more complex problem, with no unambiguous solution. The study is performed in close collaboration with theorists. The possible decay channels of the resonances, the partial widths and the production cross-sections in miscellaneous reactions are studied, and for the analysis of the problem, the additional kinematic variables reflecting the dynamics of the particle production are used.

More than 30 years of the $\eta\pi$ system analysis by many experimental groups, in varied reactions and at different energies, do not give the final answer to even one of the questions listed above. Now we can speak with a fair degree of confidence about the existence of three resonances decaying to η and π. They are $a_0(980)$, $a_2(1320)$ and $a_4(2040)$ having quantum numbers $J^{PC} = 0^{++}, 2^{++}$ and 4^{++} respectively. The first two particles, $a_0(980)$ and $a_2(1320)$, were observed by all experimental groups studying the $\eta\pi$ system at different energies and in various reactions. Other decay channels of these particles are also thoroughly studied.

Quite a long time ago, in 1978, the third resonance was detected as having spin 4, and decaying to $K\bar{K}$ and $\pi^+\pi^-\pi^0$ ([13] and [14] respectively). However, only in 1996 did the group GAMS publish the work in which the decay $a_4(2040) \to \eta\pi^0$ [18] was studied. The almost 20-year pause in the study of this resonance was caused by the need to complete the full partial-wave analysis, in order for the $\eta\pi$ system to extract the mass dependence of the 4^{++} wave, because the particle is not visible in the mass spectrum due to a large background in the high mass region. The complex mathematical technique for a partial-wave analysis for high spin systems was only developed in the recent years.

Up until 1988, many experimental works dedicated to the analysis of $a_0(980)$ and $a_2(1320)$, in particular in the $\eta\pi$ channel, were published. Statistics were increased, the parameters of the resonances were updated, new decay channels were sought. But in the scientific world, the study of the $\eta\pi$ system did not a cause special interest except for, perhaps, some disputes about the nature of the $a_0(980)$, whose properties differ from ordinary quark-antiquark state. It was however known that the $\eta\pi$ system is a good territory for searches for exotic particles, because this system can have exotic quantum numbers $J^{PC} = 1^{-+}$. It is noted above that such particles cannot be built by quark and antiquark only. However, if a particle with such quantum numbers is observed, it is possible to explain its existence and properties in the frame of a $q\bar{q}g$-model [15]. Also 1^{-+} objects can exist in fourquark $q\bar{q}q\bar{q}$ models [16, 17]. Glueballs ($2g$,$3g$...) can also have quantum numbers $J^{PC} = 1^{-+}$, but a glueball cannot decay to $\eta\pi$ due to its isospin $I = 1$.

In 1988, the GAMS Collaboration published the work [19] which studied the charge exchange reaction $\pi^- p \to n\eta\pi^0$ at 100 GeV CERN-SPS π^- beam and observed an exotic 1^{-+} resonance in the $\eta\pi^0$ system. Active studies of meson systems which have exotic waves and, in particular, the $\eta\pi$ system have begun from this year. In the last 10 years several experimental groups have undertaken such studies. They are listed below:

- the GAMS Collaboration, already mentioned above, working on the CERN-SPS and the U-70 (IHEP,Protvino) beams and studying the reaction of π^- charge exchange on protons at energies 32, 38, 100 and 300 GeV;

- the experiment VES, working on the U-70 beam (IHEP,Protvino) and studying π^- diffraction on protons at 36 GeV;

- the experiment E179, at the Japanese science centre KEK, studied the diffraction reaction of 6.3 GeV π^- meson on protons;

- the experiment "Crystal Barrel" (CB) from CERN, studied the reaction of proton-antiproton annihilation at the antiproton ring CERN-LEAR;

- the experiment E852 at the Brookhaven National Laboratory also studied the reaction of π^- diffraction on protons at 18 GeV.

The main efforts of the experimental groups studying the $\eta\pi$ system were directed towards looking for certain exotic resonances. A history of the analysis of the observed exotic 1^{-+} state, the so-called $\hat{\rho}(1405)$, will be described more explicitly later on. Two new particles decaying to $\eta\pi$, the $a_0(1450)$ and the $a_2(1620)$, were observed recently.

The particle $a_0(1450)$ is included in the catalogue PDG[3] [20], its status in the modern hadron spectroscopy and the status of the $a_0(980)$ also deserves a detailed discussion. The $a_2(1620)$ and the probable nature of this state will be debated. The observation of the $a_4(2040)$ meson in the $\eta\pi$ decay channel is mentioned above. In this work we are limited in our study by the mass 2 GeV in the $\eta\pi$ spectrum due to kinematical factors and the small statistics of the experiment and, therefore, the states with a masses higher than this limit will not be considered.

2.1 $\hat{\rho}(1405)$

Researches of the GAMS group.

As mentioned above, the first observation of the state with the exotic quantum numbers 1^{-+} was made by the GAMS Collaboration in 1988 [19] in the charge exchange reaction

$$\pi^- p \to n\eta\pi^0 \tag{2.1}$$

at 100 GeV/c π^- beam at the CERN-SPS. A partial-wave analysis was performed and a peak with a mass 1406 ± 20 MeV and a width 180 ± 20 MeV was observed in the P_0 wave. In the D_0 wave the well-known $a_2(1320)$ meson was seen. The behaviour of the phase difference between the P_0 and D_0 waves was described by 2 resonances. So it was concluded that the observation of the exotic resonance was made in the P_0 wave. In the chapter 4 the procedure of a partial-wave analysis and accepted indications will be described in detail. Here we note only that the P and D waves in the $\eta\pi$ system have respectively the quantum numbers $J^{PC} = 1^{-+}$ and 2^{++}, which correspond to spins 1 and 2. The index "$_0$ " means a wave with zero spin projection, the indices "$_+$" and "$_-$ " concern the superpositions of waves with spin projections 1 and -1. Note that the waves with indices "$_0$ " and "$_-$" correspond to exchange with so-called unnatural spin-parity in the t-channel of the reaction 2.1 and waves with the index "$_+$ " correspond to exchange with a natural spin-parity[4].

A lot of criticism was directed at the work [19] at that time. In the study [31] it

[3] Particle Data Group

[4] A natural spin-parity $= (-1)^J$, an unnatural spin-parity $= (-1)^{J+1}$, where J is the spin of the exchanged particle.

was noted that the relative phase motion of the two resonances in the P_0 and D_0 waves should have a more complex behaviour than the one observed. Also the explanation of the a_2 meson production by a ρ exchange is absolutely incorrect because it is incompatible with the observed zero projection of the spin. Besides, the dominant production of the a_2-meson in the D_0 wave was in contradiction with the previous experimental results [32, 33] and with the Regge theory, which predicts that the ratio between intensities of unnatural and natural exchanges should decrease proportionally to $\frac{1}{p}$, where p is the beam momentum. This model works well in the case, for example, of ω meson [34]. The measurements at 4, 12 and 15 GeV/c (reaction 2.1) [32, 33] also corresponded to predictions of the theory. The dominant production of the a_2-meson at 100 GeV/c with a natural spin-parity exchange followed from these measurements, that is the a_2 must form in a D_+ wave instead of D_0. It was confirmed in later experiments, including GAMS.

In 1995 Y.D.Prokoshkin, the leader of the GAMS Collaboration, and S.A.Sadovsky published works [35] and [36], where they pointed to a discrepancy in the results [19] with regard to the Regge theory and analysed possible errors, which could have been made in the data analysis. A possible reason for such a mistake could be the use of the approximate method of minimization in the partial-wave analysis. In addition, the ambiguity of the partial-wave solutions was not resolved at that time and instead of eight solutions only two were found. Later the GAMS group performed a new analysis of the reaction 2.1 at 100 GeV/c, and has published its results together with the results of the analysis of the same reaction at 32 and 38 GeV/c [23]. The results obtained at three different energies, at different installations, in two different experiments have been very similar. The GAMS results of the partial-wave analysis of the $\eta\pi^0$ system in the reaction 2.1 at 100 GeV/c are presented in the figure 2.1. As it can be seen, the $a_2(1320)$ peak dominates in a D_+ wave. The P_0 wave is practically equal to zero, but the peak in the P_+ wave, having the exotic quantum numbers $J^{PC} = 1^{-+}$ and the resonant behaviour of the phase between P_+ and D_+ waves, is clear. The conclusion was the following: the broad peak in the P_+ wave in the mass region around 1300 MeV is a non-resonance structure, because the behaviour of the relative P_+ and D_+ phases, together with their amplitudes squared, are well enough described by the sum of the $a_2(1320)$ resonance and some non-resonance components.

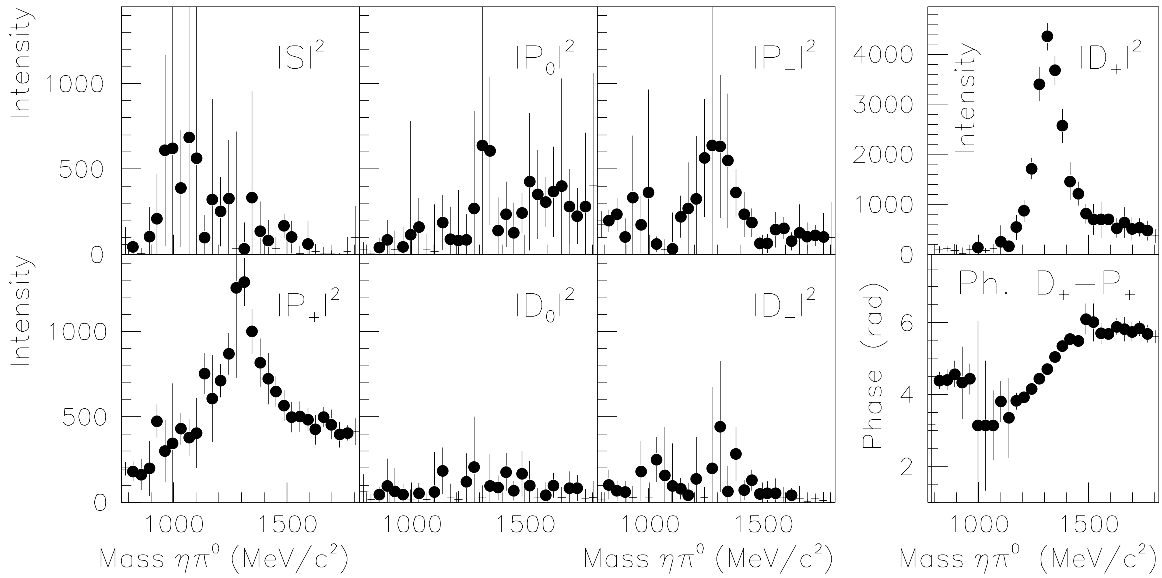

Figure 2.1: Results of the $\eta\pi^0$ partial-wave analysis obtained by the GAMS group in 1997. Figure from [23].

The work [23] did not complete the study of the $\eta\pi^0$ system. In 1998 S.A.Sadovsky made the report on the conference LEAP'98 [37], where he pointed to a number of mistakes in the study [23], in particular, in the definition of the normalization condition and in the selection of the physical solution in the partial-wave procedure that could result in new errors. The ratio of the $a_2(1320)$ production in natural and unnatural exchanges obtained in [23] was lower than the one predicted by the Regge theory and the results [32, 33] for 38 GeV. The analysis of the angular distributions, performed by S.A.Sadovsky on the basis of spherical moments measured in [18], gave a result closer to the theoretical prediction for the ratio of exchanges with natural and unnatural spin-parity. The conclusions of the study [37] concerning the 1^{-+} exotic state were the following: a resonance with a mass 1370 MeV is seen in the P_+ wave with a width 300 ± 125 MeV and in the P_0 wave with a width 225 ± 50 MeV; the cross-section of its production in the P_+ wave is approximately twice larger than in the P_0 one.

The author of this thesis, as a member of the GAMS Collaboration, would like to point out that the GAMS group now accumulates experimental data from the reaction 2.1 measured by the spectrometer GAMS-4π, which is an order of magnitude better than the one used in earlier works [18], [23] and [37]. Now, a wide experience in partial-wave analysis of two pseudoscalar particles has been gained, the problem of ambiguous solutions has been solved and the technique of background substraction in the partial-wave analysis has been developed, therefore the analysis of the GAMS-4π data should help to clear the complex situation about the 1^{-+} state.

The GAMS Collaboration also studied the $\eta\pi^0$ system in the central production reaction: $pp \to \eta\pi^0 pp$ [38]. The study was performed at 450 GeV/c incident proton beam at the CERN-SPS using the GAMS-4000 spectrometer. ~2700 $\eta\pi^0$ events have been selected, a mass spectrum has been built and the analysis of the angular momentums has been performed. No indication on the existence of an exotic 1^{-+} state has been observed. But a detailed partial-wave analysis was not performed in that study, the statistics was also small. So it was not possible to reach any reliable conclusions about the 1^{-+} state. In the study [38] an interesting phenomenon has been observed for the first time: a much more intensive $a_0^0(980)$ production compared with $a_2^0(1320)$. In the charge exchange reactions, studied earlier, the situation was exactly the opposite: the $a_2^0(1320)$ production is in order of magnitude larger then the $a_0^0(980)$ production.

In the previous paragraphs we did not follow the chronology of the performed $\eta\pi$ studies. The basic works dedicated to the search of the exotic $\hat{\rho}(1405)$ state in the $\eta\pi$ system are presented in the table 2.1 in chronological order.

Experiment	E_{beam},GeV Reaction	Wave	Mass,MeV	Width,MeV	Reference
GAMS'88	$100\pi^- p \to n\eta\pi^0$	P_0	1406 ± 20	180 ± 20	[19]
VES'93	$36\pi^- A \to A\eta\pi^-$	P_+	nonresonante structure		[21]
KEK'93	$36\pi^- p \to p\eta\pi^-$	P_+	1323.1 ± 4.6	143.2 ± 12.5	[22]
GAMS'97	$32, 38, 100\pi^- p \to n\eta\pi^-$	P_+	nonresonante structure		[23]
E852'97	$18\pi^- p \to p\eta\pi^-$	P_+	$1370 \pm 16^{+50}_{-30}$	$385 \pm 40^{+65}_{-105}$	[24]
CB'98	$\bar{p}n \to \eta\pi^0\pi^-$	$P_{\eta\pi}$	$1400 \pm 20 \pm 20$	$310 \pm 50^{+50}_{-30}$	[27]
CB'99	$\bar{p}p \to \eta\pi^0\pi^0$	$P_{\eta\pi^0}$	1360 ± 25	220 ± 90	[28]

Table 2.1: Results of the basic works dedicated to the search of the exotic $\hat{\rho}(1405)$ state in the $\eta\pi$ system.

Researches of the VES group.

After the work [19] the VES experiment performed a study of the $\eta\pi^-$ system [21]. A partial-wave analysis of the π^- diffraction on the beryllium target

$$\pi^- A \rightarrow A\eta\pi^- \tag{2.2}$$

at 32 GeV was made. The results of the analysis are shown in the figure 2.2. They were interpreted as follows: the waves with unnatural spin-parity exchange are negligible, in the P_+ wave a broad nonresonance peak is seen in the mass region ≈1400 MeV. The intensity of the P_+ wave is also small and equal ≈ 5% of the dominant D_+ wave.

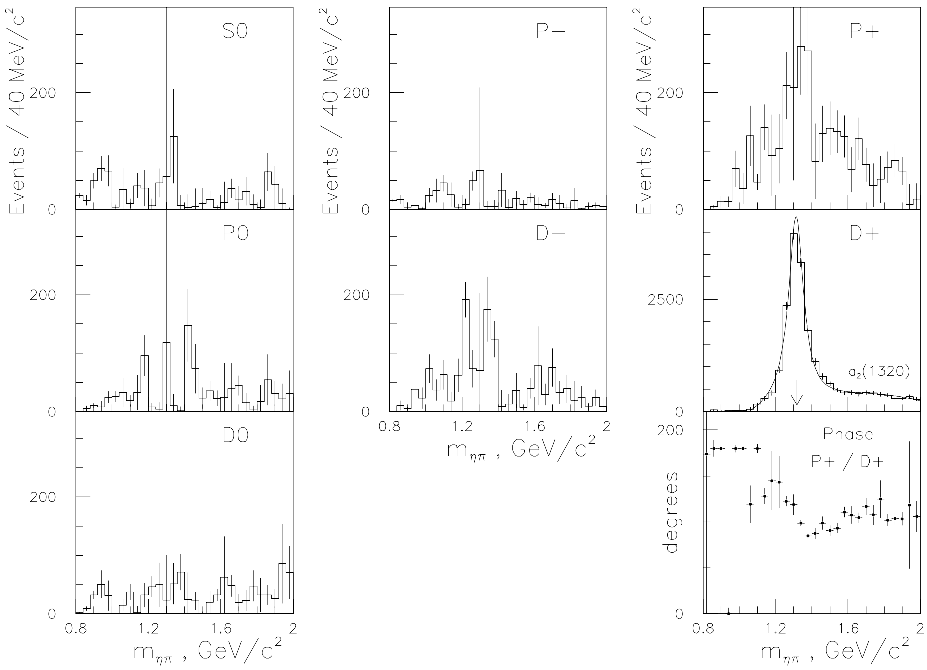

Figure 2.2: Results of the partial-wave analysis of the $\eta\pi^-$ system, obtained by the VES experiment in 1993. Figure from [21].

In parallel the VES group performed the analysis of the reaction

$$\pi^- A \rightarrow A\eta'\pi^-, \tag{2.3}$$

in which a broad peak was observed in the mass region about 1600 MeV. It has an intensity which is about half of the total cross-section in this mass region. The P_+ wave matrix element squared for $\eta'\pi^-$ in the region > 1400 MeV was several times higher than for $\eta\pi^-$. Such a behaviour of decay constants is predicted for hybrid $q\bar{q}g$ systems [17] and it does not depend on the resonant or nonresonant nature of the wave. So the authors concluded that in the mass region ~1600 MeV, in the reaction 2.3, some hybrid systems are produced intensively.

Study of the KEK group.

In the same year, 1993, a study was published by the E179 experiment [22] at the Japanese science centre KEK. They studied the reaction of π^- diffraction on protons

$$\pi^- p \longrightarrow p\eta\pi^- \tag{2.4}$$

at 6.3 GeV. The results of their angular analysis are presented in the figure 2.3.

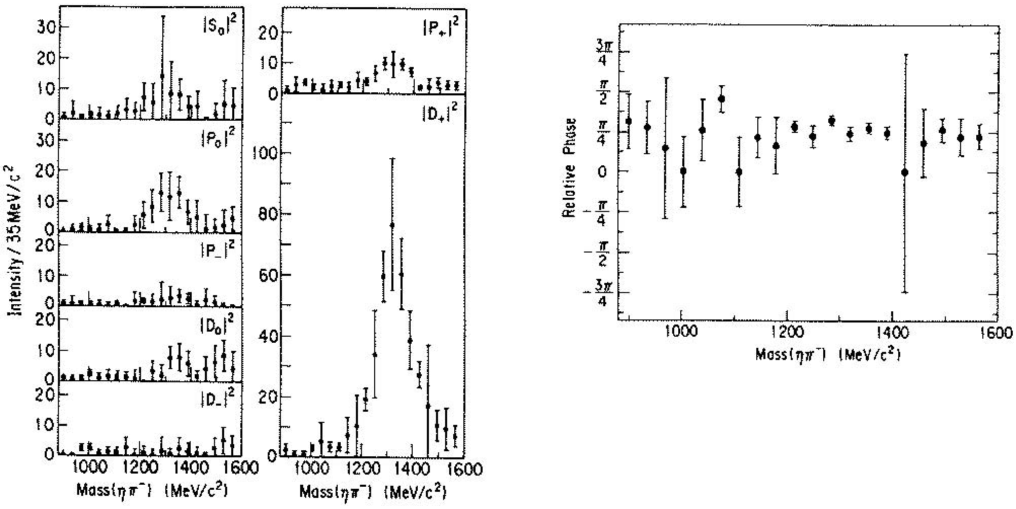

Figure 2.3: Results of the partial-wave analysis of the $\eta\pi^-$ system, obtained by the E179 experiment in 1993. Figure from [22].

A rather narrow peak with a width ~140 MeV and a mass ~1320 MeV was observed in the P_+ wave. The phase difference between the P_+ and D_+ waves was described well by a constant, that is possible to explain by the existence of two resonances in these waves with identical masses and widths. The authors concluded that one of these resonances is the $a_2(1320)$ and the second one is the exotic 1^{-+} state. However, this result causes some doubts, if we take into account the suspicious coincidence of the masses of resonances in the P_+ and D_+ waves and their approximately equal widths. Also it can be seen that in the remaining waves at a mass 1320

MeV there is some dominance of the spectrum over the background. It is easier to explain this constant by a transfer of the dominate D_+ wave into the remaining ones due to, for example, inaccuracies in the efficiency calculation. The value of the effect (intensity of P_+ wave) is less than 10% of the spectrum.

Study of the E852 experiment.

In 1997 the E852 Collaboration at BNL undertook the next attack of the $\eta\pi^-$ system looking for the exotic 1^{-+} state. They studied the reaction 2.4 at 18 GeV. The results obtained [24] were very close to the results of the VES experiment [21]. The waves with an unnatural spin-parity exchange were small. Only P_+ and D_+ waves were observed in the mass region of the $a_2(1320)$ meson. The intensities of these waves and their relative phase are shown in the figure 2.4. As well as the VES result [21], in the P_+ wave we can see a peak, interpreted by the VES group as a broad nonresonant structure. However, the group at BNL, with identical result, has concluded differently.

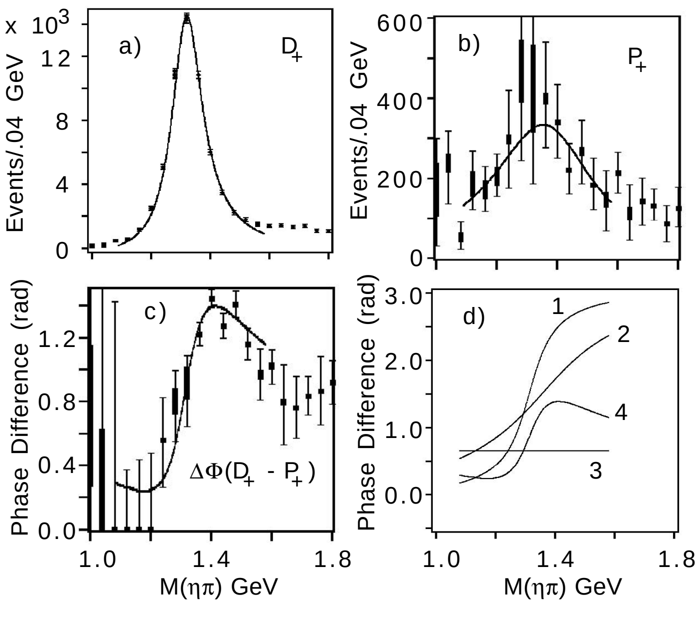

Figure 2.4: Results of the partial-wave analysis of the $\eta\pi^-$ system, obtained by the E852 experiment in 1997. Figure from [24] (see comments in the text).

The joint fit of the P_+ and D_+ amplitudes squared and their relative phase was performed with the assumption of two Breit-Wigner resonances. Also a constant phase shift was entered between the P_+ and D_+ waves. The results are shown in the figure 2.4. The figure 2.4 d) shows the phases of the resonances in the D_+ (1) and P_+ (2) waves, the phase shift (3) and the difference between the P_+ and D_+ phases (4), taking into account the constant phase shift, that is (4)=(1)-(2)+(3). The χ^2 of such a fit, divided by the number of degrees of freedom N, is equal to 1.49. For an alternative hypothesis, where the peak in the P_+ wave is described by a normal distribution, $\chi^2/N = 1.55$, that is a practically same value as for the first hypothesis. However, the phase shift between the waves, which was a constant in the first case, should enter as a linear function of mass in the second hypothesis to reach a good description of data. The constant phase shift between the waves is a consequence of the Regge theory [39] and it is difficult to explain a fast varying phase shift, as in the second hypothesis, in the frame of any model. This has allowed the authors to conclude that they observe a resonance structure. This resonance has the quantum numbers $J^{PC} = 1^{-+}$ and its parameters are presented in the table 2.1 (5-th row).

It is interesting to note that preliminary results of the $\eta'\pi^-$ analysis, obtained by the E852 experiment were reported recently [25]. They wonderfully coincide with the results of the VES experiment [21]: the P_+ wave has no structure in the mass region of the $a_2(1320)$ meson and has a broad peak in the region about 1600 MeV. This peak is interpreted as a resonant exotic state $\pi_1(1600)$, observed by the E852 experiment earlier in the $\rho(770)\pi$ decay channel in the study of the reaction $\pi^- p \to p\pi^-\pi^+\pi^0$ [26].

Researches of the Crystal Barrel experiment.

One year later the Crystal Barrel Collaboration has confirmed the observation of their colleagues of BNL, investigating the reaction of antiproton annihilation in liquid deuterium [27]:

$$\bar{p}d \to \pi^-\pi^0\eta p. \tag{2.5}$$

The Zemach method [40] was used for the analysis of the angular distributions of the reaction 2.5. In this method the production of three particles in the final state goes through the intermediate decay of isobars entered into the analysis. Testing different sets of isobars, the analysis looks for the model that best describes the data. The mass dependence of the waves can be either resonant or nonresonant.

The analysis has shown that a resonant P wave in the $\eta\pi$ system is needed for a good fit of the angular distributions in both combinations (as neutral as charged one). The figure 2.5 demonstrates that the P wave hypothesis essentially improves the $\chi^2 = \sum_{cells}(N_i^{exp} - N_i^{theor})^2/\sigma^2$. In the two upper histograms of 2.5 the χ^2 distributions for the fit including a P wave are presented on the Dalitz plot of the reaction 2.5 and in the bottom histograms of 2.5 without the P wave. It is seen that the P wave hypothesis essentially improves the fit.

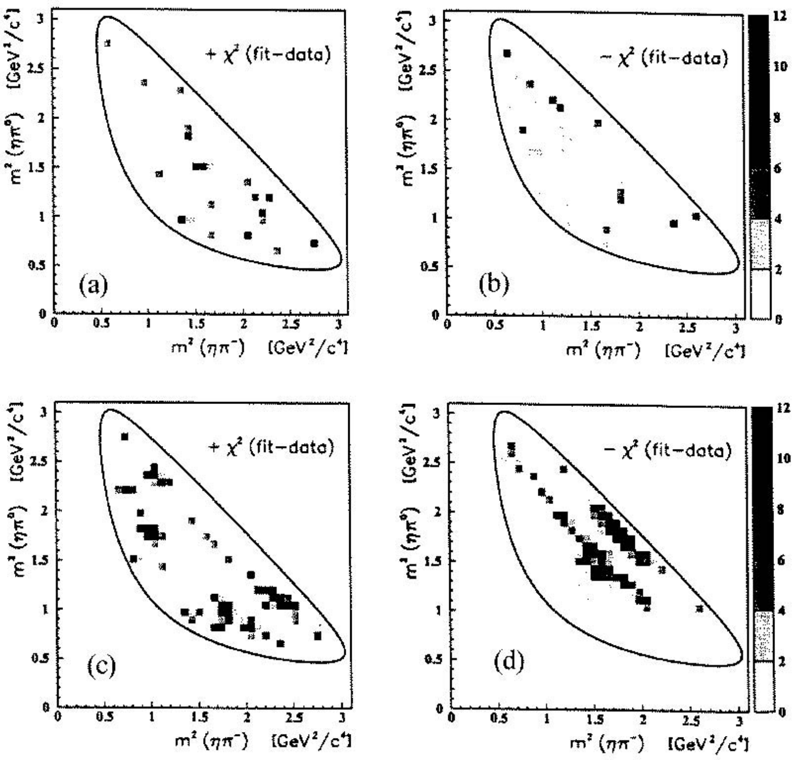

Figure 2.5: Results of the analysis of the reaction $\bar{p}d \to \pi^-\pi^0\eta p$, obtained by the Crystal Barrel experiment in 1998. Figure from [27].

The next study of the Crystal Barrel experiment was related to the partial-wave analysis of the reaction

$$\bar{p}p \to \pi^0\pi^0\eta, \tag{2.6}$$

where the observation of a 1^{-+} resonance in the $P_{\eta\pi^0}$ wave [28] was confirmed. The mass and the width of the resonance for both reactions are presented in the table 2.1 (last row). They are close to the parameters of the 1^{-+} state detected by the E852 experiment. It is important to note that in 1994 the Crystal Barrel Collaboration already published the results of a partial-wave analysis of the reaction 2.6 [29], where the exotic 1^{-+} wave was entered, but its contribution was not statistically significant. The data for this analysis was obtained in an antiproton annihilation in liquid hydrogen. The new data, in which the 1^{-+} state was observed, was obtained in gaseous hydrogen, in which the probability of annihilation from the nuclear P-state is much higher. At the same time the analysis of the $\bar{p}p \rightarrow \pi^0\eta\eta$ reaction [30], performed in 1998 by the Crystal Barrel, has not required the new exotic $P_{\eta\pi^0}$ wave. The resonance 1^{-+} was not observed in [30].

Theoretical discussion.

At the present time a particle with the quantum numbers $I^G J^{PC} = 1^- 1^{-+}$ is included in the PDG catalogue [20] and named $\hat{\rho}(1405)$. Having looked once again at the table 2.1 it is possible to come to the conclusion that the situation with this exotic state is far from a solution. All groups observe a statistically significant peak in the P wave in the mass region $1.3 \div 1.4$ GeV. Two experiments interpret it as a broad nonresonant structure, three experiments insist on the resonant nature of the peak and regard the detected phenomenon as a particle. If we look to the theory, the situation does not become more clear. As it was already mentioned above, the state with the quantum numbers $J^{PC} = 1^{-+}$ cannot consist of quark and antiquark. It can be a hybrid $q\bar{q}g$ or a fourquark state $q\bar{q}q\bar{q}$. The calculations based on the "MIT bag" model [41] demonstrate that a 1^{-+} hybrid may have a mass ~1.4 GeV. On the other hand, the "flux-tube" model [42, 43] predicts the mass of the lightest hybrid, which cannot be below 1.8 GeV. The numerical calculations on latice [44] also give an estimation for the mass of a 1^{-+} hybrid in the range from 1.7 to 2.1 GeV, which is far from the mass obtained experimentally. Meanwhile the parameters of fourquarks are predicted only for S-wave states ($J^P = 0^+, 1^+, 2^+$) [45], but there is no calculation for 1^-.

Nevertheless, the hypothesis of a fourquark state seems to be preferable than the hypothesis of a hybrid to explain the nature of the $\hat{\rho}(1405)$. Such a conclusion comes out naturally, if one takes into account that, if the hybrid decays to the $\eta\pi$ channel, it should decay to the $\eta'\pi$ channel more intensively [17]. However, neither the VES experiment[21] nor the E852 experiment [26], which studied the π^- diffraction on beryllium and hydrogen targets, have not observed any excess of the P wave production in the $\eta'\pi^-$ system compared with the $\eta\pi^-$ one. They have not found any structure at all in the P wave in the $\eta'\pi^-$ system in the mass region $\sim$1.4 GeV. The Crystal Barrel experiment, studying the annihilation $\bar{p}p \to \pi^0\pi^0\eta'$ [46], has not observed the exotic $P_{\eta'\pi^0}$ wave either.

2.2 $a_0(980)$ and $a_0(1450)$

As already mentioned, more than 30 years have passed since the $a_0(980)$ observation in the $K\bar{K}$ [12] and $\eta\pi$ [10, 11] channels, but the nature of this particle has not received unambiguous explanation until the present time. Theoretical as well as experimental works, dedicated to this subject, are published each year.

Until recently the $a_0(980)$ has been a solitary particle, having the quantum numbers $I^G J^{PC} = 1^-0^{++}$, and has been naturally considered as a lower isovector scalar state, that is as an ordinary $q\bar{q}$ meson alongside with its isoscalar partner $f_0(980)$ [47]. In this model a_0 consists of the following quark combination:

$$a_0^0 = (u\bar{u} - d\bar{d})/\sqrt{2}, \quad a_0^+ = u\bar{d}, \quad a_0^- = d\bar{u}.$$

However, many properties of the $a_0(980)$ and the $f_0(980)$ are not described in the frame of the $q\bar{q}$ model. Both particles have masses which are very close to the $K\bar{K}$ threshold, and the decay constants to $K\bar{K}$, which are higher than the estimations for $q\bar{q}$ models. The widths of these particles are anomalously small. It is possible to explain these properties using a model of $K\bar{K}$ molecules [48]. Besides, the models of fourquark $q\bar{q}q\bar{q}$ state [45] and hybrid $q\bar{q}g$ state [49] were suggested as explanation. It is possible to meet more exotic models in the literature, see, for example, [50], [51].

Many experimental facts, concerning $a_0(980)$ and $f_0(980)$, have been accumulated up to the present time. The combined consideration of them allows multiform models to be sorted, some of them to be rejected. Basically, this comparison with the models is due to rare decay measurements namely:

(1) electrical dipole decays $\phi \to \gamma f_0(980) \to \gamma\pi^0\pi^0$ and $\phi \to \gamma a_0(980) \to \gamma\pi^0\eta$ [52, 53] giving:

$$BR(\phi \to \gamma f_0(980) \to \gamma\pi^0\pi^0) = (0.5 \pm 0.06 \pm 0.06) \cdot 10^{-4},$$

$$BR(\phi \to \gamma a_0(980) \to \gamma\pi^0\eta) \simeq 0.5 \cdot 10^{-4}.$$

(2) width of $a_0(980)$ decay to $\gamma\gamma$ [54, 55] giving:

$$\Gamma(a_0 \to \gamma\gamma) = (0.19 \pm 0.07^{+0.1}_{-0.07})/BR(a_0 \to \pi\eta) \text{ keV},$$

$$\Gamma(a_0 \to \gamma\gamma) = (0.28 \pm 0.04 \pm 0.1)/BR(a_0 \to \pi\eta) \text{ keV}.$$

(3) decays of J/ψ to $a_2(1320)\rho$ and $a_0(980)\rho$ [20, 56] giving:

$$BR(J/\psi \to a_0(980)\rho)/BR(J/\psi \to a_2(1320)\rho) < 0.04 \pm 0.008.$$

Analysing these results and the experimental data of $f_0(980)$ decays, many theorists prefer the fourquark model $q\bar{q}q\bar{q}$ which better describes the experimental data than the models of $q\bar{q}$ meson and $K\bar{K}$ molecule (see, for example, [57]). The structure of a_0 in the fourquark model can be presented as

$$a_0^0 = s\bar{s}(u\bar{u} - d\bar{d})/\sqrt{2}, \quad a_0^+ = s\bar{s}u\bar{d}, \quad a_0^- = s\bar{s}d\bar{u}.$$

For such states the decay $\phi \to \gamma a_0$, mentioned in the item (1), is not prohibited, while the quark-antiquark a_0 meson is suppressed up to 10^{-6} by the OZI rules [58, 59]. The experimental values of the item (2) correspond well to the fourquark model [60]:

$$\Gamma(a_0(980) \to \gamma\gamma) \sim 0.27\,\text{keV}$$

and also contradict the predictions of the $q\bar{q}$ model [61, 62]:

$$\Gamma(a_0 \to \gamma\gamma) = (1.5 - 5.9) * \Gamma(a_2 \to \gamma\gamma) = (1.5 - 5.9) * (1.04 \pm 0.09)\,\text{keV}.$$

The item (3) does not contradict the fourquark model of a_0 and it would be difficult to explain if the a_0 were an ordinary meson. The model of $K\bar{K}$ molecules does not contradict items (2) and (3), but it does not agree with (1). For $K\bar{K}$ molecules predicts [63]:

$$BR(\phi \to \gamma f_0 \to \gamma\pi\pi) \simeq BR(\phi \to \gamma a_0 \to \gamma\pi^0\eta) \simeq 10^{-5},$$

that does not correspond to the experimental data.

For a long time physicists have been reluctant to reject the $q\bar{q}$ interpretation of the $a_0(980)$, because, if it were so, its place in the scalar multiplet whould become empty. But in 1994 the Crystal Barrel Collaboration, studying a reaction of proton-antiproton annihilation $p\bar{p} \to \pi^o\pi^o\eta$, reported the observation of a new scalar resonance in the $\eta\pi^0$ channel with a mass 1450 ± 40 and a width 270 ± 40 MeV [29]. After this discovery Crystal Barrel has performed a K-matrix analysis [64] of the three meson systems $\eta\eta\pi^0$, $\eta\pi^0\pi^0$ and $\pi^0\pi^0\pi^0$, in which the existence of the $a_0(1450)$ resonance has been confirmed [65]. It is interesting to note that in [65] the authors referred to the separate analysis of the $\eta\eta\pi^0$ system, which was not published at that time and in which the new scalar resonance $a_0(1450)$ was also seen. The study of the $\eta\eta\pi^0$ system has only appeared in 1999 [30] where the $a_0(1450)$ was not observed. The Crystal Barrel Collaboration also observed decays of $a_0(1450)$ to $K\bar{K}$ [66] and $\eta'\pi^0$ [46] channels.

It is necessary to note that before the Crystal Barrel's works in 1991 the GAMS Collaboration reported the observation of a new isovector scalar in the $\eta\pi^0$ decay channel with the a mass $\sim$1300 MeV [67]. But this study was made using the same data and the same methods of analysis as [19], where errors were later found, and thus could also contain errors. The experiment E179 from KEK in [22] also reported the observation of a 0^{++} state in the $\eta\pi^-$ system with a mass $\sim$1320 MeV. In both works [67] and [22] the new state has a small cross-section and has a mass and a width comparable to the parameters of the $a_2(1320)$ meson which dominates in the mass spectrum. So it was likely enough that the detected resonances are the result of the events flow from the dominant D wave. In proton-antiproton annihilations, the $\eta\pi^0\pi^0$ system was also studied by the experiments OBELIX [68] and ASTERIX [69]. Their analysis has not demanded the introduction of the new a_0 resonance in addition to the already known $a_0(980)$. It must be said that apart from the Crystal Barrel experiment, no other experimental group has observed the $a_0(1450)$ state until now.

Though the existence of the new isovector scalar requires serious experimental confirmations, the theorists have perceived the $a_0(1450)$ observation with pleasure, because its properties well satisfy the $q\bar{q}$ model, contrary to the properties of the $a_0(980)$. The $a_0(1450)$ pretends for the place of the $a_0(980)$ in the $^3P_0$ multiplet

[70, 71].

2.3 $a_2(1320)$ and $a_2(1650)$

The $a_2(1320)$ resonance was detected for the first time in 1964, in the π^+ diffraction on protons: $\pi^+ p \to p\pi^+\pi^+\pi^-$ [72], in the spectrum of $\rho(770)\pi$. The decays of the $a_2(1320)$ to $\eta\pi$, $\omega\pi\pi$, $K\bar{K}$, $\eta'\pi$ and $\pi^\pm\gamma$ were detected later (here these decays are arranged in decreasing order of their partial widths). The properties of the $a_2(1320)$ are well described by the $q\bar{q}$ model and it takes place in the $^3P_2$ multiplet: (a_2, f_2, K_2^*, $f_2^{,}$). It has been the sole particle with the quantum numbers $I^G J^{PC} = 1^- 2^{++}$ until recently.

In 1999, the Crystal Barrel Collaboration [30] reported the observation of a new particle decaying to $\eta\pi^0$ with the quantum numbers $J^{PC} = 2^{++}$, a mass 1660 ± 40 MeV and a width 280 ± 70 MeV. Earlier they have used the isobar with the same parameters as the analysis of the $\eta\pi^0\pi^0$ system, but they have limited data up to 1.7 GeV in the $\eta\pi^0\pi^0$ mass spectrum and reported only the preliminary observation at that time. The new resonance $a_2(1660)$ could be naturally considered as a radial excitation of the $a_2(1320)$.

There are some mentions in the literature about the observations of the isovector 2^{++} states with masses close to the mass of $a_2(1660)$. The E852 experiment (BNL) observed a particle with the quantum numbers 2^{++} decaying to $\eta'\pi^-$ [73]. This state was observed in a K-matrix analysis of $\eta'\pi^-$, $\eta\pi^-$, $b_1/f_1\pi$, $\rho^0\pi^-$ systems. The particle has a mass $\sim$1800 MeV and a width $200 \div 500$ MeV. Recently the experiment E852 finished the partial-wave analysis of the $\omega\pi^-\pi^0$ system. In this study [74] in the $\omega\rho$ channel a rather intensive peak in the 2^{++} wave is seen in the mass region about 1.6 GeV alongside the well-known $a_2(1320)$ meson, but no phase variation is observed. Such a behaviour of the wave would naturally be explained by a barrier effect, because the mass 1520 MeV is close to the threshold of the $\omega\rho$ system. A similar behaviour of amplitude and phase of the 2^{++} $\omega\rho$ wave can be observed in the study made by the VES experiment [75].

Chapter 3

The WA102 experiment

The experiment WA102, whose experimental data is the basis of this thesis, was designed for the study of the central production reactions in pp collisions. The experiment has been performed at the H1 beam of the CERN SPS at the energy 450 GeV. In the laboratory frame the beam proton is scattered forward with an energy of $\approx$400 GeV, and is called "fast". The target proton recoils at large angle with an energy of $\approx$1 GeV, and is called "slow". The decays of the central system X in charged, neutral and mixed modes are measured in the experiment. The charged particles from these decays such as $\pi^{\pm}$ and $K^{\pm}$ mesons have an energy of about 10 GeV and they are naturally called "medium" tracks. The experiment had two 100 days runs, one in 1995 and one in 1996. During these runs $5 \cdot 10^8$ events were recorded and analysed.

3.1 The WA102 setup

The experimental setup for the 1995 and 1996 runs is shown in fig.3.1 and 3.2 respectively. Its basic elements were the electromagnetic calorimeter GAMS-4000, which enables the measurement of neutral particles decaying to photons, and the spectrometer OMEGA for measuring fixed-target interactions, which produce many charged particles in the final state. OMEGA consists of a superconducting magnet, a set of proportional chambers, drift chambers, μ-strip detectors and trigger scintillation counters. The assemblage of the spectrometers GAMS and OMEGA allows the study of a broad spectrum of X decay modes with a high multiplicity of both neutral and charged products. In the region of the proportional chambers A, B and C, the magnet delivers an enough homogeneous field up to 1.8 T. At time, the field was tuned at 1.35 T to allow the measurement of tracks with a momentum of less than 1 GeV/c[1]. In a 1995 run the GAMS was placed as close to the target as possible to increase the acceptance of the registration of soft photons. In a 1996 run the Čerenkov counters were placed between the GAMS and the drift chambers to allow the decay channels of the K-mesons to be measured. More technical details of the measurement of the beam, fast and slow protons, photons and tracks will further be described. The detailed description of the setup, trigger and data acquisition may be found in [76, 77].

3.1.1 The target

A liquid hydrogen target is used in the experiment. The selection of a hydrogenous target instead of, for example, a beryllium one increases the dispersion of the vertex coordinates but eliminates nuclear effects and ensures that only *pp* interactions are measured. The point of interaction is reconstructed using the slow proton track. The target is surrounded by ten scintillation counters (TB). If the slow proton interacts in one of 2 counters located at the left and right sides from the beam[2] the event is registered, otherwise it is rejected. The distinguishing of the left-hand and right-hand slow protons is dictated by the experimental trigger and will be explained later.

[1]In figures 3.1 and 3.2 the field points opposite to the reader, i.e. positive charged particles are deflected to the left side.

[2]In fig.3.1 and 3.2 "at the left" is above than the beam axis, "on the right", accordingly, is below.

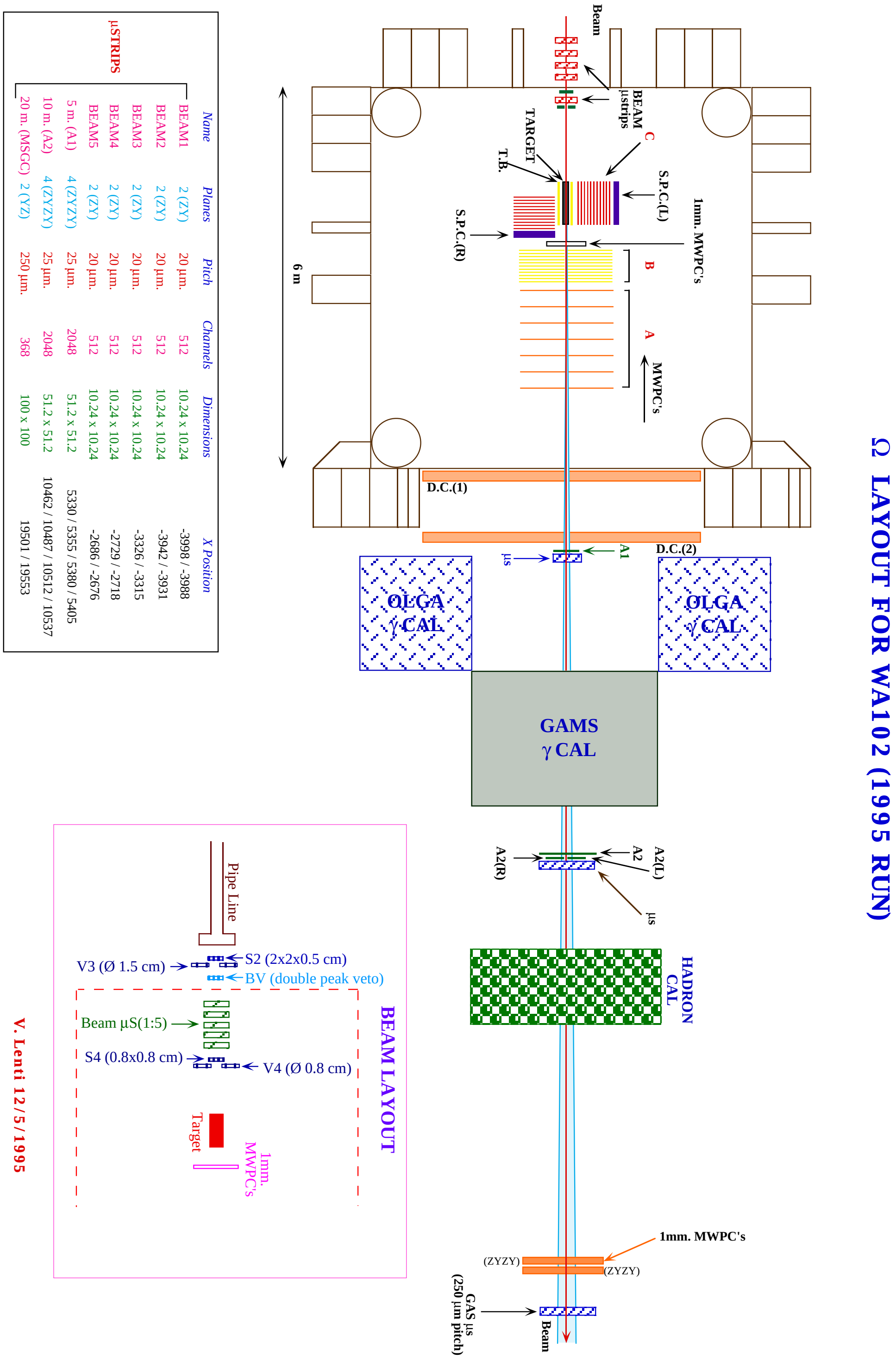

Figure 3.1: Layout of the WA102 experimental setup for the 1995 run (see comments in the text).

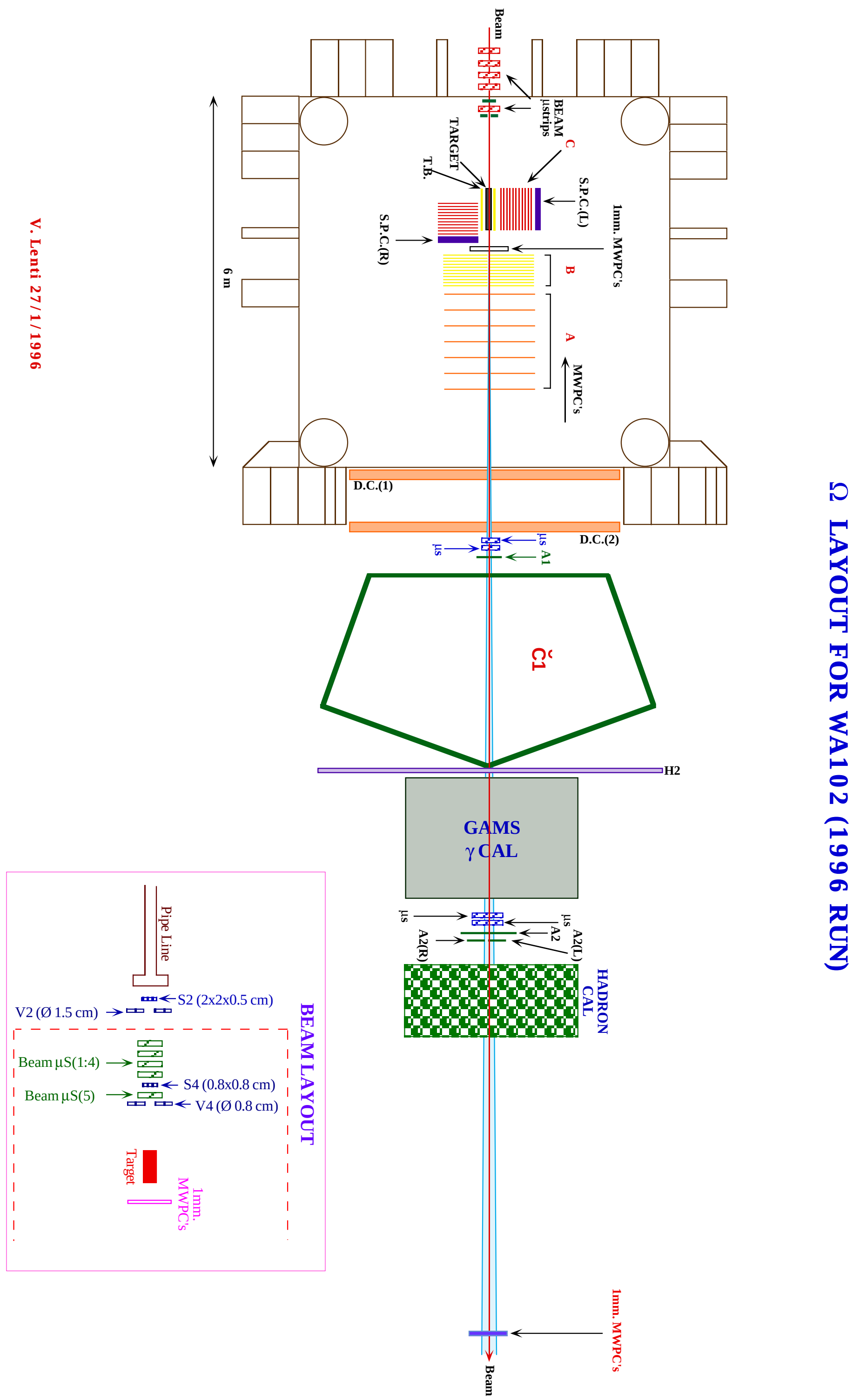

Figure 3.2: Layout of the WA102 experimental setup for the 1996 run (see comments in the text).

3.1.2 The beam trigger

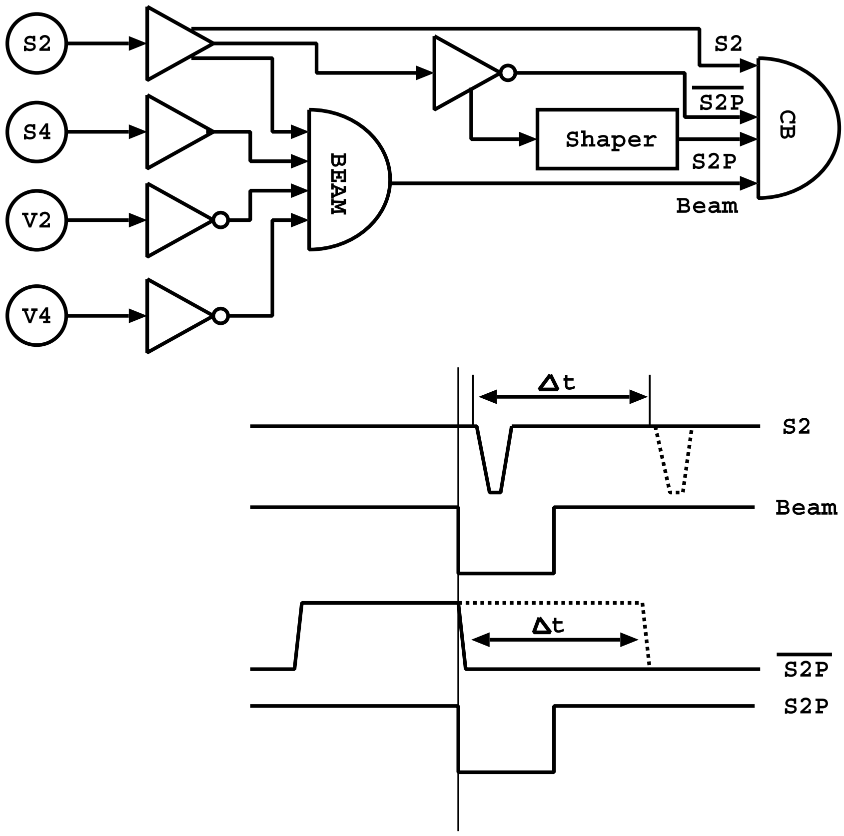

Figure 3.3: The scheme of the beam trigger.

To measure the momentum of the beam proton and to build up the beam trigger, a set of scintillation counters S2, S4, V2, V4 and μ-strip detectors, see fig.3.1, 3.2 is used. The logic of the beam trigger is reflected in the fig. 3.3. The trigger requires the coincidence of the signals S2, S2P, $\overline{\text{S2P}}$ and BEAM, where BEAM is formed by the coincidence of S2, S4 and $\overline{\text{V2}}$, $\overline{\text{V4}}$. In the absence of a proton beam, the signals S2, S2P and BEAM are equal to 0, and the signal $\overline{\text{S2P}}$ is equal to 1. At registration of the proton the signals S2, S2P and BEAM appear; $\overline{\text{S2P}}$ disappears. After about 50 ns it returns to 1 and the signal of the trigger is formed. If during this time an additional proton is registered by a scintillator S2 the signal $\overline{\text{S2P}}$ remains at zero during the following 50 ns and the first proton is not registered. Thus, the trigger allows the single interactions of protons to be only detected and avoids the "superposition" of two or more interactions in the event.

3.1.3 Measurement of the slow proton

Multiwire proportional chambers, indicated in the fig.3.1 and 3.2 by the letter C, the target box scintillation counters (TB) and the scintillation counters, arranged directly behind the chambers (SPC), are used for the registration of the slow proton. The proportional chambers, as shown in the fig.3.4, located above (”left”) the beam, are parallel to its direction. The planes of chambers, located below (”right”) the beam, are oriented perpendicularly to the beam. This arrangement of chambers is caused by the bending of the slow proton tracks in the magnetic field and corresponds to the optimal acceptance. Because of the tracks bending the efficiency of the registration of the ”left” slow protons is several times higher than the efficiency of registration of the ”right” slow protons.

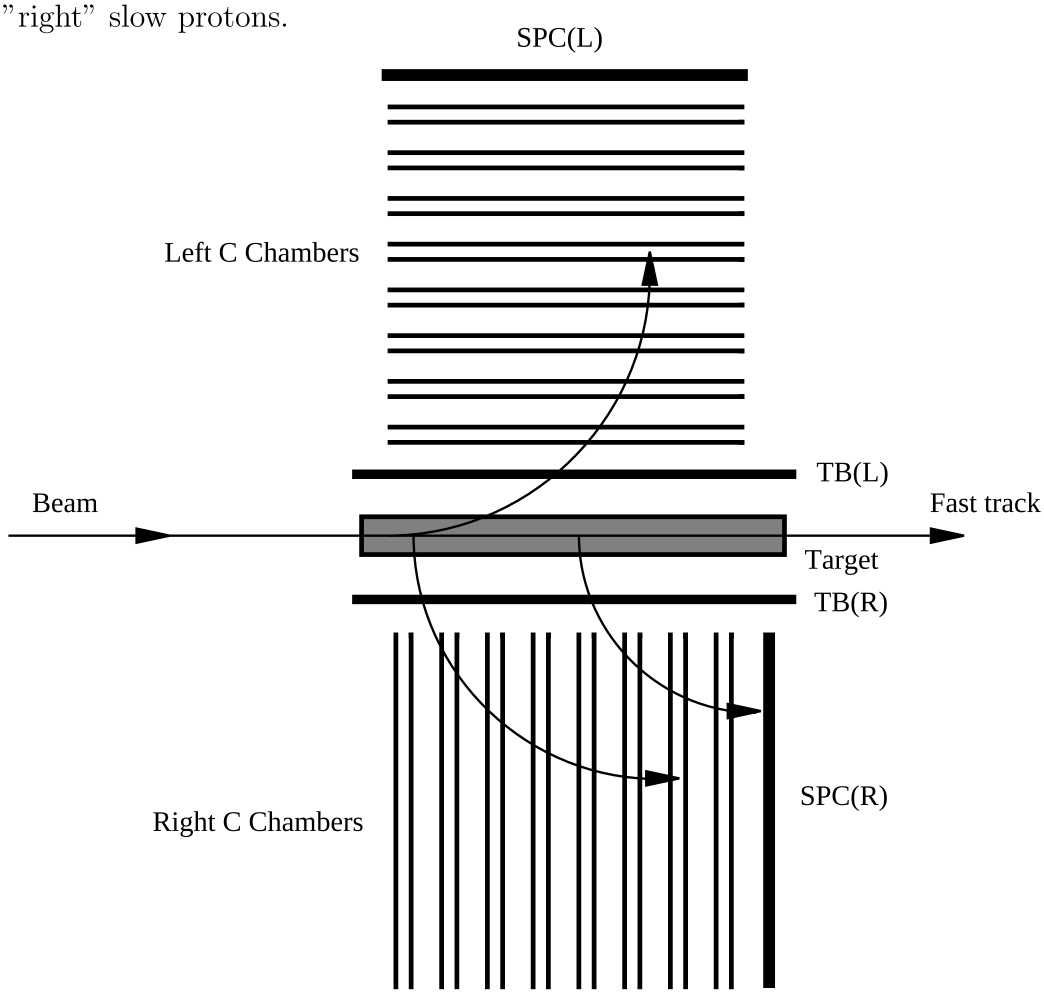

Figure 3.4: The detectors alignment for the slow proton measurement.

An intensive background process, which hinders the detection of central collisions is the process of the diffraction of the beam proton on the target proton. The diagram of this process is shown in the fig.3.5. To suppress such reactions the scintillation counters TB and SPC are used. The organization of the trigger is shown in the fig.3.6.

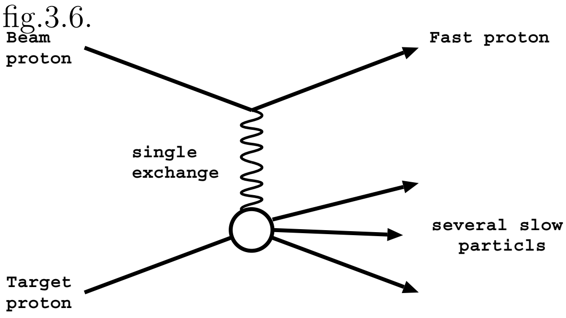

Figure 3.5: Diagram of the diffraction process.

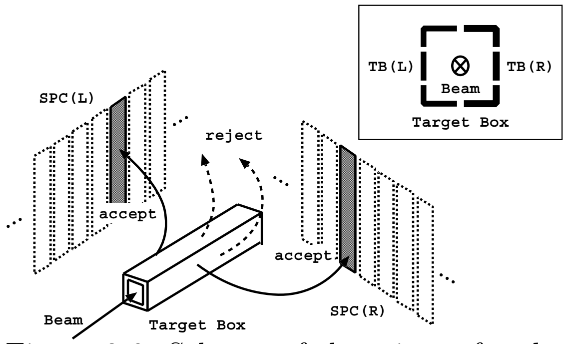

Figure 3.6: Scheme of the trigger for the slow proton.

The trigger requires

- the presence of a signal in only one of the 10 target scintillation counters: TB(L) or TB(R), other counters are used as "veto";
- the coincidence of signals in TB(L) and SPC(L) or in TB(R) and SPC(R); events of type TB(R) and SPC(L) or TB(L) and SPC(R) are rejected[3];
- the presence of one track in the chambers.

The scintillation counters SPC are also used for the identification of the particles. Fig.3.7 shows the distribution of the signal in SPC depending on the momentum of the registered particles. This figure shows that these distributions differ between protons and π-mesons. This information is used after the tracks reconstraction for the separation of events with slow protons.

3.1.4 Measurement of the fast proton

The momentum of the fast proton is measured with the 25 μm pitch μ-strip detectors, situated at 5 and 10 m from the target (in the fig.3.1 and 3.2 they are indicated by "μs"), and 1 mm pitch proportional chambers (1mm MWPC's).

[3]This requirement suppresses a *pp* elastic scattering.

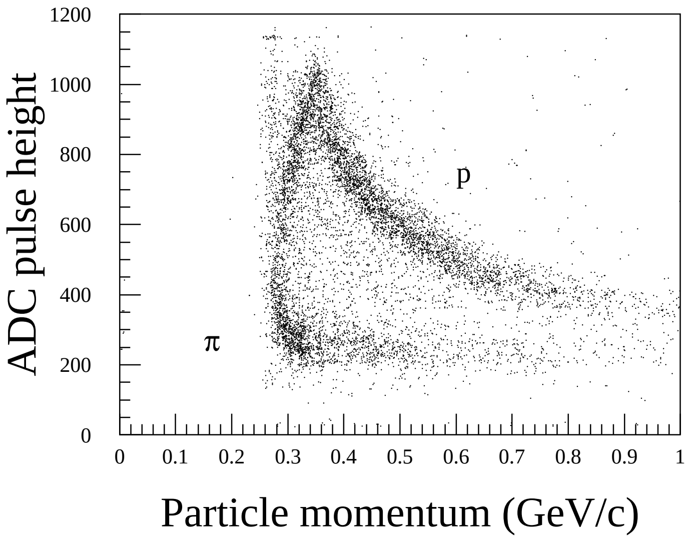

Figure 3.7: ADC pulse height in the scintillation counters SPC versus particle momentum.

The trigger for the fast proton is built up using the scintillation counters A1, A2, A2(L) and A2(R), see fig. 3.1 and 3.2. It requires:

- the coincidence of the signals in A1 and A2;
- the presence of the signal in A2(L) or in A2(R)[4].

3.1.5 Measurement of the medium tracks

The momentums of the charged particles from the decays of the central system X are measured with the 2 mm pitch multiwire proportional chambers indicated in the fig.3.1 and 3.2 with the letters A and B and the drift chambers D.C.(1) and D.C.(2). The 1 mm pitch multiwire proportional chambers (1mm MWPC's) situated directly behind the target are used for the extrapolation of the tracks in the chambers to the vertex of the interaction. The same chambers are also used for the fast proton reconstruction. In the 1996 run the Čerenkov counters Č1 were also used for the identification of the charged particles.

[4]The separation of protons on "left-hand" and "right-hand" is used in the further data analysis.

3.1.6 Measurement of γs

The electromagnetic calorimeter GAMS-4000 is used for the registration of γs coming from decays of the central system. It consists of 4092 čerenkov counters assembled as a matrix 64×64[5]. Counters are made of $38 \times 38 \times 450$ mm lead glass cells having a radiation length 2.9 cm. γ falling in the counter causes an electromagnetic shower in the lead glass. The Čerenkov's light from electrons and positrons of the shower, being mirrored from the walls of the counter, is collected by the photomultiplier fixed at the end. The value of the signal in the photomultiplier is proportional to the energy of the γ. The calorimeter is calibrated, for example, with an electron beam of known energy. Thus it can be used to measure the energy of the γs.

The parameters of the calorimeter cells were selected to get the best performances with a measurement of the electron beam using prototypes [78]. The transverse size of the cells provides the coordinate resolution ≈ 2 mm at an energy of the γs equal to 25 GeV and ≈ 1 mm at an energy of 200 GeV. It allows two γs separated by ≥ 3 cm to be distinguished. The energy resolution of the calorimeter is $\sigma_E / = 1.5\% + 0.045\%/\sqrt{E(GeV)}$ The length of the counter allows the measurement of γs having an energy of up to several hundreds GeV, which covers practically all possible energies of γs. In the center of the detector there is a hole of 4 cells to let pass through the fast proton and beam particles which do not interact in the target. It considerably reduces the background from the direct interactions of the beam with the lead glass.

In the 1995 run the additional electromagnetic calorimeter OLGA (fig.3.1), located at both sides of the GAMS, was used. Each part of OLGA consists of 6×19 cells of $14 \times 14 \times 47$ cm lead glass. The calorimeter was installed to increase the acceptance of the γs registration, but in practice it appeared that GAMS, having essentially the best coordinate and energy resolutions, alone provided sufficient acceptance. Therefore in the 1996 run the calorimeter OLGA was not used. In this work the data from the OLGA will also not be used.

In the 1995 and 1996 runs a hadron calorimeter HC240 [79] consisting of 240 counters was used. It was located behind GAMS. Each counter is made of 35 25 mm thick steel plates separated by 5 mm thick scintillator plates. The calorimeter is useful

[5] 4 cells in the centre of GAMS are removed for the letting the beam pass through.

to exclude the hadron showers, which are the result of the hits in GAMS of charged particles and can be misinterpreted in the reconstruction as extra γs. By including the hadron calorimeter in the anticoincidence with the electromagnetic calorimeter, one can reject events with charged tracks passing through GAMS. It essentially decreases the efficiency of the registration of mixed decay modes. However, "false" γs are extracted by the extrapolation of the tracks, registered by the chambers A, B and D.C., to the plane of the calorimeter, and then by comparing the coordinates of the obtained point with the coordinates of the shower in GAMS.

3.2 The trigger and the classification of events

The trigger has to suppress the background processes which have cross-sections in pp interactions comparable to or bigger than the cross-section of the double exchange process. Such background processes are:

(1) the elastic scattering $pp \to pp$, where the kinematic of protons is very similar to the one in the double exchange reaction;

(2) the "forward" diffraction (see fig.3.5), for example, of the type:

$$pp \to p_s \Delta^{++}(1232)\pi^-, \Delta^{++}(1232) \to p_f \pi^+; \tag{3.1}$$

(3) the "back" diffraction, which differs from the "forward" diffraction only in that the target proton fragments into low momentum particles instead of the beam proton.

The general trigger of the experiment is formed from the beam trigger, described in the section 3.1.2, the triggers on slow and fast protons (sections 3.1.3 and 3.1.4, respectively) the signal from the chamber A, the detected charged tracks from the decays of the central particle, and the signal from the calorimeter GAMS. The registered events are divided into 4 types:

LL

RR

LR and (GAMS or FASTRO)

RL and (GAMS or FASTRO)

The first character in LL, RR, LR and RL shows which counters, SPC(L) or SPC(R), has contributed to the trigger of the slow proton. The second character concerns the fast proton and indicates the presence of a signal in the counter A2(L) or A2(R). GAMS means that a signal from the calorimeter GAMS was required at the registration of the event. This signal is formed if the total energy in all cells of the calorimeter is more than 8 GeV. The word FASTRO ("FAST ReadOut") means that a signal from the fast information reading device in the proportional chambers has arrived. This device is connected to the third plane of the chamber A and it forms the trigger signal when two or more tracks pass through the chamber.

Registering only these types of events, we effectively suppress the background process of the elastic pp scattering because this does not fall into one of the 4 above-stated groups. Practically, the protons in this process should scatter on different sides from the beam, so they fall to the type LR or RL. In the elastic pp scattering there are no signals either in the chambers or in the calorimeters and it contradicts the condition "and (GAMS or FASTRO)".

The background process of the "forward" diffraction is not suppressed at the trigger level. The events, for example, of the reaction 3.1 were rejected by the cut $M_{p_f\pi^+} > 1.3$ GeV in the data analysis. Such a trigger allows the study of the process

$$pp \to p_s\Delta^{++}(1232)X^-, \Delta^{++}(1232) \to p_f\pi^+,$$

using the selection $M_{p_f\pi^+} < 1.3$ GeV. It also allows the analysis of the $\eta\pi^-$ system formed in the decay $X^- \to \eta\pi^-$. The trigger suppression of the "back" diffraction naturally comes out of the description given in the section 3.1.3.

3.3 The reconstruction of the events

The intensity of the proton beam of the CERN SPS H1 was 1.7×10^{11} protons per 2.6 sec spill. The cycle time was 14.4 sec. The beam intensity was reduced down to $5 \sim 6 \times 10^6$ of protons per spill by absorbers and collimators. About 900 events which passed through the trigger conditions were recorded each cycle. During the 1995 and 1996 runs (90 and 95 days accordingly) 500×10^6 events were registered, reconstructed, sorted according to the multiplicity of charged tracks and γs and used in the analysis.

3.3.1 The reconstruction of the charged tracks

For the reconstruction of the tracks of the proton beam, of the fast and slow protons and of the charged particles from decays of the central system, and for finding the vertex coordinates, the program TRIDENT is used. This program was applied in all previous experiments working with the spectrometer OMEGA and updated for the WA102 experiment. It is possible to find the detailed description of the program, the procedure of the reconstruction and algorithms for the searches for the tracks in the work [80]. Here, only the main phases of the reconstruction procedure are mentioned.

First, the reconstruction of the slow proton track is made using the information from the C chambers and the center of the target as the first approximation of the vertex. Then the x coordinate of the vertex is found as the point of intersection of the track with the beam direction. The correction of the energy loss in the scintillation counters TB surrounding the target is made by reconstructing the slow proton track. Then the track of the proton beam is also reconstructed. Using the deviation of its momentum from the X axis and the x coordinate of the vertex, two remaining coordinates are determined. The tracks from the proportional (A, B) and drift chambers (D.C) and the slow proton track are extrapolated to the point of interaction. Thus the momentums of the charged decay products and the slow proton are calculated. The correction to the energy loss by the slow proton in the target is made. The final stage of the reconstruction is the definition of the fast proton momentum using the information from the μ-strip detectors. A search for secondary vertices is also made. In this work events, which have secondary vertices, are rejected from the analysis. They were used in the analysis of K-meson decays.

3.3.2 The reconstruction of γs

In this section, the procedure for the reconstruction of the coordinates and the energy of γs detected by the calorimeter GAMS is described briefly. Detailed descriptions can be found in [81] and [82]. The initial design of the calorimeter GAMS allows the presence of a special optic grease between the lead glass and the photomultiplier to create a good optical contact and a maximum absorption of light. However, as the experience has shown it, the layer of the optic grease creates a background noise and its removal has enabled an essential suppression of the registration of the background light from muons and hadrons. The absence of the absolute optical contact has resulted in distortions in the measured electromagnetic shower shapes. So the formulas for the calculation of the shower center and the energy distribution have been corrected. This problem was solved in [81].

The calculation of the γs coordinates

The simplest estimation of the x-coordinate of a γ falling in the GAMS calorimeter can be made by the calculation of the center of gravity of the electromagnetic shower:

$$X_c = \frac{\sum_{i=1}^{n} E_i X_i}{\sum_{i=1}^{n} E_i}, \tag{3.2}$$

where E_i is the energy deposit in the cell i, and X_i is the x-coordinate of the cell center. In the figure 3.8 the solid curve shows the distribution of X_c. It has a periodic structure, though it should be isotropic, because the calorimeter's plane was uniformly irradiated by the wide electron beam. Using an additional correction to the formula 3.2 allows the situation to be vitally improved. In the figure 3.8 the dashed line shows the distribution of the variable X computed according the formula

$$X = X_c + \Delta(X_c), \tag{3.3}$$

with $\Delta(X_c) = a * t * (t^4 + b * t^2 + c) * (t^2 - \frac{1}{4}) * (t^2 - q)$, where $t = (X_c - X_0)/d$, X_0 is the x-coordinate of the cell edge nearest to X_c, d is the cell size, $-0.5 < t < 0.5$. a, b and c are free parameters, q can be obtained by setting the second derivative of the function to zero at the cell center.

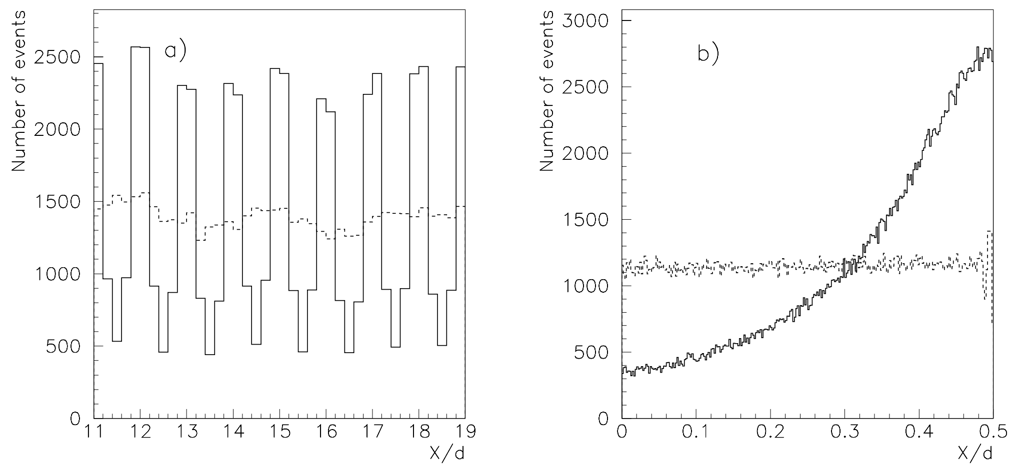

Figure 3.8: (a) the solid curve represents the distribution of the center of the shower computed according to the formula 3.2, the dashed line is the corrected distribution according to the formula 3.3. The horizontal axis is the x coordinate divided by the cell size. Figure (b) represents the same distribution as (a) added over all cells but for the half of the cell. Figure from [81].

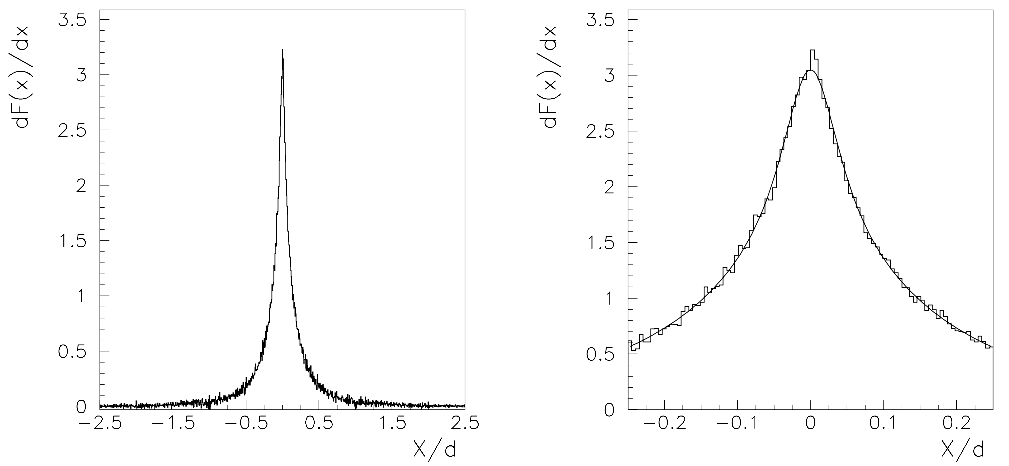

Figure 3.9: x-projection of the transverse energy density in the electron shower. The solid line shows the approximation of the distribution to the formula 3.5. The horizontal axis is the x-coordinate divided by the cell size. Figure from [81].

The parametrization of the shower profile

The energy distribution of the electromagnetic shower in GAMS can be represented by the two-dimensional cumulative function

$$F(x, y) = \int_{-\infty}^{x} \int_{-\infty}^{y} \Phi(x, y) dy dx, \tag{3.4}$$

where $\Phi(x, y)$ is the normalized (the integral over the total shower is equal to 1) energy density. The derivative $\frac{dF(x)}{dx}$ is the x projection of the transverse energy distribution in the electromagnetic shower:

$$f(x) = \frac{dF(x)}{dx} = \frac{1}{\pi} \sum_{i=1}^{3} \frac{a_i}{\frac{x^2}{b_i} + b_i}. \tag{3.5}$$

Shown in the figure 3.9 one can see that the formula 3.5 describes well the energy distribution of the x-coordinate in the electromagnetic shower.

The separation of the showers

The reconstruction program follows three stages.

1. Searches for clusters. A cluster is one or several neighbouring cells of the calorimeter with a non-zero energy deposit surrounded by cells with zero energy deposit. Each cluster is analysed independently.

2. Searches for peaks in the cluster. A peak is the cell of the cluster where the signal is higher than in all neighbouring cells. The cluster can contain more than one peak. In this case the re-computation of the energy deposit is made in the neighbouring cells according to formulas 3.5 and 3.3.

3. γ's reconstruction within the peak regions. Two nearby showers can create one peak in the calorimeter. A goal of the program is to separate them, that is, to determine the coordinates and the energies of the γs generating these showers.

   Stages 2 and 3 are realized in an iterated procedure.

In [82] the procedure for separating two nearby showers is described in detail. At first, it is supposed that the peak is formed by one γ. In a two dimensional space (X,Y) the functional

$$\chi^2 = \sum_{i=1}^{n} \frac{(A_i - E_i)^2}{c^2 A_i (1 - \frac{A_i}{E_0}) + q} \tag{3.6}$$

is minimized, where A_i is the measured energy in the cell i, E_i is the energy computed with the formulas 3.5 and 3.3, E_0 is the total energy in the peak ($\sum_{i=1}^{n} A_i$), c is the constant which represents the fluctuations of energy in the shower (in the present experiment c^2 is set to 15 MeV), and q describes the electronic noise. If $\chi^2/ND < 3$ ($ND = N_{cell} - 2$ is the number of degree of freedoms), the hypothesis of one γ in the shower is accepted; otherwise the hypothesis of two γs is investigated. To check this hypothesis the functional 3.6 is minimized in a three-dimensional space: $\alpha = (E_1 - E_2)/E_0$, $\Delta X = X_1 - X_2$ and $\Delta Y = Y_1 - Y_2$. The energy and the coordinates of each γ are computed from these variables as follows:

$$\begin{aligned} E_1 &= E_0(1+\alpha)/2, \quad X_1 = X_0 + \Delta X(1-\alpha)/2, \quad Y_1 = Y_0 + \Delta Y(1-\alpha)/2, \\ E_2 &= E_0(1-\alpha)/2, \quad X_2 = X_0 - \Delta X(1+\alpha)/2, \quad Y_2 = Y_0 - \Delta Y(1+\alpha)/2, \end{aligned}$$

where X_0, Y_0 are the coordinates of the peak center. The hypothesis of two γs is accepted if $\chi^2(2\gamma)$ is much less than $\chi^2(1\gamma)$ (in this work the condition $\chi^2(2\gamma) < \chi^2(1\gamma) - 6$ was used).

The efficiency of two nearby γs separation depends on the distance between them and their energies. For convenience it is possible to use one variable only for the data representations

$$D = \frac{2MZ}{E_0}, \tag{3.7}$$

where Z is the distance from the decay point to the calorimeter, M is the two γ's invariant mass, $E_0 = E_1 + E_2$ – their total energy. In the case $E_1 = E_2$ D represents the distance between the 2γ's. Figure 3.10 shows the efficiency of the two γ's separation, having $E_0 = 10$ GeV, as the function of D. It can be seen that an efficiency $> 90\%$ is reached on distances larger than 3.5 cm [6]. For $Z \sim 10$ m it corresponds to 148 GeV π^o's and 344 GeV η's. that greatly exceeds the energy of typical γs (< 60 GeV) as observed in the experiment. Due to the energy fluctuations in the shower

[6] In [82] it is found that the value D, at which maximum efficiency is reached, does not depend strongly on E_0.

and the noise of electronics, the profile of the shower can differ from the theoretical one. It results in errors of the reconstruction program and the program can find false γs. Figure 3.11 shows the probability of finding a third false γ in the peak actually formed by two γs. The errors of the reconstruction program are corrected at the stage of the events selection by merging the very close γs which also have small invariant mass.

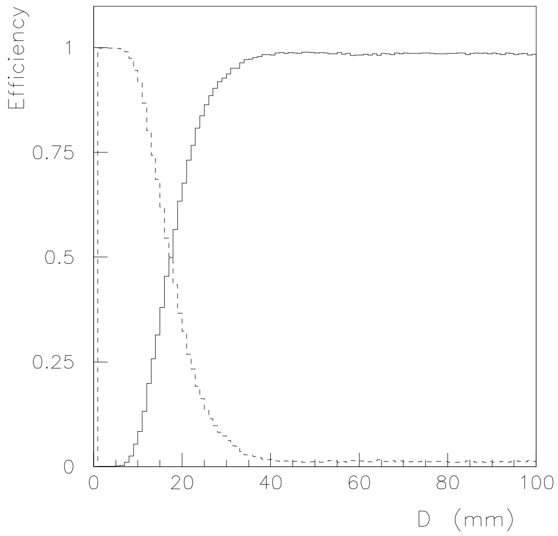

Figure 3.10: Efficiency of two nearby γ's separation. The dashed line is the probability of finding only one γ in the peak formed actually by two γs. Figure from [82].

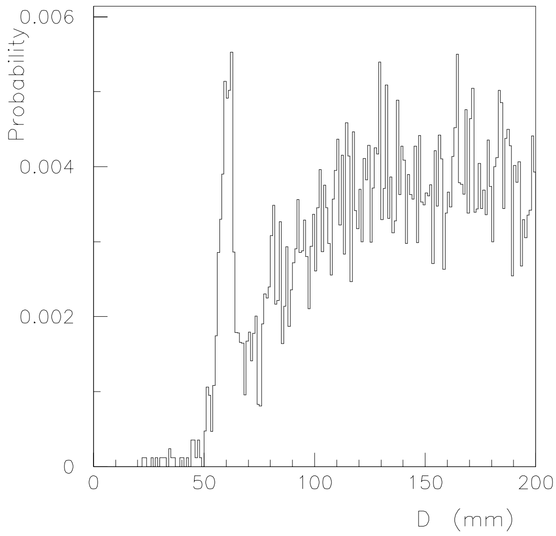

Figure 3.11: Probability of finding third false γ in the peak actually formed by two γ's. Figure from [82].

In conclusion GAMS allows the measurement of up to 10 simultaneous γs with a good confidence level.

Chapter 4

The theoretical basis of the analysis

4.1 The kinematical fit

The kinematical fit is the basic part of the data analysis procedure. It plays an important role in the selection of the events of the reactions 1.3 and 1.4. The following and essential 3 aims are reached by the kinematical fit:

- identification of the reaction;
- suppression of background processes;
- corrections of the kinematical parameters of the event.

As an example let's consider the variant of the kinematical fit for the reaction

$$\begin{aligned} &p_{beam}\ p_{target} \to p_{fast}(X)p_{slow} \\ &\qquad\qquad\qquad\quad \hookrightarrow m_1 m_2 \to 4\gamma, \end{aligned} \tag{4.1}$$

where we have 2 protons and 4 γs in the final state. If instead of m_1 and m_2 one takes, for example, η and π^0, then one gets the reaction 1.3. The input data for the kinematical fit are the parameters of the events obtained by the reconstruction procedure. Before the kinematical fit the events were selected by the first kinematical analysis (cuts on the missing momentum, γs energy and other selections which will be discussed in chapters 5.1 and 6.1).

The next terms are used below: hypotheses, constraints, combinations. For a selection of the events from the reaction 4.1 it is necessary to define 2 constraints:

$$\begin{aligned} f_1(\vec{x}) &= M^2_{\gamma\gamma}(\vec{x}) - M^2_{m_1} = 0, \\ f_2(\vec{x}) &= M^2_{\gamma\gamma}(\vec{x}) - M^2_{m_2} = 0, \end{aligned} \tag{4.2}$$

where $\vec{x}$ is the vector of the kinematical parameters of the event.

The set of several constraints presents a hypothesis. The couple of γ's can be selected from four in 6 ways, that is 6 combinations exist for the constraints 4.2. Also, one can add the following constraints to the analysis:

$$\begin{aligned} f_3(\vec{x}) &= p^x_{beam} - p^x_{fast} - p^x_{slow} - p^x_X = 0, \\ f_4(\vec{x}) &= p^y_{beam} - p^y_{fast} - p^y_{slow} - p^y_X = 0, \\ f_5(\vec{x}) &= p^z_{beam} - p^z_{fast} - p^z_{slow} - p^z_X = 0, \\ f_6(\vec{x}) &= m^2_{p_{beam}+p_{target}-p_{fast}-p_{slow}}(\vec{x}) - M^2_X = 0, \end{aligned} \tag{4.3}$$

which are the equations of momentum and mass balance. Combining different constraints from 4.2 and 4.3 it is possible to define different hypotheses. Substituting instead of M_{m_1} and M_{m_2} in 4.2 the masses of the π^0, the η or of another particles decaying to 2γ one can study different decay channels of the central particle X: $\pi^0\pi^0$, $\eta\pi^0$ and others.

The procedure of the kinematical fit is realized by the following method. Some hypothesis and one combination are fixed. The following function is constructed as presented below:

$$\chi^2 = \sum_{i=1}^{N_{par}} \frac{(x_i - x_i^*)^2}{\sigma_i^2} \tag{4.4}$$

where

x_i are the kinematical parameters of event,

x_i^* are the input kinematical parameters (from reconstructed procedure);

σ_i are the parameters errors;

N_{par} - number of parameters.

Further the minimization of 4.4 is performed under the conditions 4.2 and 4.3. The method of the undefined Lagrange coefficients is used. It reduces the problem of searching a minimum of the functional:

$$\Phi = \chi^2 - \sum_{k=1}^{N_{con}} \lambda_k f_k(\vec{x}), \tag{4.5}$$

where N_{con} is the number of constraints.

The functions $f_k(\vec{x})$ are represented by Taylor series limited only by the first derivatives:

$$f_k(\vec{x}) = f_k(\vec{x}^*) + \sum_{i=1}^{Npar} \frac{\partial f_k(\vec{x}^*)}{\partial x_i}(x_i - x_i^*). \tag{4.6}$$

In this case, the first derivatives of Φ are linear functions of the parameters. Using 4.6 and 4.5 Φ can be written in the following matrix form:

$$\Phi = \triangle X^T W \triangle X - \Lambda^T(D \triangle X + F), \tag{4.7}$$

where:

$\triangle X$ is the difference between the vectors of initial and quest parameters (dimension $N_{par} \times 1$);

W is the diagonal matrix of the parameter's weights ($W_{ii} = 1/\sigma_i^2$, dimension $N_{par} \times N_{par}$);

Λ is the vector of the Lagrange coefficients (dimension $N_{con} \times 1$);

D is the matrix of the first derivatives $f_k(\vec{x})$ in the point $\vec{x}^*$ (dimension $N_{con} \times N_{par}$);

F is the vector of the values $f_k(\vec{x})$ in the point $\vec{x}^*$ (dimension $N_{con} \times 1$).

It is necessary to solve the following system to find the minimum:

$$\begin{aligned} \tfrac{\partial \Phi}{\partial \Lambda} &= D \triangle X + F = 0 \\ \tfrac{\partial \Phi}{\partial \triangle X} &= 2 \triangle X^T W - \Lambda^T D = 0 \end{aligned} \tag{4.8}$$

Its solution

$$\triangle X = -W^{-1} D^T (D W^{-1} D^T)^{-1} F \tag{4.9}$$

allows the vector of parameters to be found:

$$\vec{x} = \vec{x}^* + \vec{\triangle x}\ . \tag{4.10}$$

The obtained parameters are equated to x_i^* and the search for the minimum is repeated. The iterations can be repeated as long as

$$|f_k| < \varepsilon_k \ , \qquad k = 1, 2, ..., N_{con} \tag{4.11}$$

The elements of the vector $\vec{x}$ calculated in the last iteration are considered as the corrected kinematical parameters of the event and the $\chi^2(\vec{x})$ are calculated. This way the χ^2 are calculated for each of the 6 combinations of γs and the combination with the minimal χ^2 is selected. Changing a hypothesis (i.e. a combination of constraints) one can repeat the fitting procedure.

Finally, after the kinematical fit, we have several vectors of corrected kinematical parameters for each event respective to each hypothesis and its χ^2. To control the quality of the kinematical fit the distribution of probability $P(\chi^2)$ is plotted. It should be flat if we used the correct errors of the parameters σ_i. Then one can select the events related to the different hypotheses and suppress the background processes by a χ^2 cut.

4.2 The procedure of the efficiency calculation

The efficiency of the events registration for the reactions 1.3 and 1.4 in the WA102 experiment was calculated by a Monte-Carlo method. The distributions for the transversal components p_y and p_z of the initial and final protons measured experimentally were used in the generator of events. The energy of the proton beam can be considered as constantly equal to 450 GeV with a good accuracy. For the calculation of the axial component of p_f and p_s the distributions of x_F were used. The x-coordinate of the vertex x_v was also modelled. The target was presented by a fixed proton. If we know the momenta of the protons in the initial and final states and the point of interaction then we can completely define the kinematics of the reaction. p_y, p_z, x_F and x_v were simulated so that after passing the particles through the experimental setup the distributions of the obtained parameters are identical to the ones measured experimentally. The kinematics of the events was modelled including the final decays to charged $\pi^{\pm}$ mesons and γs. This method does not require any knowledge of the dynamics of the central pp collisions and so works without any theoretical assumptions.

To calculate the efficiency of the charged particles special tables were filled. These tables define the correspondence between the momentum of the particle, the vertex coordinate and the efficiency of registration. It was required that the simulated events satisfy the same trigger conditions as the experimental ones. That is, the fast proton should pass through the A1 and A2 counters and the slow proton through the TB, the SPC counters and the proportional chambers C. The energy deposits of the slow proton in the target and in the target counters were also calculated. Each $\pi^{\pm}$ meson should pass through the 4 chambers B layers as a minimum to be counted and reconstructed. Gaussian distributions with a width equal to the real resolution of the detectors were used for the simulation of the errors in the measurements of the charged particles. The energy and the coordinate resolutions of the GAMS calorimeter were simulated for γs. γ's energy was shared among the cells of the calorimeter according to the density of the energy distribution in an electromagnetic shower (see 3.3.2). Further, the information from the calorimeter was analysed by the program of γ's reconstruction. Thus the efficiency of the reconstruction program, the errors of simulated parameters, and possible bugs in the program codes were taken in account.

The Monte-Carlo events were recorded in the same format as real data and further analysis was performed using the same programs as the ones used for the experimental events. This procedure of efficiency calculation allows to take into account the experimental set-up, conditions of measurements, and all phases of events reconstruction and selection used in the analysis of real data. The kinematical variables used in the analysis were calculated for the reconstructed and selected Monte-Carlo events: the mass M of the central system, the azimuthal ϕ and the polar θ angles used in the partial-wave analysis, the difference dP_T between the transverse momentum vectors of the exchanged particles, the azimuthal angle ϕ_{pp} between the transversal components of the final protons and others. As it will be shown later in greater detail, in the mass-independent partial-wave analysis the angular distributions $\Omega = (\theta, \phi)$ are analysed separately in each mass interval ΔM_i. The efficiency ε is included to the minimization functional as the following normalized integral

$$\int \varepsilon(\Omega) I(\Omega, \vec{A}) d\Omega, \tag{4.12}$$

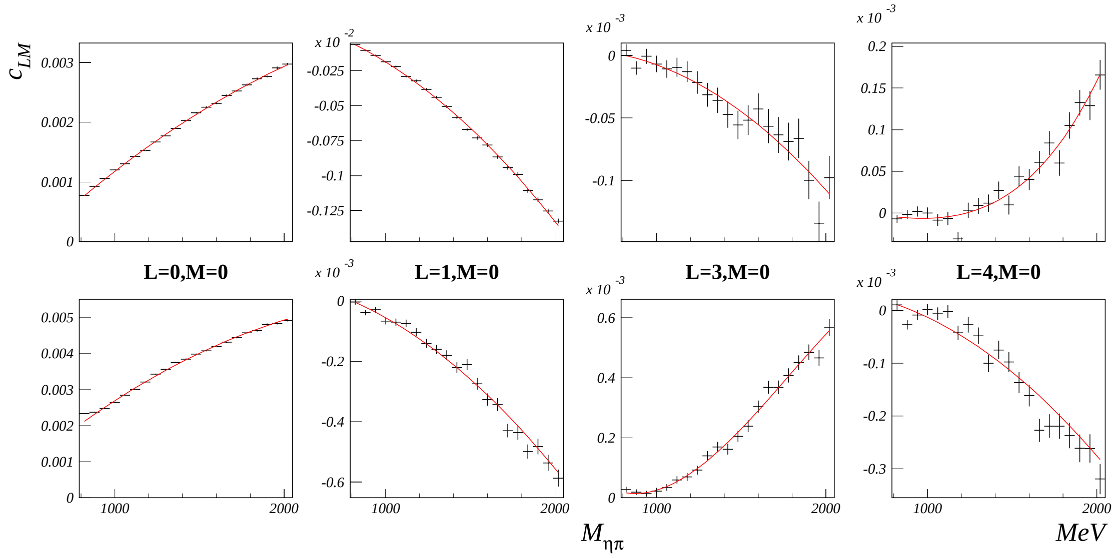

Figure 4.1: Coefficients c_λ of the efficiency for the reactions 1.3 (upper histograms) and 1.4 (lower histograms). The curve shows the aproximation of c_λ by polynomials.

where $I(\Omega, \vec{A})$ is the angular distribution of the experimental events in the mass interval ΔM_i, $\vec{A}$ is the vector of the parameters. $I(\Omega, \vec{A})$ can be written as a Fourier series:

$$I(\Omega, \vec{A}) = \sum_\lambda t_\lambda(\vec{A}) Y_\lambda(\Omega), \tag{4.13}$$

where $Y_\lambda(\Omega) = Y_L^M(\Omega)$ is the system of the orthonormal spherical harmonics. Then the integral 4.12 can be written as:

$$\int \varepsilon(\Omega) \sum_\lambda t_\lambda(\vec{A}) Y_\lambda(\Omega) d\Omega = \sum_\lambda t_\lambda(\vec{A}) \int \varepsilon(\Omega) Y_\lambda(\Omega) d\Omega = \sum_\lambda t_\lambda(\vec{A}) c_\lambda, \tag{4.14}$$

where the coefficients $c_\lambda = \int \varepsilon(\Omega) Y_\lambda(\Omega) d\Omega$ can be calculated as follows:

$$c_\lambda = \frac{4\pi}{N_0} \sum_{i=1}^{N} Y_\lambda(\Omega_i), \tag{4.15}$$

where N_0 is the number of Monte-Carlo events in the interval ΔM_i , N is the number of those events which have passed all stages of selection. The precision of the calculations of the coefficients 4.15 is characterized by the dispersion:

$$\sigma_\lambda^2 = \frac{16\pi^2}{N_0^2} \sum_{i=1}^{N} (Y_\lambda(\Omega_i) - \frac{N_0}{4\pi N} c_\lambda)^2. \tag{4.16}$$

In each mass interval the number of events N exceeded by two orders of magnitude the number of experimental events that allowed the calculation of the coefficients with a precision sufficient to ignore the statistical errors of this efficiency calculation in the partial-wave analysis. The coefficients c_λ of the efficiency calculated for the reaction 1.3 are presented for some spherical harmonics in the figure 4.1. It is necessary to note that the formula 4.15 can be used only for non-zero efficiency in all area $\Omega = 4\pi$, that was observed for all studied mass intervals ΔM_i for both reaction 1.3 and 1.4.

4.3 The partial-wave analysis

The technique of a partial-wave analysis (PWA) of two pseudoscalar particles is designed explicitly enough and is described for peripheral reactions such as 2.1 and 2.2 (see, for example, [83]-[90]). The most detailed description of the method can be found in [91]. The key moments of a PWA of two pseudoscalar particles for double exchange reactions in proton-proton collisions 4.1 will be discussed briefly in the present chapter. The technique of the analysis in this case differs mathematically a little from that described in [91]. The coordinate frame for the analysis is defined differently and the superpositions of waves with different spin projections in reaction 4.1 do not connect with naturality of exchange as in peripheral reactions.

4.3.1 The theoretical foundation of a PWA

The axes for a PWA of the central production reaction 4.1 is defined in analogy with the Gottfried-Jackson axes [92] for peripheral reactions. Let a_s and a_f represent the exchanged particles refering the slow and the fast proton respectively. In the reaction 4.1 a_s and a_f interact and produce the central particle X:

$$a_s a_f \to X.$$

The azimuthal ϕ and polar θ angles in the PWA are defined in the X rest frame. The direction of the axis z is chosen to be along the direction of one of the exchanged particles; the axis y is defined as being perpendicular to the plane formed by the momentums of this exchanged particle and the corresponding final proton, p_f or p_s; $\vec{x} = \vec{y} \times \vec{z}$. In the X rest frame the fast and slow protons are indistinguishable but

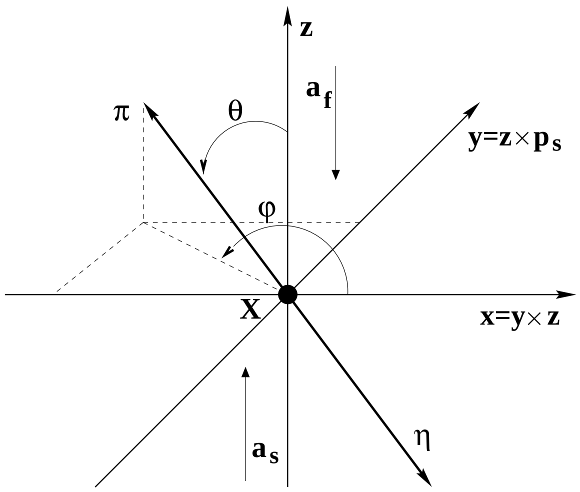

Figure 4.2: Definition of axes for a PWA of two scalar particles in central production reactions.

in practice the slow vertex is better measured than the fast one. For this reason the axis z is defined using the exchanged particle a_s.

The above-mentioned coordinate frame is shown in the figure 4.2. The angular distribution of the reaction (4.1) in this system can be expanded in terms of partial amplitudes V_{lmk} [91]

$$I(\Omega) = \sum_k |U_k(\Omega)|^2 = \sum_k \left| \sum_{lm} V_{lmk} Y_l^m(\Omega) \right|^2 = \sum_k \left| \sum_{lm} \sqrt{\frac{2l+1}{4\pi}} V_{lmk} D_{m0}^{l*}(\phi, \theta, 0) \right|^2 ,$$

where l is the spin of the central particle X, m is the spin value with respect to the z-axis, k represents the spin degrees of freedom for the initial and final nucleons ($k = 1, 2$ for spin-flip and spin-nonflip amplitudes), $D_{m0}^l(\phi, \theta, 0)$ are the Wigner D-functions [93], $Y_l^m(\Omega) = \sqrt{\frac{2l+1}{4\pi}} D_{m0}^{l*}(\phi, \theta, 0)$ are the spherical harmonics.

The angular distribution can be also expanded in terms of the moments H_{LM}:

$$I(\Omega) = \sum_{LM} \frac{2L+1}{4\pi} H_{LM} D_{M0}^{L*}(\phi, \theta, 0), \tag{4.17}$$

which can be expressed in terms of the density matrix elements

$$\rho_{mm'}^{ll'} = \sum_k V_{lmk} V_{l'm'k}^* \tag{4.18}$$

as follows

$$H_{LM} = \sum_{\substack{lm \\ l'm'}} \sqrt{\frac{(2l'+1)}{(2l+1)}} \rho^{ll'}_{mm'} \langle l'm'LM|lm\rangle \langle l'0L0|l0\rangle, \tag{4.19}$$

where $\langle l'm'LM|lm\rangle$ are the Clebsch-Gordan coefficients [93]. The symmetry relations for the moments H_{LM} are well known. From the hermiticity of the ρ-matrix, one gets

$$H^*_{LM} = (-1)^M H_{L-M} \tag{4.20}$$

and, from parity conservation in the production process, one finds

$$H_{LM} = (-1)^M H_{L-M}. \tag{4.21}$$

The equations (4.20) and (4.21) show that the moments H_{LM} are real. The angular distribution (4.17) can now be re-written as

$$I(\Omega) = \sqrt{\frac{2L+1}{4\pi}} \sum_{LM} \tau_M H_{LM} \mathrm{Re}\left\{Y_{LM}(\Omega)\right\}, \tag{4.22}$$

where the connection between the D-functions and the spherical harmonics $Y_{LM}(\Omega)$ (see [93]) is taken into account, $\tau_M = 2$ at $M > 0$, $\tau_M = 1$ at $M = 0$ and $\tau_M = 0$ at $M < 0$. In many works ([18], [22], [84] and others) the moments $t_{LM} = \sqrt{(2L+1)/4\pi} H_{LM}$ are used for a PWA. In the terms t_{LM} the angular distribution looks as:

$$I(\Omega) = \sum_L \left\{ t_{L0} Y_{L0}(\Omega) + 2 \sum_M t_{LM} \, \mathrm{Re}\, Y_{LM}(\Omega) \right\}. \tag{4.23}$$

Since the spherical harmonics form a complete orthonormal set in the space $\Omega = (\theta, \phi)$, they define uniquely an angular distribution of the reaction (4.1).

The important assumption is made regarding this PWA description, necessary for carrying out the amplitude analysis, that the projection of the spin l on the z axis can have two values only: 0 or 1, i.e. the amplitudes V_{lmk} with $m > 1$ are equal to zero. Thus, the index M in the moments H_{LM} can be equal to 0, 1 or 2. Also, one makes the second assumption that if the production amplitudes V_{lmk} do not depend on k, then $\rho^{ll'}_{mm'} = V_{lm} V^*_{l'm'}$ (see 4.18). For the partial amplitudes V_{lm} one introduces the notations:

$$V_{00} = S_0, \quad V_{1m} = P_m, \quad V_{2m} = D_m, \quad ... \tag{4.24}$$

The dependences of the angular momentums H_{LM} on the partial waves are defined by a set of 12 equations:

$$\begin{aligned}
H_{00} &= S^2 + P_0^2 + P_{-1}^2 + P_{+1}^2 + D_0^2 + D_{-1}^2 + D_{+1}^2 \\
H_{10} &= \tfrac{2}{\sqrt{3}} SP_0 + \tfrac{4}{\sqrt{15}} P_0 D_0 + \tfrac{2}{\sqrt{5}}(P_{+1}D_{+1} + P_{-1}D_{-1}) \\
H_{11} &= \tfrac{1}{\sqrt{3}}(P_{+1}S - P_{-1}S) + \tfrac{1}{\sqrt{5}}(D_{+1}P_0 - D_{-1}P_0) - \tfrac{1}{\sqrt{15}}(P_{+1}D_0 - P_{-1}D_0) \\
H_{20} &= \tfrac{2}{\sqrt{5}} SD_0 + \tfrac{2}{5}P_0^2 - \tfrac{1}{5}(P_{+1}^2 + P_{-1}^2) + \tfrac{2}{7}D_0^2 + \tfrac{1}{7}(D_{+1}^2 + D_{-1}^2) \\
H_{21} &= \tfrac{\sqrt{3}}{5}(P_{+1}P_0 - P_{-1}P_0) + \tfrac{1}{\sqrt{5}}(D_{+1}S - D_{-1}S) + \tfrac{1}{7}(D_{+1}D_0 - D_{-1}D_0) \\
H_{22} &= -\tfrac{\sqrt{6}}{5}P_{+1}P_{-1} - \tfrac{\sqrt{6}}{7}D_{+1}D_{-1} \\
H_{30} &= \tfrac{6\sqrt{3}}{7\sqrt{5}}P_0D_0 - \tfrac{6}{7\sqrt{5}}(P_{+1}D_{+1} + P_{-1}D_{-1}) \\
H_{31} &= \tfrac{3\sqrt{2}}{7\sqrt{5}}(P_{+1}D_0 - P_{-1}D_0) + \tfrac{2\sqrt{6}}{7\sqrt{5}}(D_{+1}P_0 - D_{-1}P_0) \\
H_{32} &= -\tfrac{\sqrt{6}}{7}(P_{+1}D_{-1} + P_{-1}D_{+1}) \\
H_{40} &= \tfrac{2}{7}D_0^2 - \tfrac{4}{21}(D_{+1}^2 + D_{-1}^2) \\
H_{41} &= \tfrac{\sqrt{10}}{7\sqrt{3}}(D_{+1}D_0 - D_{-1}D_0) \\
H_{42} &= -\tfrac{2\sqrt{10}}{21}D_{+1}D_{-1}
\end{aligned} \tag{4.25}$$

In a PWA of peripheral reactions some new basic amplitudes are introduced:

$$P_+ = \frac{1}{\sqrt{2}}(P_{+1} + P_{-1}), \qquad D_+ = \frac{1}{\sqrt{2}}(D_{+1} + D_{-1}),$$

$$P_- = \frac{1}{\sqrt{2}}(P_{+1} - P_{-1}), \qquad D_- = \frac{1}{\sqrt{2}}(D_{+1} - D_{-1}).$$

In peripheral reactions such superpositions of amplitudes have a concrete physical content: the P_+ and D_+ waves describe an exchange with so-called natural spin-parity in the t channel of the reaction, and the S, P_0, D_0, P_- and D_- waves correspond to an exchange with unnatural spin-parity[1]. Although in the central production reaction 4.1 the waves do not connect with the naturality of the exchange, for the uniformity of the description and the capability of comparing the results, the PWA for central production reactions is also performed on a new basis. Besides, following the above mentioned convention, the moments t_{LM} are used. In this case the set of equations

[1]A natural spin-parity=$(-1)^J$, unnatural spin-parity = $(-1)^{J+1}$, where J is the spin of the exchanged particle.

4.25 becomes:

$$\begin{aligned}
\sqrt{4\pi}t_{00} &= S^2 + P_0^2 + P_-^2 + P_+^2 + D_0^2 + D_-^2 + D_+^2 \\
\sqrt{4\pi}t_{10} &= 2SP_0 + \tfrac{4}{\sqrt{5}}P_0D_0 + 2\sqrt{\tfrac{3}{5}}(P_-D_- + P_+D_+) \\
\sqrt{4\pi}t_{11} &= \tfrac{1}{\sqrt{2}}SP_- + \tfrac{1}{\sqrt{10}}(\sqrt{3}P_0D_- - P_-D_0) \\
\sqrt{4\pi}t_{20} &= 2SD_0 + \tfrac{1}{\sqrt{5}}(2P_0^2 - P_+^2 - P_-^2) + \tfrac{\sqrt{5}}{7}(2D_0^2 + D_+^2 + D_-^2) \\
\sqrt{4\pi}t_{21} &= \tfrac{1}{\sqrt{2}}SD_- + \sqrt{\tfrac{3}{10}}P_0P_- + \tfrac{\sqrt{5}}{7\sqrt{2}}D_0D_- \\
\sqrt{4\pi}t_{22} &= \sqrt{\tfrac{3}{10}}(P_-^2 - P_+^2) + \tfrac{\sqrt{15}}{7\sqrt{2}}(D_-^2 - D_+^2) \\
\sqrt{4\pi}t_{30} &= \tfrac{6}{\sqrt{35}}(\sqrt{3}P_0D_0 - P_-D_- - P_+D_+) \\
\sqrt{4\pi}t_{31} &= \sqrt{\tfrac{3}{14}}(2P_0D_- + \sqrt{3}P_-D_0) \\
\sqrt{4\pi}t_{32} &= \sqrt{\tfrac{3}{14}}(P_-D_- - P_+D_+) \\
\sqrt{4\pi}t_{40} &= \tfrac{6}{7}D_0^2 - \tfrac{4}{7}(D_-^2 + D_+^2) \\
\sqrt{4\pi}t_{41} &= \tfrac{\sqrt{15}}{7}D_0D_- \\
\sqrt{4\pi}t_{42} &= \tfrac{\sqrt{10}}{7}(D_-^2 - D_+^2),
\end{aligned} \tag{4.26}$$

where $A_iA_j = |A_i||A_j|\cos(\phi_i - \phi_j)$, $A_i^2 = |A_i|^2$. The system 4.26 of 12 equations includes 12 variables: 7 amplitudes squared $|S|$, $|P_0|$, $|P_-|$, $|P_+|$, $|D_0|$, $|D_-|$, $|D_+|$ and 5 relative phases ϕ_{SD_0}, $\phi_{P_-D_0}$, $\phi_{P_0D_0}$, $\phi_{D_-D_0}$, $\phi_{P_+D_+}$. Here one uses ϕ_{D_0} and ϕ_{P_+} as the basic phases, i.e. the others are measured relatively to ϕ_{D_0} and ϕ_{P_+}.

4.3.2 Ambiguities in the partial waves

In terms of amplitudes in the PWA, there is an ambiguity in the solutions caused by the nonlinearity of the equations 4.26 expressing the moments t_{LM} through amplitudes and phases. In [90] a method for calculating all solutions for the PWA of two scalar particles was found. The problem was solved for the $\eta\pi^o$ system and it was proved that 8 nontrivial solutions exist for S, P and D waves. In [91] this method is presented in more detail, the general case and some particular examples for different sets of waves are studied.

As mentioned above, in the analysis of the partial amplitudes the assumption was made that the production amplitudes do not depend on k. It means the identity of spin-flip and spin-nonflip amplitudes. As a result, the angular distribution can be presented as the sum of two non-interfering terms:

$$I(\Omega) = \left|U^{(+)}(\Omega)\right|^2 + \left|U^{(-)}(\Omega)\right|^2 . \tag{4.27}$$

It is convenient to separate out the θ dependences from the ϕ ones for the amplitudes $U^{(+)}(\Omega)$ and $U^{(-)}(\Omega)$, corresponding to natural and unnatural spin-parity exchange in the t-channel of the peripheral reactions, as follows:

$$U^{(-)}(\Omega) = \frac{1}{\sqrt{4\pi}}\Big[h_0(\theta) + h_-(\theta)\cos\phi\Big], \tag{4.28}$$

$$U^{(+)}(\Omega) = \frac{1}{\sqrt{4\pi}}\Big[h_+(\theta)\sin\phi\Big], \tag{4.29}$$

where

$$h_0(\theta) = SP_0^0(\cos\theta) + \sqrt{3}P_oP_1^0(\cos\theta) + \sqrt{5}D_oP_2^0(\cos\theta), \tag{4.30}$$

$$h_-(\theta) = \sqrt{3}P_-P_1^1(\cos\theta) + \sqrt{\frac{5}{3}}D_-P_2^1(\cos\theta), \tag{4.31}$$

$$h_+(\theta) = \sqrt{3}P_+P_1^1(\cos\theta) + \sqrt{\frac{5}{3}}D_+P_2^1(\cos\theta). \tag{4.32}$$

Here $P_l^m(x)$ are the associated Legendre functions.

In order to examine the ambiguities one introduces a variable $u = tg\theta/2$ and the Gersten functions [94]:

$$g(u) = \frac{1}{\sqrt{2}}\Big[h_0(u) + h_-(u)\Big], \tag{4.33}$$

which can be prolonged in the negative area of the variable u in such a way as either the $g(u)$ or its first derivative should be a continuous functions:

$$g(-u) = \frac{1}{\sqrt{2}}\Big[h_0(u) - h_-(u)\Big]. \tag{4.34}$$

Using (4.30) and (4.31) one can express the g-function through the amplitudes of the S, P_0, P_-, D_0 and D_- waves:

$$\begin{aligned} G(u) = (1+u^2)^4 g(u) = & \quad\quad (S + \sqrt{3}P_0 + \sqrt{5}D_0) \\ & + \; u \quad (2\sqrt{3}P_- + 2\sqrt{15}D_-) \\ & + \; u^2 \quad (4S + 2\sqrt{3}P_0 - 2\sqrt{5}D_0) \\ & + \; u^3 \quad (6\sqrt{3}P_- + 2\sqrt{15}D_-) \\ & + \; u^4 \quad (6S - 6\sqrt{5}D_0) \end{aligned} \tag{4.35}$$

The function $G(u)$ represents a polynomial of degree eighth which can be written as follows

$$G(u) = \sum_{i=0}^{4} a_i u^i = c_0 \prod_{k=1}^{8} (u - u_k), \tag{4.36}$$

where a_i are some complex polynomial coefficients and u_k are the complex roots of the polynomial. From 4.35 and 4.36 one can find the following set of equations for the coefficients of the polynomial $G(u)$:

$$\begin{aligned}
a_0 &= (S + \sqrt{3}P_0 + \sqrt{5}D_0) \\
a_1 &= (2\sqrt{3}P_- + 2\sqrt{15}D_-) \\
a_2 &= (4S + 2\sqrt{3}P_0 - 2\sqrt{5}D_0) \\
a_3 &= (6\sqrt{3}P_- + 2\sqrt{15}D_-) \\
a_4 &= (6S - 6\sqrt{5}D_0).
\end{aligned} \tag{4.37}$$

Now that we have a theoretical basis to calculate all solutions, the algorithm is described below. At first, one of the solutions is fond by numerical methods which will be discussed in the next section. Using equations 4.37 and the first solution, the coefficients a_i of the polynomial 4.36 are calculated. Then one can find the 4 complex polynomial roots by numerical methods and sort out all possible combinations of the roots by substituting one or several roots with their complex conjugates. A new set of coefficients a_i is calculated for each combination. Solving the linear system of equations 4.37 one find the set of the S, P_0, P_-, D_0 and D_- waves corresponding to these coefficients. In total, $2^4 = 16$ different combinations of roots exist. As shown in [90], the replacement of any complex root u_k by its conjugate partner does not change the angular distribution, therefore only 8 solutions remain out of 16. Thus, in the model of S, P and D waves there are 8 nontrivial solutions.

The amplitudes of the P_+ and D_+ waves and their relative phase for each solution can be found using the moments 4.26:

$$\begin{aligned}
|D_+|^2 &= |D_-|^2 - \frac{7}{\sqrt{10}}\sqrt{4\pi}t_{42} \\
|P_+|^2 &= |P_-|^2 - \frac{\sqrt{10}}{3}(\sqrt{4\pi}t_{22} - \frac{\sqrt{3}}{4}\sqrt{4\pi}t_{42}) \\
2ReP_+D_+^* &= 2ReP_-D_-^* - \sqrt{\frac{14}{3}}\sqrt{4\pi}t_{32}
\end{aligned} \tag{4.38}$$

If in equations 4.38 for some of the solutions one finds a negative amplitude squared for the P_+ and D_+ waves, or that the module of the cosine of their relative phase is more than 1, then such a solution is rejected, so in practice, the number of solutions can be less than eight. The procedure of the solutions calculation is carried out separately for each mass interval. To find the conformity between the solutions in the nearest bins there is a special "bootstrapping" procedure which will be discussed hereafter.

4.3.3 The functionals of the minimization

As said in the previous section, to calculate 8 solutions in a PWA with the S, P and D waves by analytical methods it is necessary to know just one of these solutions. It is found by numerical methods. We use a method of maximum of likelihood (see, for example, [95]).

The probability that an event has the coordinate $\Omega_i = (\cos\theta_i, \phi_i)$ is equal to $I(\Omega_i)/\int \varepsilon(\Omega)I(\Omega)d\Omega$. The probability of finding n events in a given mass bin is defined by Poisson distribution. The likelihood function is defined by the multiplication of the probabilities:

$$L \propto \frac{\bar{n}^n}{n!}e^{-n}\prod_i^N \frac{I(\Omega_i)}{\int \varepsilon(\Omega)I(\Omega)d\Omega}, \tag{4.39}$$

where $\bar{n} = \int \varepsilon(\Omega)I(\Omega)d\Omega$ is the expectation value for n. The likelihood function can now be written, dropping the factors depending on n alone:

$$L \propto \left[\prod_i^N I(\Omega_i)\right] exp\left[-\int \varepsilon(\Omega)I(\Omega)d\Omega\right]. \tag{4.40}$$

The functional of minimization is a logarithm of the likelihood function taken with a negative sign:

$$F = -lnL = -\sum_{i=1}^N \ln I(\Omega_i) + \int \varepsilon(\Omega)I(\Omega)d\Omega. \tag{4.41}$$

Using the expression 4.14 for the normalization of the likelihood functional the equation 4.41 can be re-written in terms of the angular moments t_λ:

$$F = -\sum_{i=1}^N \ln I(\Omega_i) + \sum_\lambda t_\lambda c_\lambda. \tag{4.42}$$

The required parameters can be either the angular momentums t_λ, uniquely determining the angular distribution 4.13, or directly the squares of the amplitudes and the relative phases defined in terms of the angular momentums by the equations 4.26. The minimum of the likelihood functional was found with the program MINUIT [96] which also allows statistical errors of parameters to be estimated (procedure HESSE [96]).

Approximately one third of the events in the mass spectra of both reactions, 1.3 and 1.4, are background events (see fig. 5.7 and 6.3) which are not rejected at the stage of the selection procedure and kinematical analysis. However, at the partial-wave analysis stage the background can be subtracted. For this purpose the background events are taken in account in the functional of minimization 4.42 with a negative sign [97]:

$$\Phi = -\left[\sum_{i=1}^{N_{ev}} \ln I(\Omega_i) - \sum_{i=1}^{N_{bg}} \ln I(\Omega_i)\right] + \sum_{\lambda} t_\lambda c_\lambda. \tag{4.43}$$

Here N_{ev} is the number of events and N_{bg} is the number of background events in the given mass bin. In this case the normalization of the functional is $\int \varepsilon(\Omega) I(\Omega) d\Omega = N_{ev} - N_{bg}$. The matrix of errors is calculated as follows

$$D = W^{-1} + 2W^{-1}HW^{-1}, \tag{4.44}$$

where

$$\begin{aligned} W_{ij} &= -\frac{\partial^2 L}{\partial\theta_i \partial\theta_j} \\ H_{ij} &= -\sum_{k=1}^{N_{bg}} \frac{\partial \ln I(\Omega_k)}{\partial\theta_i}\frac{\partial \ln I(\Omega_k)}{\partial\theta_j} - \frac{1}{N_{bg}}\left(\sum_{k=1}^{N_{bg}} \frac{\partial \ln I(\Omega_k)}{\partial\theta_i}\right)\left(\sum_{k=1}^{N_{bg}} \frac{\partial \ln I(\Omega_k)}{\partial\theta_j}\right). \end{aligned}$$

Chapter 5

The analysis of the reaction $pp \to p_s(\eta\pi^0)p_f$

This chapter describes the procedure of the events selection and the results of the partial-wave analysis of the central $\eta\pi^0$ production in the proton-proton collisions

$$pp \to p_s(\eta\pi^0)p_f \tag{5.1}$$

with the subsequent decays of η and π^0 to 2γ's. The dP_T, t and ϕ_{pp} (see chapter 1) dependences for the $a_0^0(980)$ and $a_2^0(1320)$ mesons are measured and described.

5.1 Selection of events

In the final state of the reaction 5.1 4 γs and the charged tracks of the fast and slow protons should be observed. Therefore we use events with the absence of tracks from the central particle decay and where the number of γs is more or equal to 4 for the analysis. The events with a number of γs more than 4 are not rejected because the noise of the calorimeter, the background of charged particles, the errors of the reconstruction program and other factors that can result in the appearance of false γs and thus increase the original multiplicity of γs. Such false γs can be rejected from the analysis at further stages. The procedure of selection is described below.

1. Due to energy fluctuations and noise of the electronics the shape of the real electromagnetic shower can differ from the theoretical one. It results in errors

in the γs reconstruction (see chapter 3.3.2); the program can find such false γs. Errors in the reconstruction program were corrected by merging two nearby γs from one cluster ($R_{\gamma\gamma} < 60$ mm) which had simultaneously a small invariant mass ($m_{\gamma\gamma} < 60$ MeV). It is easy to illustrate this selection of events with 2 reconstructed γs. A part of these events ($\sim 6\%$) have actually a single γ. It can be clearly seen in figures 5.1 a) and b), that their invariant masses lie lower than the π^0 mass. The square in the left lower corner of the histogram 5.1 b) selects the events excluded from the analysis. In the case of 2 γs one could use only the selection on their invariant masses. In the case, for example, of 4 γs there are 6 $\gamma\gamma$ combinations and there is a high probability that the mass of some combinations will be large, but the distance between γs is also large enough and thus such γ pairs cannot appear due to errors in the reconstruction program. Therefore, one uses an additional selection on the distances between γs in pair together with a selection on their invariant masses.

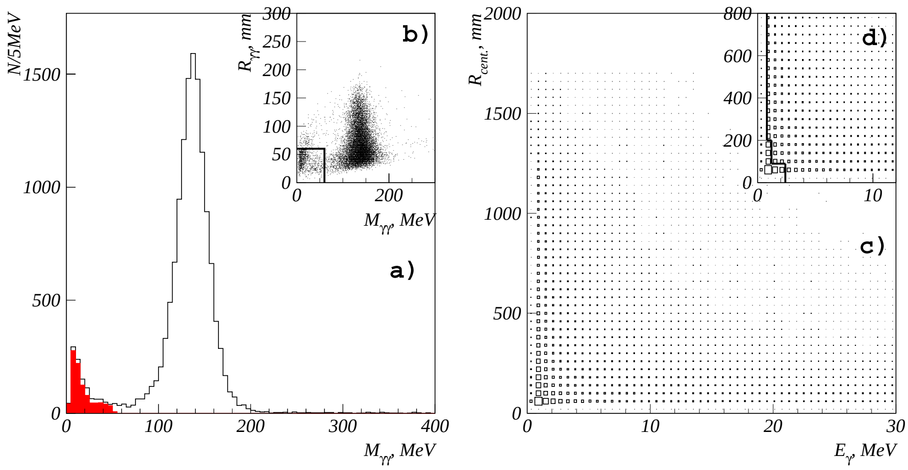

Figure 5.1: a) Mass spectrum of reconstructed 2γs events, the shaded area shows that events where 2 γs were merged in one γ after selection 1; b) distribution of invariant masses and distances between γs for 2γs events, the solid line shows the boundaries of the selection 1; c) distribution of γ's energies and distances of γ to the centre of the GAMS calorimeter; d) enlarged left lower corner of the histogram c), in which the boundaries of the selection 2 are shown by solid lines (see text).

2. In the WA102 experimental set-up many detectors (proportional and drift chambers and, in the 1996 set-up, the cherenkov counter, see fig. 3.1 and 3.2) were

located between the target and the electromagnetic calorimeter to measure the charged particles. The interaction of such charged particles with the matter of these detectors may cause the emission of electrons, so-called δ-rays. δ-rays produce electromagnetic showers in the GAMS and can be mistaken for γs. These false γs should be observed dominantly in the centre of the electromagnetic calorimeter, because their main source is the fast proton. At fast proton average energy 400 GeV the energy of produced electrons should not exceed 1-2 GeV [98]. In the figure 5.1 c) and d) the 2-dimensional distribution of γ energies and distances of the γ to the centre of the calorimeter are shown. In the area near the centre a concentration of low energy events is observed. Selections

$$\begin{aligned} R < 90\text{mm} \quad &with \quad E_\gamma > 2.4\text{GeV}, \\ 90 < R < 200\text{mm} \quad &with \quad E_\gamma > 1.2\text{GeV}, \\ R > 200\text{mm} \quad &with \quad E_\gamma > 0.8\text{GeV}, \end{aligned} \tag{5.2}$$

are marked in the fig.5.1 d) by the solid line. They effectively supress the δ-rays.

3. Events with a total energy from all cells of the electromagnetic calorimeter of less than 3 GeV were not used in the analysis. This selection is caused by the limited sensitivity of the electronics used in the calorimeter.

Selections 1 and 2 change the multiplicity of γs in the events. The figure 5.2 a) shows the number of the events with a given input multiplicity N_γ^{inp} misinterpreted by the analysis with output multiplicity N_γ^{out}, which can differ from the original one. The efficiency and correctness of this procedure are demonstrated by the example of the events with 3 γs in the initial state. The invariant mass of 3 γs events before selections 1 and 2 is shown in the figure 5.2 b) (unshaded histogram). The signal from the decay $\omega(782) \rightarrow \pi^0\gamma \rightarrow 3\gamma$ should be observed in it and the peak of the π^0 meson should not be seen, because the decay $\pi^0 \rightarrow 3\gamma$ is forbidden by C parity conservation. However, in the spectrum we can see a strong signal of the π^0, which arises due to the mixing of 3 γs events with 2 γs events which have one false γ. In the same figure the shaded histogram demonstrates the spectrum of 3 γs events after selections 1 and 2. The peak of π^0 meson has vanished, i.e. 3 γs events with one false γ change their multiplicity to 2γ (histogram 5.2 c)).

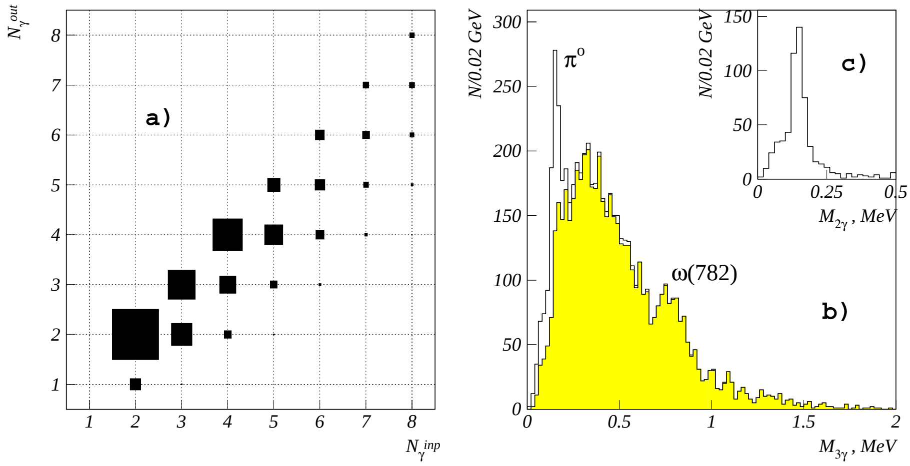

Figure 5.2: a) distribution of the γs multiplicity before (N_γ^{inp})) and after (N_γ^{out})) selections 1 and 2; b) mass of 3γs events before (unshaded histogram) and after (shaded histogram) selections 1 and 2; c) mass spectrum of events changing multiplicity from 3γ to 2γ after the selections 1 and 2.

4. The WA102 experimental set-up does not cover a 4π geometry. This means that there are events where some final state particles could not be detected. To be sure that no incomplete event is accepted by the analysis, the difference between the total momentum of all particles in the final state of reaction 5.1 in the laboratory frame and the momentum of the proton beam is checked to be equal to zero within the limits of errors of measurement:

$$\begin{aligned} |\triangle P_x| &< 17.0\text{GeV/c}, \\ |\triangle P_y| &< 0.16\text{GeV/c}, \\ |\triangle P_z| &< 0.12\text{GeV/c}. \end{aligned} \tag{5.3}$$

   Figure 5.3 illustrates the selection 5.3.

5. After the selections 1, 2, 3 and 4 only 4 γs events were used for the further analysis. The preliminary selection of events of the reaction 5.1 was made before the kinematical fit. Then, the combinations of the gamma pairs in each event were investigated. To select the gamma pair produced by π^0 or η decays, the following mass windows were used:

$$\begin{aligned} \pi^0 :\ 85 < m_{\gamma\gamma} < 185\text{MeV}, \\ \eta : 380 < m_{\gamma\gamma} < 720\text{MeV}. \end{aligned} \tag{5.4}$$

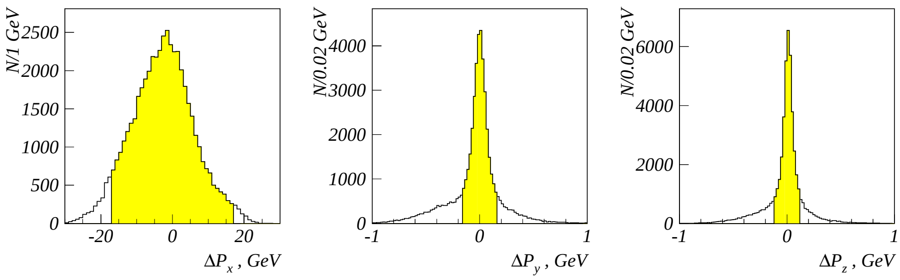

Figure 5.3: The difference between the total momentum of all particles in the final state of the reaction 5.1 and the momentum of the proton beam in the laboratory frame, projection to the axis x (left histogram), y (middle histogram) and z (right histogram). The shaded area shows the selection 5.3.

The broad mass interval for the η meson selection was justified for the background research. Six combinations of gamma pairs can be built with 4 γs. If the invariant mass of one pair is within the η mass window and the other pair is within the π^0 mass window, these four gammas are tagged as $\eta\pi^0$ candidate. Even if in one of the combinations both pairs are within the π^0 window, the event is rejected. Thus the $\pi^0\pi^0$ hypothesis is suppressed. The selected event were then subjected to the kinematical fit described in the chapter 4.1. In

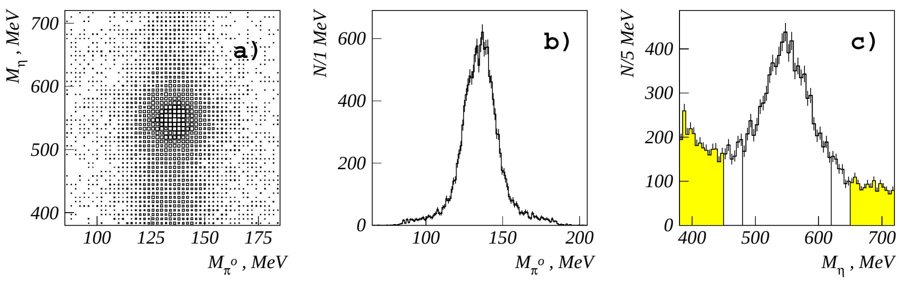

Figure 5.4: Distributions of the $\gamma\gamma$ masses for the events related to the reaction 5.1. In the histogram c) the hatched bands show the events used as background in analysis.

the figure 5.4 the distributions of the $\gamma\gamma$ invariant masses are shown for the events after the selection 5.4. For events 5.4 a) and b) a kinematical 4C-fit was performed using the constraints 4.3 on momentum and mass balance. For events 5.4 c) a 5C-fit was used with an added constraint on the mass of π^0 (first equation in the system 4.2). The events were divided into two groups: 1)

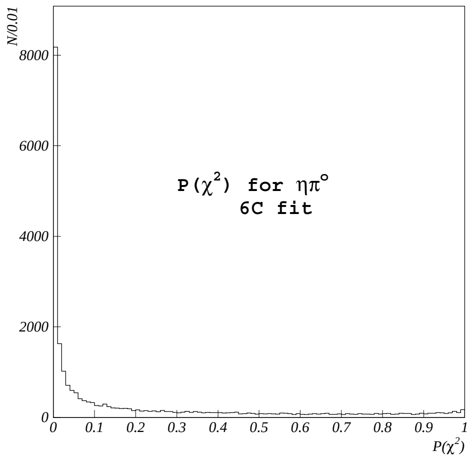

Figure 5.5: Distribution of the probability $P(\chi^2)$ for the $\eta\pi^0$ hypothesis (6C-fit).

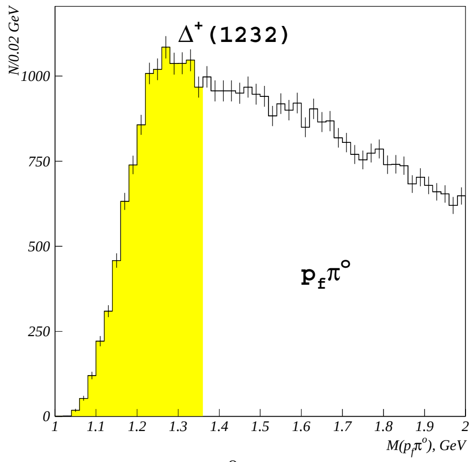

Figure 5.6: $p_f\pi^0$ mass spectrum. The events in the shaded area are rejected from the analysis.

"background" events in the intervals [380,450] MeV and [650,720] MeV (shown by shaded areas in the figure 5.4 c)) and 2) "background+signal" events in the interval [480,620] MeV (shown by clear areas in the figure 5.4 c)). Taking into account that the $\gamma\gamma$ mass dependence for the "background" events is approximately linear and that the sum of the "background" intervals is equal to the interval of the "background+signal" events, then the number of η meson background events is approximately equal to the number of events in the right and left "background" intervals. If we also take into account that the distributions of the background events with a $\eta\pi^0$ mass and with a θ and ϕ angles, used in the PWA, depend weakly and linearly of $\gamma\gamma$ mass, the events in the "background" intervals (shaded intervals in the figure 5.4 c)) can be used for the subtraction of the η background from "background+signal" events to plot the $\eta\pi^0$ mass dependence and perform the PWA of pure "signal" events.

6. For the events in the η mass interval ("background+signal") a 6C kinematical fit was performed with the constraints 4.2 and 4.3. The figure 5.5 shows the distribution of the probability $P(\chi^2)$ of the fit. It is practically flat except for the area near zero which indicates the correctness of the kinematical fit. A cut on $P(\chi^2)$ was not performed to leave the ratio of "background" and "signal" events unaltered. The kinematical fit was only used for the correction of the

kinematical parameters of the events. The dominant background process of $\pi^0\pi^0$ production was suppressed earlier by excluding the events where even in one of the combinations both pairs of $\gamma\gamma$ lie within the π^0 mass interval. The selection 5 suppressed the contribution of other background processes, as $\eta'\pi^0$, $\eta\eta$, $\eta'\eta$ and $\eta'\eta'$ productions, to less than 0.1%.

7. In the chapter 3.2 a mention was made of the background process of the "forward" diffraction which is not suppressed at the trigger level and left for the "off-line" analysis. In the reaction 5.1 a weak $\Delta^+(1232)$ signal was observed in the $p_f\pi^0$ spectrum, see the figure 5.6. To reject the process of the $\Delta^+(1232)$ production from the further analysis a selection $M_{p_f\pi^0} < 1.35$ GeV was used.

In total, 6045 events of the reaction 5.1 were selected after the cuts 1-7. The kinematical variables for further analysis (the $\eta\pi^0$ invariant mass, the polar θ and the azimuthal ϕ angles used in the PWA, the azimuthal angle ϕ_{pp} between the transversal momentums of the protons in the final state, the difference dP_T between the transversal momentums of the exchanged particles) were calculated for each selected event. The figure 5.7 a) shows the $\eta\pi^0$ invariant mass plotted for the selected events, corrected for the efficiency and rescaled to the total number of selected events. The shaded histogram is the estimation of the background. The background is estimated around 40% from the total number of events. The figure 5.7 b) shows the background-subtracted mass spectrum. On inserts 5.7 b) and d) there are the same distributions, as on the main histograms, but not corrected for efficiency. The efficiency of events registration, as a function of $\eta\pi^0$ mass, is proportional to the coefficient $c_{00}(m)$, which is shown in the figure 4.1 for the reaction 5.1.

There is a clear evidence for the $a_0^0(980)$ and $a_2^0(1320)$ resonances in the $\eta\pi^0$ mass spectrum. To determine the parameters of these resonances a fit to the efficiency corrected mass spectrum has been performed using a parametrisation of the form

$$\frac{dN}{dm}(m) = G(m) + a_1|B_1(m,0)|^2 + a_2|B_2(m,2)|^2, \tag{5.5}$$

where

$$G(m) = (m - m_{thr})^{\alpha} e^{-\beta m - \gamma m^2} \tag{5.6}$$

represents the background. Here m is the $\eta\pi^0$ mass, m_{thr} is the $\eta\pi^0$ mass threshold, a_n is the amplitude of a nth resonance, a_n, α, β and γ are parameters to be determined

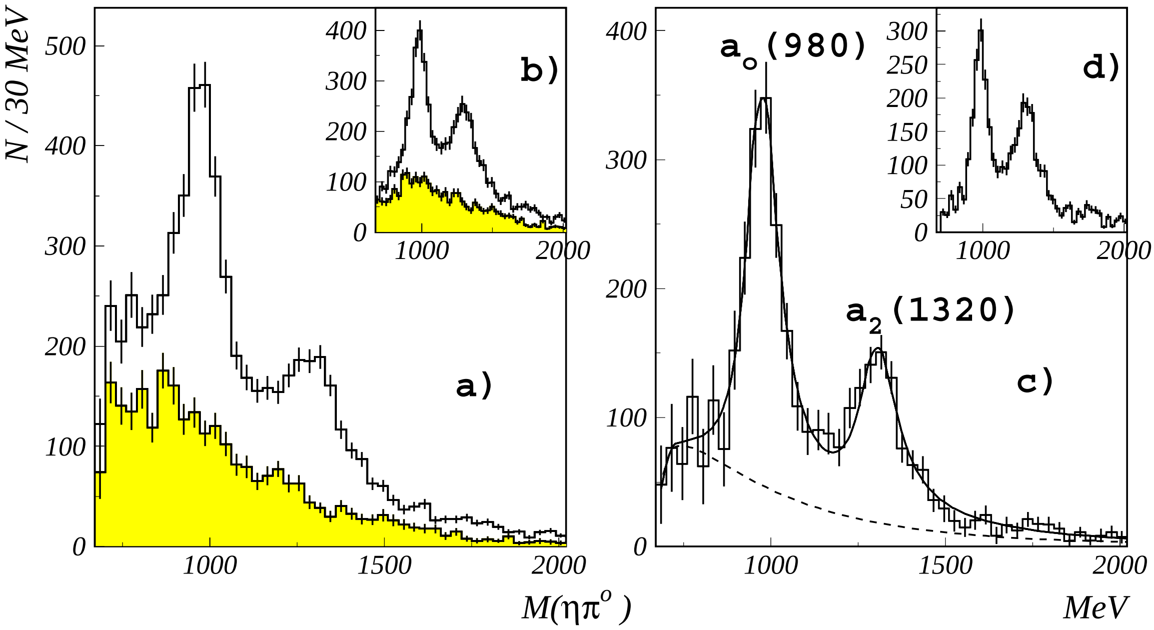

Figure 5.7: a) $\eta\pi^0$ mass spectrum corrected for efficiency and normalised to the total number of selected events. Indicated as a shaded histogram is the estimation of the background contribution. c) The efficiency-corrected, background-subtracted $\eta\pi^0$ mass spectrum. The curve is the result of the fit by the function 5.5 (the dotted line represents a non-resonant contribution to the mass spectrum). Insets b) and d) are the same distributions as a) and c) but they are not corrected for efficiency.

from the fit. A relativistic Breit-Wigner function [99] is used for the parametrisation:

$$B(m,l) = \left(\frac{q}{m^3}\right)\sqrt{2l+1}\frac{m_R\Gamma}{m_R^2 - m^2 - im_R\Gamma}, \tag{5.7}$$

$$\Gamma = \Gamma_R\left(\frac{q}{q_R}\right)^{2l+1}\frac{D_l(q_R r)}{D_l(qr)}, \tag{5.8}$$

where q is the momentum of the π^o (η) meson in the ($\eta\pi^0$) rest frame; l, m_R and Γ_R are the spin value with respect to any arbitrary axis, the mass and the width of the resonance respectively; q_R is the momentum of the π^o (η) meson at $m = m_R$; r is the radius of the interaction which has been set equal to 1 fm[1]; $D_l(x)$ is the Blatt-Weiskopf barrier function ($D_0(x) = 1$, $D_2(x) = 9 + 3x^2 + x^4$); $\frac{q}{m^3}$ is the kinematical factor for central production reactions [100]. The function 5.5 has been convoluted

[1]The result of the fit does not depend strongly of this parameter.

with a Gaussian to take in account the experimental mass resolution:

$$\zeta(x, m) = C \exp\left\{-\frac{(x-m)^2}{2\sigma^2(x)}\right\}, \tag{5.9}$$

where $\sigma(m)$ is the experimental $\eta\pi^0$ mass resolution approximated by a linear function rising from 20 MeV at the $\eta\pi^0$ threshold (682 MeV) to 40 MeV at 2 GeV.

The fit is shown in the figure 5.7 c) and gives the following parameters for the $a_0^0(980)$ and $a_2^0(1320)$ resonances:

$$\begin{aligned} M(a_0^0(980)) &= 975 \pm 7 \text{ MeV}, & \Gamma(a_0^0(980)) &= 72 \pm 16 \text{ MeV}, \\ M(a_2^0(1320)) &= 1308 \pm 9 \text{ MeV}, & \Gamma(a_2^0(1320)) &= 115 \pm 20 \text{ MeV}. \end{aligned} \tag{5.10}$$

These parameters of the resonances are consistent with those quoted in the PDG [20]. The fit of the $\eta\pi^0$ mass spectrum gives the following value for the production ratio of the $a_0^0(980)$ and $a_2^0(1320)$:

$$\frac{\sigma(pp \to pp[a_0^0(980) \to \eta\pi^0])}{\sigma(pp \to pp[a_2^0(1320) \to \eta\pi^0])} = 2.0 \pm 0.3 \tag{5.11}$$

It is interesting to note that the production ratio for the $a_0^0(980)$ and the $a_2^0(1320)$ in central production reactions differs essentially from those observed in charge exchange reactions [23], where the $a_2^0(1320)$ production is $\approx$7 times larger than the $a_0^0(980)$ one.

5.2 The partial-wave analysis

A PWA has been performed in the mass interval from 670 to 2050 MeV for the $\eta\pi^0$ system produced in the reaction 5.1. The angular distributions have separately been analysed in 60 MeV intervals. The technique of the PWA for central production reactions in the model of S, P and D waves is described explicitly in the chapter 4.3. The analysis of the angular distributions has been done both in terms of angular momentums and in terms of amplitudes and phases of partial waves. As the background level was substantial (40%), the PWA has been performed with background subtraction as explained before (see subsection 4.3.3). The angular momentums t_{LM} can be found in the PWA without ambiguities. Using the minimization functional 4.42 the angular momentums t_{LM}^{bg} for "background" events and t_{LM}^{bg+sig} for "background+signal" events were calculated. They are shown in the figures 5.9 and 5.8 accordingly. Subtracting

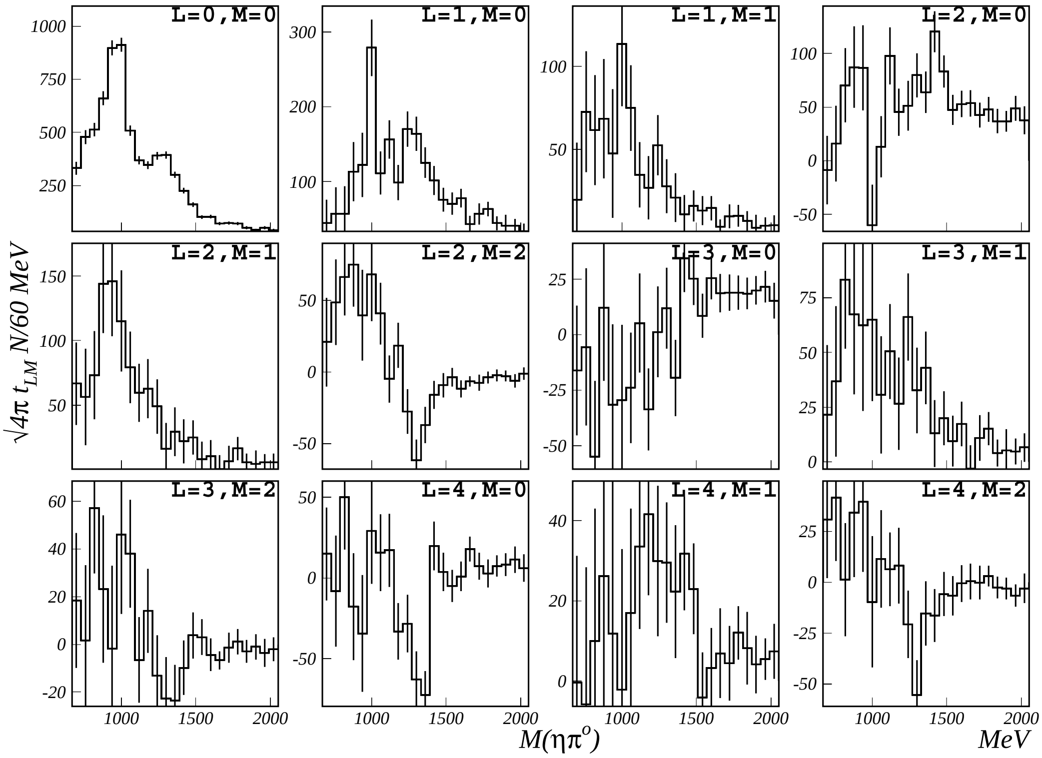

Figure 5.8: Angular momentums t_{LM}^{bg+sig} for "background+signal" events of the reaction 5.1.

from t_{LM}^{bg+sig} the momentums t_{LM}^{bg} one obtains the momentums t_{LM}^{sig} for events with the subtracted background. They are presented in the figure 5.10. The momentums t_{LM}^{sig} can be also calculated using the functional 4.43. The results of both methods coincide within the statistical errors.

A PWA in the terms of amplitudes squared of S, P and D waves and their relative phases can also be performed by 2 ways: 1) with the functional 4.43, where the t_{LM} are substituted by their expressions in amplitudes and phases of the partial waves (equations 4.26) or 2) using the momentums t_{LM}^{sig}, where background events are already subtracted. In the second case it is necessary to find one of the solutions of the system 4.26, where the left side of the equations are the momentums t_{LM}^{sig} measured with the errors σ_{LM}. For this purpose the function

$$\chi^2 = \frac{(t_{LM}^{sig} - t_{LM})^2}{\sigma_{LM}^2}$$

is minimized. The solution can be used as initial parameters for the minimization of

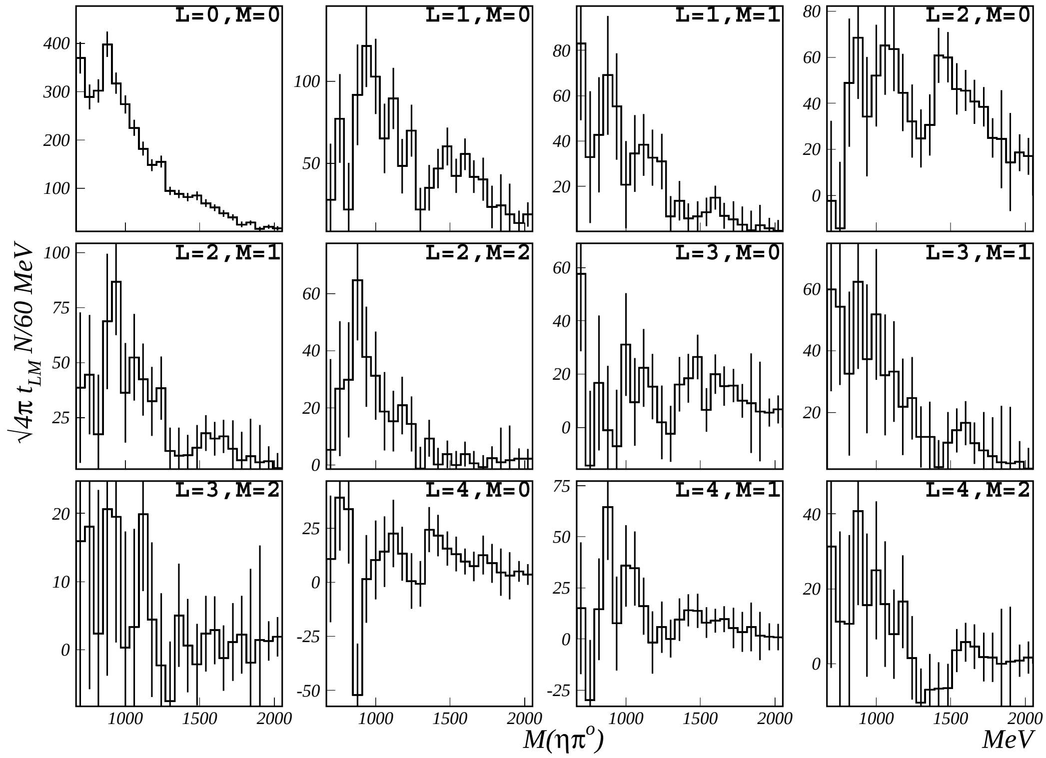

Figure 5.9: Angular momentums t_{LM}^{bg} for "background" events of the reaction 5.1.

the functional 4.43. Both methods give results which are similar within their errors.

Further, the 7 remaining solutions have been found for each mass bin using the first solution. The procedure of the solution calculations in a model of S, P and D waves is explicitely described in the chapter 4.3.2. When all 8 solutions are calculated for each mass bin, it is necessary to "bootstrap" them. It means that one needs to connect the solutions in the adjacent bins for each of the 12 parameters and as a result to obtain 8 smooth curves, one of which being the physical solution. 2 methods of solutions "bootstrapping" are known: first, by the imaginary and the real parts of the roots of the complex polynomial 4.36 and, second, by the obtained solutions directly, using the criteria of the minimum distance and(or) the minimum curvature between the solutions in the adjacent bins. Both methods are applied and described explicitly in [101]. They work well in the case, for example, of two solutions (model S and D waves) or when the errors on the "bootstrapped" parameters are small enough to allow the solutions to be separated. If one succeeded in "bootstrapping" solutions,

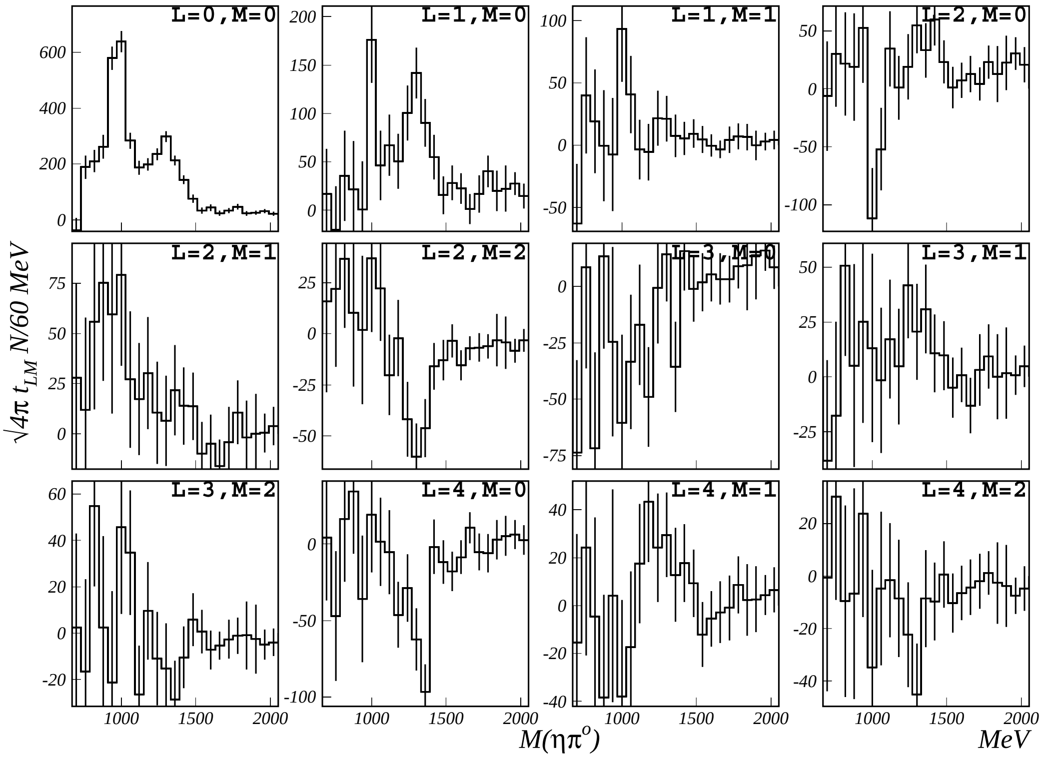

Figure 5.10: Angular momentums t_{LM}^{sig} for "signal" events of the reaction 5.1.

the next step, to select among them the physical one, is a difficult problem. It can be done using some a priori physical principles. The physical solution should fit to these principles, for example, the waves with high spins should be suppressed near the threshold of the studied system. Or, for example, in [37] for the "bootstrapping" it is used the fact that the ratio of the $a_2^0(1320)$ meson productions in the natural and unnatural spin-parity exchanges in the t-channel of the reaction 2.1 should decrease as $p^{-\alpha}$, where p is the beam momentum. Using the results of the previous measurements at different energies, in [37] the needed ratio was found for 38 GeV and used for the selection of the physical solution.

In our case it was not possible to use any of the methods listed above to "bootstrap" the solutions, because the small statistics leads to large errors in the measured parameters overlapping the space between solutions for many mass bins. The figure 5.11 illustrates the "bootstrapping" procedure. The histograms show the amplitudes

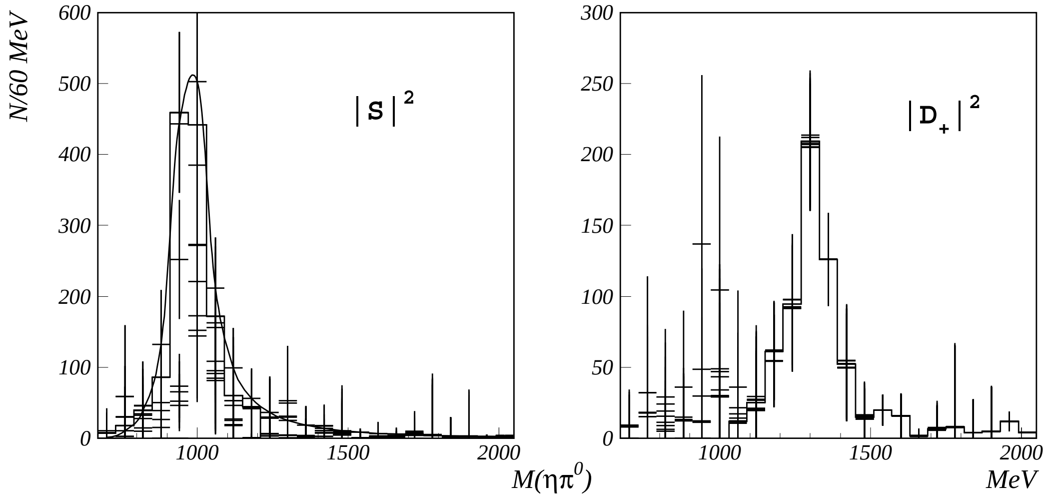

Figure 5.11: Illustration of the "bootstrapping" procedure. The histograms show all solutions from the PWA of the $\eta\pi^0$ events for the amplitudes squared of the S and D_+ waves. The curve on the histogram $|S|^2$ is the Breit-Wigner function obtained by the fit of the $a_0^0(980)$ peak in the $\eta\pi^0$ mass spectrum. The histograms, indicated by the solid line, demonstrates the selected solutions.

squared of the S and D_+ waves. In each mass bin all solutions are plotted[2]. The studied mass region can be divided into two areas according to the nature of the solution's ambiguity: below and above 1.2 GeV. In the mass region above 1.2 GeV, because the D_+ wave is the dominant contribution, the solutions are not affected by the ambiguities and the 8 solutions are identical within their errors. In this area the solutions were not "bootstrapped", but the method used earlier in [18] and [24] is applied: let's denote x_{min} and x_{max} the minimum and maximum solutions in the given mass bin, the required solution is calculated as the mean value between the maximum and minimum solutions:

$$x_0 = \frac{x_{max} + x_{min}}{2}. \tag{5.12}$$

Its error is calculated as follows:

$$\sigma_{x_0} = \frac{x_{max} - x_{min}}{2} + \sigma_x, \tag{5.13}$$

where $\sigma_x = max(\sigma_{x_{min}}, \sigma_{x_{max}})$, that is, it overlaps the errors of all 8 solutions from the higher to the lower one.

[2]Let's remind that the number of solutions can be ≤ 8 (see 4.3.2).

The threshold region, below 1.2 GeV, suffers from ambiguities. The large errors of the measured parameters do not allow the solutions with high confidence to be separated. In the search for the physical solution one makes the evident supposition that the peak in the $\eta\pi^0$ mass spectrum near 1 GeV is completely produced by the $a_0^0(980)$ resonance. The $a_0^0(980)$ has a spin 0 and should appear in the S wave only, therefore we have picked the physical solution in which the $a_0^0(980)$ is in the S wave. The right histogram in the figure 5.11 illustrates this procedure. The solution, lying more closely to the Breit-Wigner curve fitting of the $a_0^0(980)$ resonance in the $\eta\pi^0$ mass spectrum (fig. 5.7 c)), has been chosen as the physical one.

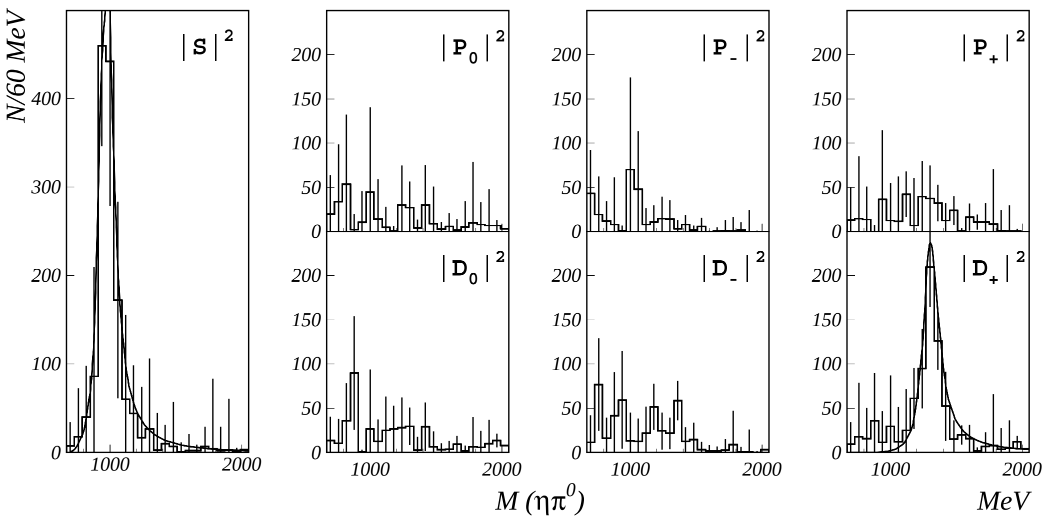

Figure 5.12: The physical solution from the PWA of the events related to the reaction 5.1. The curves on the histograms $|S|^2$ and $|D_+|^2$ are Breit-Wigner functions fit of the peaks of the $a_0^0(980)$ and the $a_2^0(1320)$ resonances in the $\eta\pi^0$ mass spectrum.

The physical solution from the PWA of the events of the reaction 5.1, obtained by this method, is shown in the figure 5.12[3]. As it can be seen the D_+ wave dominates above 1.2 GeV. The fit of the D_+ wave amplitude squared with a Breit-Wigner function gives the parameters for the $a_2^0(1320)$ meson similar to the ones from the fit of the efficiency corrected mass spectrum 5.10. A fit of the S wave amplitude squared gives parameters for the $a_0^0(980)$ also similar to those from a fit of the mass spectrum. There is no evidence for an $a_0^0(1450)$ nor $a_2^0(1660)$. As it can be seen there is no

[3]The relative phases of the partial waves have large statistical errors due to the small statistics, and will not be discussed in this thesis.

evidence for other significant structures in any other waves. The remaining waves, including some exotic P wave, are statistically insignificant.

5.3 Study of the dP_T, t and ϕ_{pp} dependences

As already mentioned in the introduction, in the previous WA102 analyses it has been observed that centrally produced states have different dP_T dependences, where dP_T is the difference between the transverse momentum vectors of the two exchanged particles [4]. The ratio R of the production cross-sections for $dP_T < 0.2$ GeV to $dP_T > 0.5$ GeV is significantly different for $q\bar{q}$ states and for the glueball candidates (see fig. 1.2). It has been observed that all undisputed $q\bar{q}$ states which can be produced by a double Pomeron exchange have very small values for this ratio (≤ 0.1). The states which cannot be produced by a double Pomeron exchange (with a negative G parity, for example) have slightly higher values ≈ 0.25. All non-$q\bar{q}$ candidates $f_0(980)$, $f_0(1500)$, $f_0(1710)$ and $f_2(1950)$ have values for this ratio about 1. The $a_0(980)$ and the $a_2(1320)$ studied in this thesis concern just the second group (with the $R \approx 0.25$). Their study has been made as a function of dP_T. The events related to the reaction 5.1 were divided into 3 groups depending on the dP_T value. For each group of events the efficiency as a function of the $\eta\pi^0$ mass has been calculated. Then the $\eta\pi^0$ mass spectrum corrected for efficiency has been plotted with the background events subtracted and then it has been parametrised by the function 5.5. The obtained values of the $a_0^0(980)$ and the $a_2^0(1320)$ productions for three dP_T intervals expressed as a percentage of their total contributions and the ratio R of events produced at $dP_T \leq 0.2$ GeV to the events produced at $dP_T \geq 0.5$ are listed in the table 5.1.

Resonance	$dP_T < 0.2$	$0.2 < dP_T < 0.5$	$dP_T > 0.5$	$R = \frac{\sigma(dP_T<0.2)}{\sigma(dP_T>0.5)}$
$a_0^0(980)$	25 ± 3 %	33 ± 5 %	42 ± 4 %	0.57 ± 0.09
$a_2^0(1320)$	10 ± 2 %	38 ± 2 %	52 ± 3 %	0.19 ± 0.04

Table 5.1: Production of the $a_0^0(980)$ and $a_2^0(1320)$ resonances for three dP_T intervals expressed as a percentage of their total contribution and the ratio R of events produced at $dP_T \leq 0.2$ GeV to the events produced at $dP_T \geq 0.5$

As it can be seen in the table 5.1 the production of the $a_2(1320)$ as a function of

dP_T shows the behaviour observed for other $q\bar{q}$ states that can not be produced by DPE. For the $a_0^0(980)$ resonance, R is approximately three times larger and this state can not be placed into any of the above mentioned groups. The possible reason of such a behaviour can be explained by a mixing of the $a_0^0(980)$ and $f_0(980)$ states (for the $f_0(980)$ $R = 0.88 \pm 0.12$) and this will be discussed in the chapter 8.6.

In addition, as it was mentioned in the introduction, an interesting effect has been observed in the azimuthal angle ϕ_{pp}, which is defined as the angle between the p_T vectors of the two outgoing protons. The measured distributions of ϕ_{pp} are clearly non-flat, as it was expected for a scalar Pomeron, and considerable variations are found between resonances with different J^{PC} [4]. The most detailed theoretical explanation of this effect was offered in [8], where the analytical expressions for ϕ_{pp} and t (the transverse momentum squared between the incoming and the outgoing proton) dependences for the production of resonances with different J^{PC} were obtained. The model was tested on experimental data and a good description was obtained [9].

In this work the ϕ_{pp} and t dependences for the $a_0^0(980)$ and $a_2^0(1320)$ resonances were studied. In order to determine the azimuthal angle ϕ for the resonances, the wole ϕ_{pp} area (from 0 to 180^o) was divided into six 30 degree bins. The events related to the reaction 5.1 were accordingly divided into 6 groups. For each group of events the above mentioned (for the dP_T measurement) analysis has been performed. The productions of resonances for the 6 ϕ_{pp} intervals were normalised to the total number of observed events. The resulting ϕ_{pp} dependences obtained for the $a_0^0(980)$ and the $a_2^0(1320)$ are shown in the figure 5.13 a) and b).

Resonance	b, GeV^{-2}
$a_0^0(980)$	6.2 ± 0.8
$a_2^0(1320)$	8.8 ± 0.4

Table 5.2: The slope parameters b, obtained by the parametrisation of the t dependences for the $a_0^0(980)$ and $a_2^0(1320)$ productions related to the reaction 5.1.

In order to determine the four momentum transfer squared (t) dependences of the resonances, the $\eta\pi^0$ mass spectrum has been fitted in 0.1 GeV^2 bins of t with the parameters of the resonances fixed to those obtained from the fits of the total data. The figure 5.13 c) and d) show the four momentum transfer squared from one of the proton vertices (see figure 7.1 in the chapter 7) for the $a_0^0(980)$ and $a_2^0(1320)$ respectively. The distributions have been fitted with exponential of the form $exp(-b|t|)$ and the obtained values of b are in the table 5.2.

In the chapter 7 the possible physical interpretation of the obtained ϕ_{pp} and t dependences for $a_0(980)$ and $a_2(1320)$ states will be discussed.

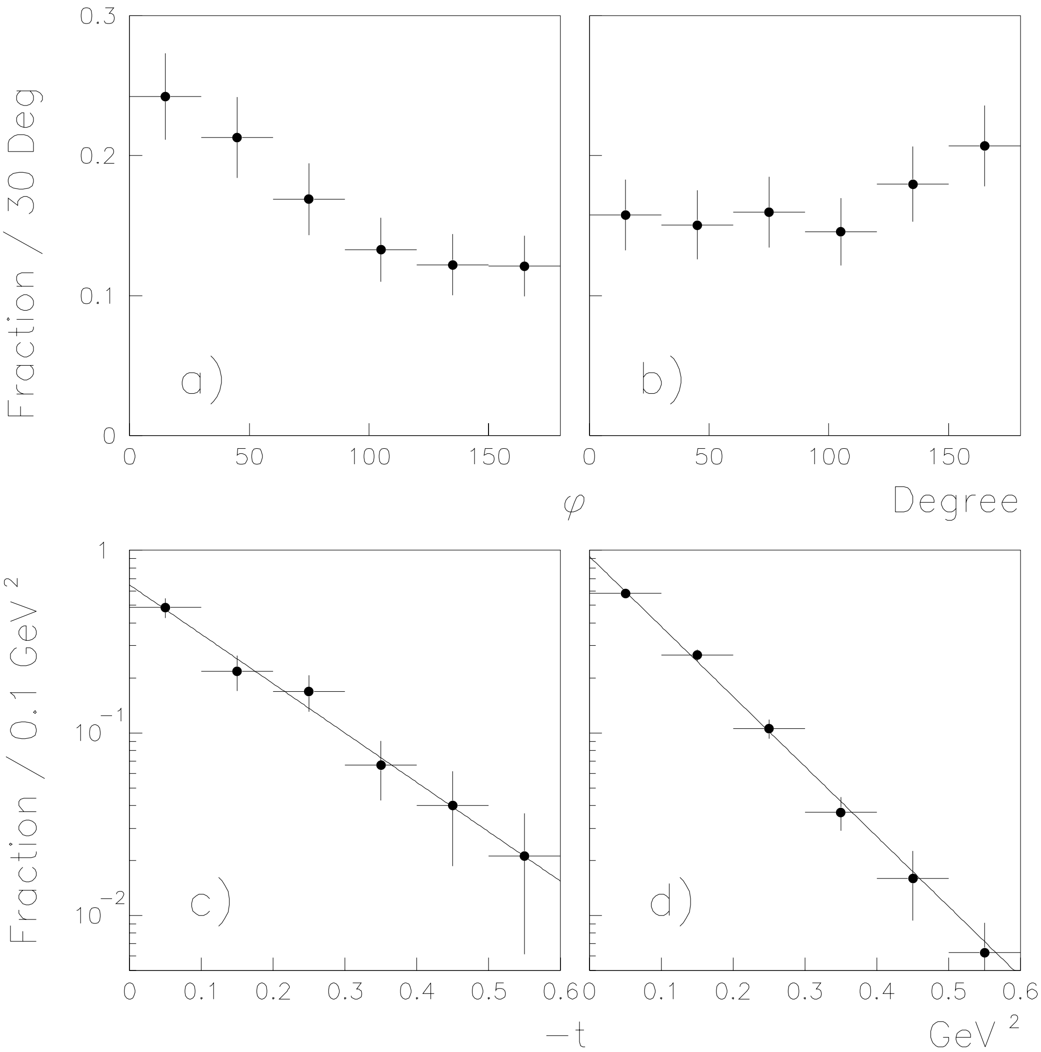

Figure 5.13: The azimuthal angle ϕ_{pp} between the transversal momentums of the fast and slow protons for a) the $a_0^0(980)$ and b) the $a_2^0(1320)$. The four momentum transfer squared t for c) the $a_0^0(980)$ and d) the $a_2^0(1320)$, with the fits with a form $e^{-b|t|}$.

Chapter 6

The analysis of the reaction $pp \to p_s(\eta\pi^-)\Delta^{++}(1232)$

This chapter describes the events selection procedure and the results of the partial-wave analysis of the central $\eta\pi^-$ production in the proton-proton collisions

$$pp \to p_s(\eta\pi^-)\Delta^{++}(1232) \tag{6.1}$$

with the subsequent decays of η to 2γs and $\Delta^{++}(1232)$ to $p_f\pi^+$. The dP_T, t and ϕ_{pp} dependences for the $a_0^-(980)$ and $a_0^-(1320)$ mesons are measured and described.

6.1 The selection of events

There are 2 γs from the η decay and 4 charged tracks with the 2 protons and 2 π mesons in the final state of the reaction 5.1. Therefore for the analysis we used events with 4 charged tracks and a number of gammas $\geq$2. The selection procedure is described below. Some stages of the selection are very close to those we used in the analysis of the reaction 5.1 in the previous chapter, and these will be discussed briefly. The selections which are specific to the reaction 6.1 will be discussed in more detail.

1. As well as for the reaction 5.1 the two nearby γs from one cluster ($R_{\gamma\gamma} < 60$ mm) which simultaneously have a small invariant mass ($m_{\gamma\gamma} < 60$ MeV) were merged to correct the results of the reconstruction program. However, it is

necessary to note that the merging of γs is much more essential for π^0 mesons than for η, because the γs from η predominantly lie in different clusters (due to its high mass) and this procedure is not so significant.

2. The electromagnetic showers from δ-electrons were removed from the analysis (see selection 5.2).

3. The total energy in all GAMS cells should be more than 3 GeV.

4. The reaction 6.1 differs from the reaction 5.1 by 2 charged π mesons from the decays of the central system and of the $\Delta^{++}(1232)$ baryon. The charged π meson interacting in the electromagnetic calorimeter causes hadron showers which can be reconstructed as γ. To reject such "false" γs from the further analysis the following procedure was applied: the charged track of the π meson has been extrapolated to the plane of the calorimeter giving the point of its interaction. The distance R from this point to the nearest cluster has been calculated. The figure 6.1 a) shows the distribution of R. In the figure 6.1 b) the distribution of the total energy in the clusters, where $R < 6$ cm, is shown. The peak in this distribution in the region < 1 GeV is characteristic for hadron clusters and corresponds to the minimum ionization energy of hadrons. Thus all clusters with $R < 6$ cm were rejected, cleaning the events from the hadron background in the calorimeter.

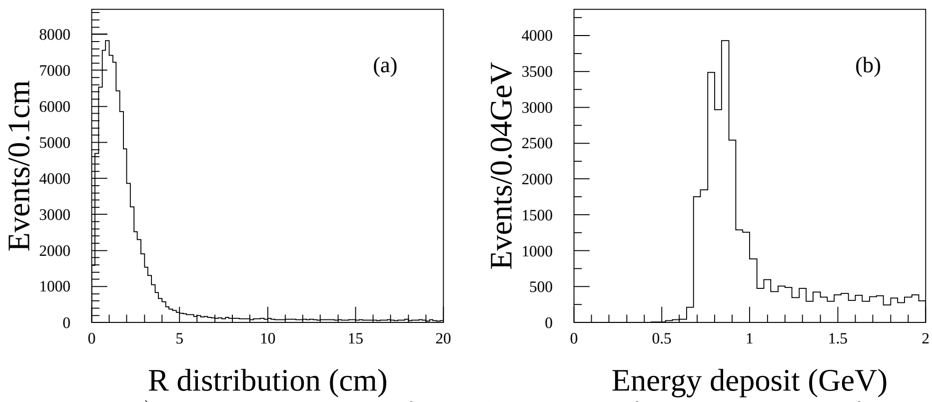

Figure 6.1: a) the distribution of the distance R from the point of interaction of the charged π meson with the GAMS calorimeter to the nearest cluster in the calorimeter; b) the distribution of the energy of such clusters for $R < 6$ cm.

5. As well as for the reaction 5.1 the balance of the beam proton momentum and the total momentum of particles in the final state implies that the selection 5.3 was required. This selection has been done more carefully at the phase of the kinematical fit when the constraints 4.3 were applied to calculate the most probable particle momentums for exactly equal initial and final moments in the reaction.

6. If the invariant mass of the pair of gammas was within the η mass window ([380,620] GeV), then this event was selected for the further analysis. As well as for the reaction 5.1 such a broad mass interval for η was used for background study. The invariant mass of 2 γs for events after the kinematical 4C-fit with the constraints 4.3 is shown in the figure 6.2 a). The events in the intervals of $\gamma\gamma$ mass [380,450] MeV and [650,720] MeV were used for the estimation of the background (see chapter 5, selection 5). The distributions of these events were subtracted from the distributions of the events from the interval [480,620] MeV to obtain background-free dependences.

7. To select events with a $\Delta^{++}(1232)$ baryon in the final state of the reaction the selection cut $M_{p_f\pi^+} < 1.4$ GeV was used. In the figure 6.2 b) the distribution of the $p_f\pi^+$ invariant mass is shown. The events, selected for the further analysis, are in the hatched area.

8. The main contribution to the background, lying below the peak of the $\Delta^{++}(1232)$ baryon, comes from the process $pp \to p_s(\eta\pi^+\pi^-)p_f$. In the figure 6.2 c) the distribution of the $\eta\pi^+\pi^-$ invariant mass is plotted. The selection $M_{\eta\pi^+\pi^-} > 1.5$ GeV suppresses efficiently the background below the $\Delta^{++}(1232)$ signal: the background decreases with a factor about 4. The distribution of the $p_f\pi^+$ invariant mass is shown for the events with $M_{\eta\pi^+\pi^-} > 1.5$ GeV in the figure 6.2 d) and of the background events with $M_{\eta\pi^+\pi^-} < 1.5$ GeV in the figure 6.2 e).

In total, 8027 events related to the reaction 6.1 were selected after the cuts 1-7. The figure 6.3 c) shows the $\eta\pi^-$ spectrum plotted for the selected events, corrected for the efficiency and normalised to the total number of selected events. The shaded histogram shows the distribution of the background events (left and right shaded areas

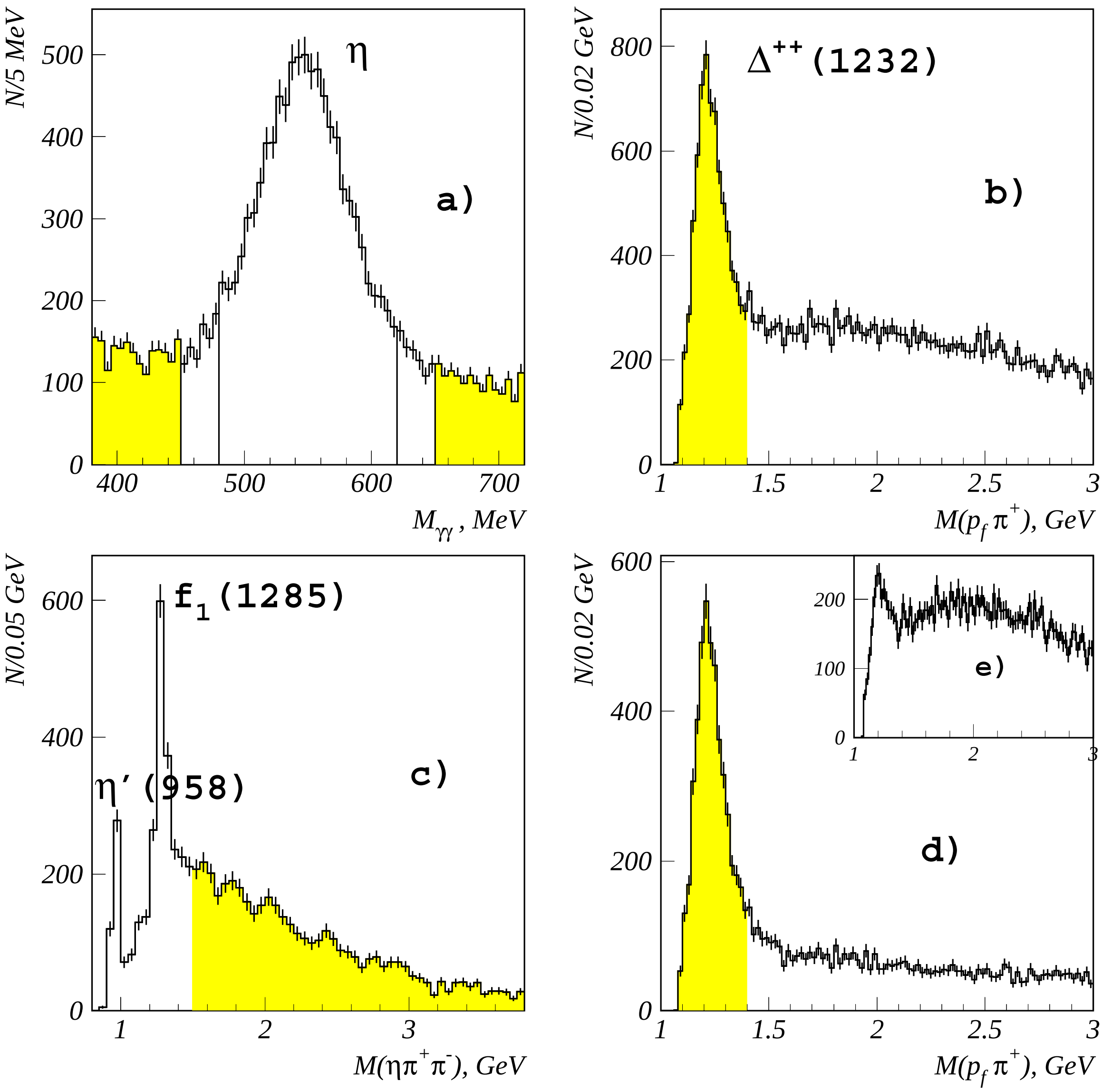

Figure 6.2: a) $\gamma\gamma$ spectrum for the reaction 6.1. The hatched bands show the events used as background in the analysis. b) $p_f\pi^+$ invariant mass before the selection $M_{\eta\pi^+\pi^-} > 1.5$ GeV. The events in the shaded area are considered as a $\Delta^{++}(1232)$ signal and used for the further analysis; c) $\eta\pi^+\pi^-$ invariant mass. The events in the shaded area were used for the further analysis. d) $p_f\pi^+$ invariant mass for the events with $M_{\eta\pi^+\pi^-} > 1.5$ GeV; e) $p_f\pi^+$ invariant mass for the events with $M_{\eta\pi^+\pi^-} < 1.5$ GeV;

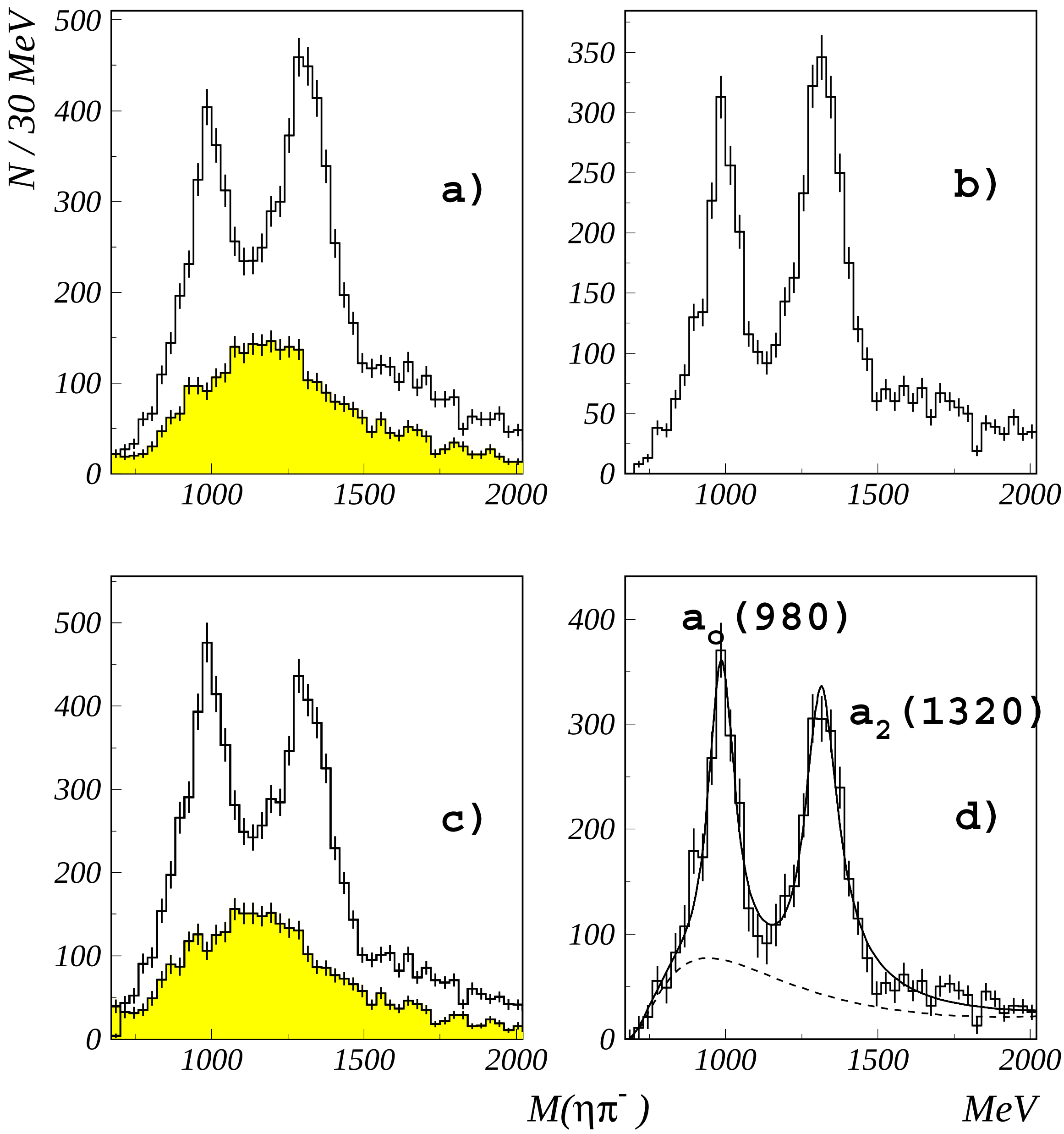

Figure 6.3: c) $\eta\pi^-$ mass spectrum corrected for the efficiency and normalised to the total number of events. Superimposed as a shaded histogram is an estimation of the background contribution; d) $\eta\pi^-$ spectrum with the subtracted background. The curve is the result of the fit by the function 5.7 (the dotted line represents a non-resonant contribution to the mass spectrum). In the figures a) and b) the same distributions, as in c) and d), are shown, but non-corrected for the efficiency.

in the figure 6.2 a)). The background affects approximately 38% of the total number of events, therefore a special attention was brought to the study of the background events, as well as to the events related to the reaction 5.1. In the figure 6.3 d) the $\eta\pi^-$ spectrum corrected for the efficiency and normalised to the total number of selected events is shown with the subtracted background. In the figures 6.3 a) and b) the same distributions as in the c) and d) are plotted, but they are not corrected for the efficiency. The efficiency for the events related to the reaction 6.1, as the function of mass, is proportional to the coefficient $c_{00}(m)$ presented in the figure 4.1.

There is a clear evidence for the $a_0^-(980)$ and $a_2^-(1320)$ resonances in the $\eta\pi^-$ mass spectrum. But the ratio of the $a_0(980)$ to the $a_2(1320)$ productions in the reaction 6.1 differ from those obtained in the reaction 5.1: the $a_0^-(980)$ and $a_2^-(1320)$ resonances are produced with identical intensities, in the reaction 5.1 the $a_0^0(980)$ production is about 2 times the $a_2^0(1320)$ production. In the chapter 7 the possible reasons for these features of the $\eta\pi^0$ and $\eta\pi^-$ spectra will be considered.

To determine the parameters of these resonances a fit to the efficiency-corrected mass spectrum 6.3 d) was performed by adding two relativistic Breit-Wigner's functions and a curve describing the background. The experimental resolution was taken into account in the fitting procedure (see equations 5.5 -5.9). The fit is shown in the figure 6.3 d) and gives the following parameters for the $a_0^0(980)$ and $a_2^0(1320)$ resonances:

$$\begin{aligned} M(a_0^-(980)) &= 988 \pm 8\text{MeV}, \quad \Gamma(a_0^-(980)) = 61 \pm 19\text{MeV}, \\ M(a_2^-(1320)) &= 1316 \pm 9\text{MeV}, \quad \Gamma(a_2^-(1320)) = 112 \pm 14\text{MeV}. \end{aligned} \tag{6.2}$$

These parameters of the resonances are consistent with those from the PDG [20] and with the parameters of the $a_0^0(980)$ and $a_2^0(1320)$ obtained in the previous chapter (equations 5.10). The fit of the $\eta\pi^0$ mass spectrum gives the following value for the production ratio of the $a_0^-(980)$ and $a_2^-(1320)$ (to be compared with 5.11:

$$\frac{\sigma(pp \to p[a_0^-(980) \to \eta\pi^-]\Delta^{++}(1232))}{\sigma(pp \to p[a_2^-(1320) \to \eta\pi^-]\Delta^{++}(1232))} = 0.8 \pm 0.2 \tag{6.3}$$

6.2 The partial-wave analysis

A PWA of the $\eta\pi^-$ events was performed in the same mass interval ([670,2050] MeV) and in bins with the same size (60 MeV), as the PWA of the $\eta\pi^0$ events. This gives the possibility to compare the results of the analysis for both reactions. As well as in the case of the reaction 5.1, a model of S, P and D waves was used and the analysis was made in terms of angular momentums as amplitudes and relative phases of partial waves with the subtraction of background events, as it was discussed in the chapter 5.2.

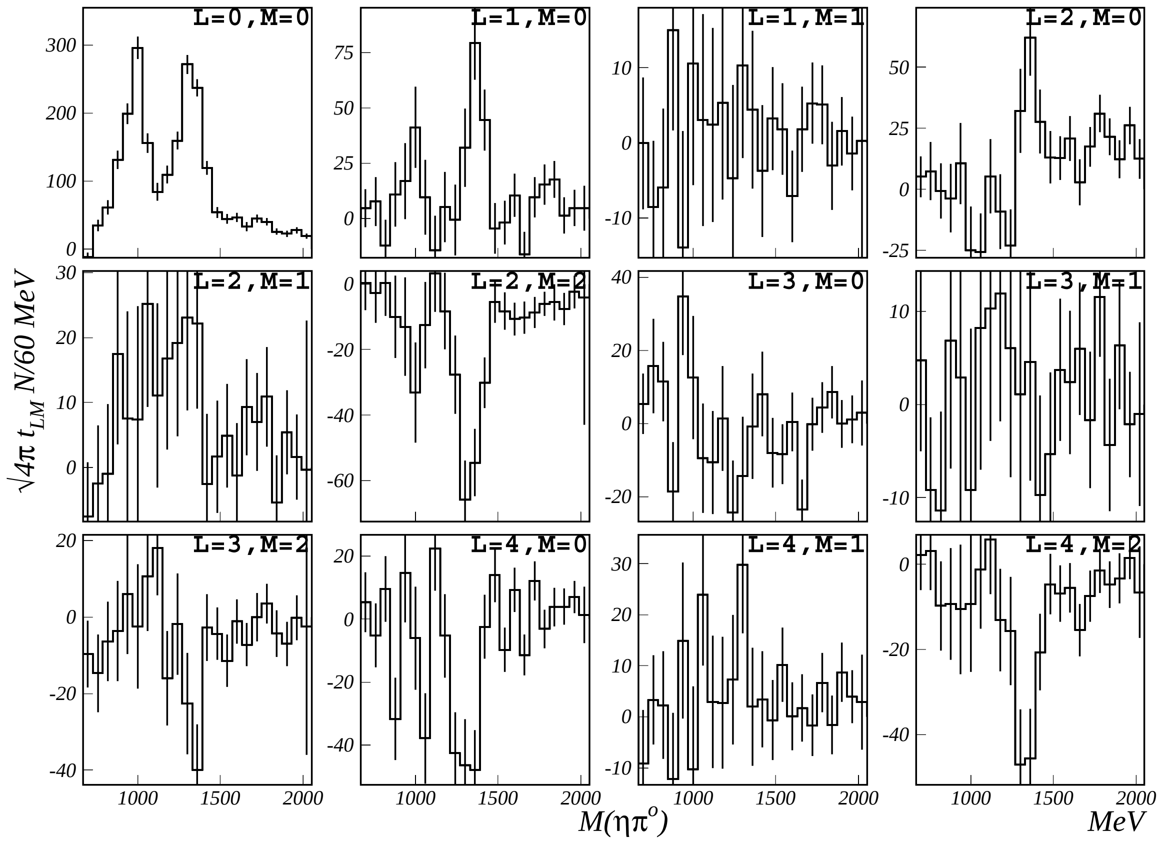

Figure 6.4: Angular momentums t^{sig}_{LM} for $\eta\pi^-$ events, the background is subtracted.

It is interesting to note that though efficiencies for reactions 5.1 and 6.1 are different (see the spherical harmonics coefficients of the efficiency in the figure 4.1), the results of the PWA for both reactions are very similar. The difference in angular momentums (see figures 5.10 for the reaction 5.1 and 6.4 for the reaction 6.1) is explained by the different relative intensity of the $a_0(980)$ and $a_2(1320)$ productions in these reactions.

The ambiguity of solutions in the PWA, performed in terms of amplitudes and phases, also has the same nature and dependence of the $\eta\pi$ mass as for the reaction 5.1. So the "bootstrapping" procedure described in the previous chapter for the $\eta\pi^0$

system was applied. That is, in the $\eta\pi^-$ mass region below 1.2 GeV, strongly suffering from ambiguities, the physical solutions were picked up from amplitudes squared of the S wave according to the Breit-Wigner curve describing the $a_0(980)$ peak in the $\eta\pi^-$ mass spectrum. In the region above 1.2 GeV, where the solutions are not affected by ambiguities and all solutions are identical within errors, the physical solution was calculated according to the formulas 5.12 and 5.13. In the figure 6.5 the physical solution from the PWA of the $\eta\pi^-$ events is shown.

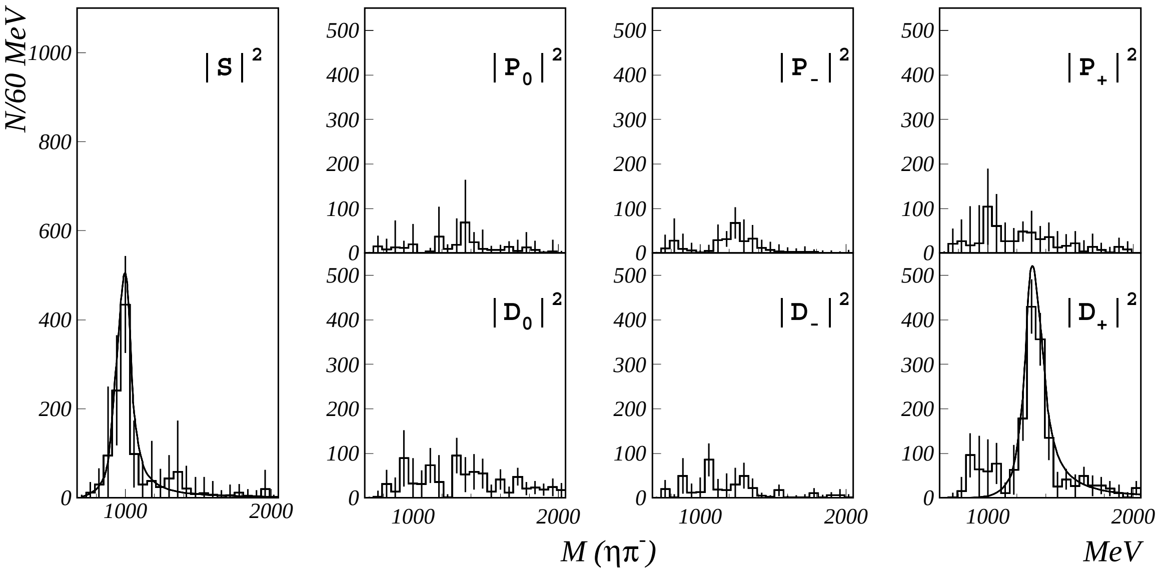

Figure 6.5: The physical solution of the PWA of the $\eta\pi^-$ events. Curves on the histograms $|S|^2$ and $|D_+|^2$ are Breit-Wigner's fit of the peaks of the $a_0^-(980)$ and $a_2^-(1320)$ resonances.

As it can be seen in the figure 6.5 the S and D_+ waves dominate in the mass regions below and above 1.2 GeV respectively. The contribution of the remaining waves, including the exotic P wave, is statistically insignificant. Again there is no evidence for the $a_0^0(1450)$ nor the $a_2^0(1660)$ and no evidence for other significant structures in any other waves. It means that the results are very similar to those obtained for the $\eta\pi^0$ system. A fit of the S and D_+ amplitudes squared with a Breit-Wigner function gives parameters for the $a_0^0(980)$ and the $a_2^0(1320)$ similar to those got with fit of the efficiency-corrected mass spectrum 6.3 d).

6.3 Study of the dP_T, t and ϕ_{pp} dependences

The relative cross-sections were obtained for the $a_0^-(980)$ and $a_2^-(1320)$ resonances in the reaction 6.1 in three dP_T intervals: $dP_T < 0.2$GeV, $0.2 < dP_T < 0.5$GeV and $dP_T > 0.5$GeV. The applied method is similar to that used for the reaction 5.1 and described in the chapter 5.3. The obtained results are presented in the table 6.1:

Resonance	$dP_T < 0.2$	$0.2 < dP_T < 0.5$	$dP_T > 0.5$	$R = \frac{\sigma(dP_T<0.2)}{\sigma(dP_T>0.5)}$
$a_0^-(980)$	14 ± 3 %	37 ± 2 %	49 ± 2 %	0.29 ± 0.09
$a_2^-(1320)$	9 ± 3 %	39 ± 2 %	52 ± 2 %	0.17 ± 0.06

Table 6.1: Production of the $a_0^-(980)$ and $a_2^-(1320)$ resonances for three dP_T intervals expressed as a percentage of their total contribution and the ratio R of events produced at $dP_T \leq 0.2$ GeV to the events produced at $dP_T \geq 0.5$

The values R for the $a_2^0(1320)$ and $a_2^-(1320)$ production are practically identical (compare tables 5.1 and 6.1) and consistent with the characteristic values of R for the states which cannot be produced in a double Pomeron exchange. For the $a_0^0(980)$ and $a_0^-(980)$ resonances the values of R are very different. If $a_0^-(980)$ also belongs to the group of states which cannot be produced in a double Pomeron exchange, the $a_0^0(980)$, as it was already said in the chapter 5.3, does not belong to the groups described in the introduction in the section dedicated to the glueball filter. The possible reasons for this difference in the $a_0^0(980)$ and $a_0^-(980)$ productions are discussed in the next chapter.

As well as for the reaction 5.1, the ϕ_{pp} and t dependences were obtained for the $a_0^-(980)$ and $a_2^-(1320)$ states. But if in the reaction 5.1 the four momentum transfers t for slow and fast vertices are not differentiated, because they are indistinguishable in the center-of-mass frame, in the case of the reaction 6.1 it is necessary and possible to distinguish t_f and t_s As it can be seen in the figure 7.1, in the reaction 6.1 the exchanged particle in the "fast" vertex can be the negative Reggeon only, while in the "slow" vertex it can be as Pomeron as Reggeon, as well as in both vertices of the reaction 5.1. The distribution of the ϕ_{pp}, t_f and t_s for the $a_0^-(980)$ and the $a_2^-(1320)$ are given in the figure 6.6. The t-dependences were parametrised by a function $e^{-b|t|}$, giving the slope parameter b listed in the table 6.2.

Resonances	b_f, GeV^{-2}	b_s, GeV^{-2}
$a_0^-(980)$	4.0 ± 0.3	7.5 ± 0.4
$a_2^-(1320)$	5.9 ± 0.5	7.9 ± 0.6

Table 6.2: Slope parameters b, obtained by the parametrisation of the t dependences for the $a_0^-(980)$ and the $a_2^-(1320)$ productions in the reaction 6.1. The indices f and s mean fast and slow vertices in the laboratory frame (see figure 7.1).

Comparing the figures 5.13 and 6.6, it is easy to see that the ϕ_{pp} dependences for the $a_2^0(1320)$ and for the $a_2^-(1320)$ are similar, but for the $a_0^0(980)$ and for the $a_0^-(980)$ they are different. A physical interpretation of this observation will be suggested in the discussion (next chapter).

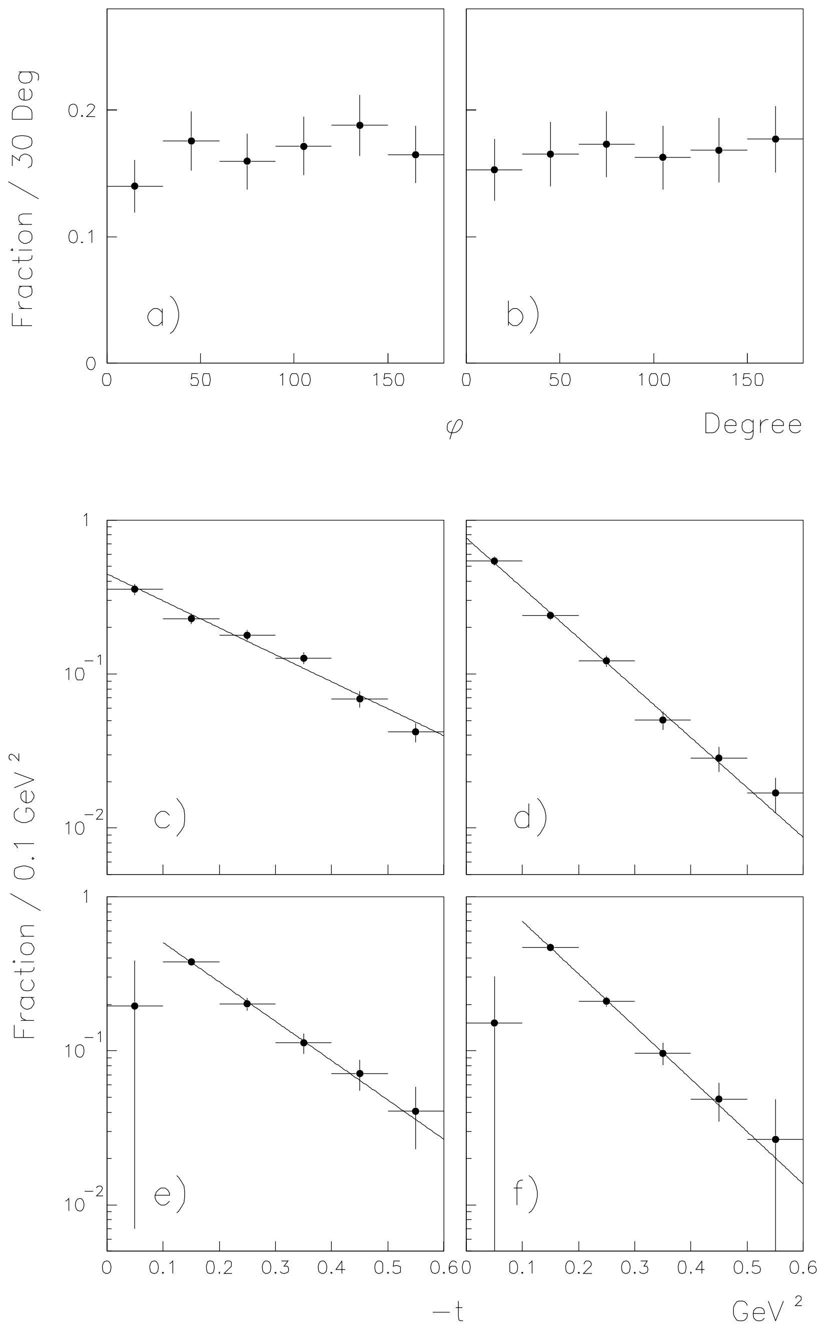

Figure 6.6: The azimuthal angle ϕ_{pp} between the transversal momentums of the fast and slow protons for a) the $a_0^-(980)$ and b) the $a_2^-(1320)$. The four momentum transfer squared t_f for c) the $a_0^-(980)$ and d) the $a_2^-(1320)$ and t_s for e) the $a_0^-(980)$ and f) the $a_2^-(1320)$, with fits of the form $e^{-b|t|}$. The indices f and s mean fast and slow vertices in the laboratory frame (see figure 7.1).

Chapter 7

Discussion

The partial-wave analysis of the reactions 5.1 and 6.1 performed in the $\eta\pi$ mass interval from 670 to 2000 MeV has shown that the main contribution to the $\eta\pi^0$ and $\eta\pi^-$ productions in the central proton-proton collisions in this mass region is formed by the S and D_+ waves, where the $a_0(980)$ and the $a_2(1320)$ resonances have been observed, respectively. The contributions of the remaining waves are negligible. The states $a_0(1450)$, $a_2(1660)$, $\hat{\rho}(1405)$ which were observed by some experimental groups (see chapter 2) are not seen in this analysis.

The interest is caused by the absence of any P wave, which has the exotic quantum numbers $J^{PC} = 1^{-+}$. While the resonances $a_0(1450)$ and $a_2(1660)$ were observed by only one experimental group (Crystal Barrel, CERN) and its existence requires experimental confirmation (in the charge exchange reactions 2.1 and in the diffraction 2.4 these particles were not observed), the exotic P-wave was observed with a good confidence level by all experimental groups which studied the $\eta\pi$ system both in neutral and charged modes (see table 2.1). The debate is conducted only on the resonant or non-resonant nature of this wave in the mass region about 1.4 GeV.

However, it is possible to explain the absence of the 1^{-+} wave in central pp collisions simply if one takes into account the dependences of two-particle exchange intensities on the centre of mass energy, see equations 1.2. Since a double Pomeron exchange is impossible in $\eta\pi$ production[1] ($I \neq 0$), the Reggeon-Pomeron exchange

[1]Except for the $a_0(980)$ whose production in double Pomeron exchange can take place due to a mixing with the $f_0(980)$ via a $K\bar{K}$ intermediate state.

gives the main contribution to the cross-section. From equations 1.2 it follows that the ratio between Reggeon-Pomeron and Reggeon-Reggeon exchanges is proportional to $\sqrt{s}$, that is $\sigma(RP)/\sigma(RR) \sim 29$ at energy 450 GeV. Let's consider the possible quantum numbers J^{PC} of the Reggeon R which forms the exotic state X with the quantum numbers $J^{PC} = 1^{-+}$ by interacting with the Pomeron P ($J^{PC} = 0^{++}$). Using P and C parity conservation in strong interactions [93]: $\mathrm{P}_X = (-1)^L \mathrm{P}_P \mathrm{P}_R$, $\mathrm{C}_X = (-1)^L \mathrm{C}_P \mathrm{C}_R$ one can conclude that an exchange of Reggeon should have quantum numbers: $0^{+-}, 1^{-+}, 2^{+-}...$. The particles with such quantum numbers are exotic and the probability of an exotic exchange is small, as it can be seen from the results of this analysis. In a Reggeon-Reggeon exchange 1^{-+} states can be produced, for example, in the $\eta\pi$, $b_1\pi$, $f_1\pi$ systems, but a Reggeon-Reggeon exchange is small compared with a Reggeon-Pomeron one. Thus, this suggests that the equations 1.2 are valid, that the probability of an exotic Reggeon exchange is small, and by taking into account P and C parity conservation in strong couplings, we can explain the absence of an exotic P wave in the $\eta\pi$ system in central pp collisions.

Another interesting effect observed in the analysis of the $\eta\pi$ system in pp central collisions has attracted the attention of the theorists [102]. It was found that the relative cross-sections of the $a_0(980)$ and the $a_2(1320)$ productions in reactions 5.1 and 6.1 are essentially different. Let's remind the results of the chapters 5.1 and 6.1:

$$\frac{\sigma(pp \to pp[a_0^0(980) \to \eta\pi^0])}{\sigma(pp \to pp[a_2^0(1320) \to \eta\pi^0])} = 2.0 \pm 0.3, \tag{7.1}$$

$$\frac{\sigma(pp \to p[a_0^-(980) \to \eta\pi^-]\Delta^{++}(1232))}{\sigma(pp \to p[a_2^-(1320) \to \eta\pi^-]\Delta^{++}(1232))} = 0.8 \pm 0.2 \tag{7.2}$$

In [102] the authors try to explain this difference by the effect of an $a_0^0(980) - f_0(980)$ mixing. In the figure 7.1 the diagrams of the $a_0(980)$ and $a_2(1320)$ resonance production in reactions 5.1 (a) and 6.1 (b) are shown. The essential difference of these diagrams consists in the nature of an intermediate state in the upper (”fast”) vertex: in the case a) it can be both Reggeon and Pomeron; in the case b) – negative Reggeon only. Thus, in the reaction 7.1 b) the Pomeron-Pomeron exchange is impossible. As it was already said, the $\eta\pi^0$ production in a Pomeron-Pomeron exchange is also prohibited by an isospin symmetry. However, in a Pomeron-Pomeron exchange the $f_0(980)$ resonance may be produced, intensively decaying into $\pi^+\pi^-$,

$\pi^0\pi^0$ or $K\bar{K}$ modes. The cross-section of the $f_0(980)$ production is approximately 100 times higher than the cross-section of the $a_0^0(980)$. The mixing of the $a_0^0(980)$ and $f_0(980)$ resonances: $f_0(980) \to K\bar{K} \to a_0^0(980)$, can cause a high $a_0^0(980)$ production compared with $a_0^-(980)$.

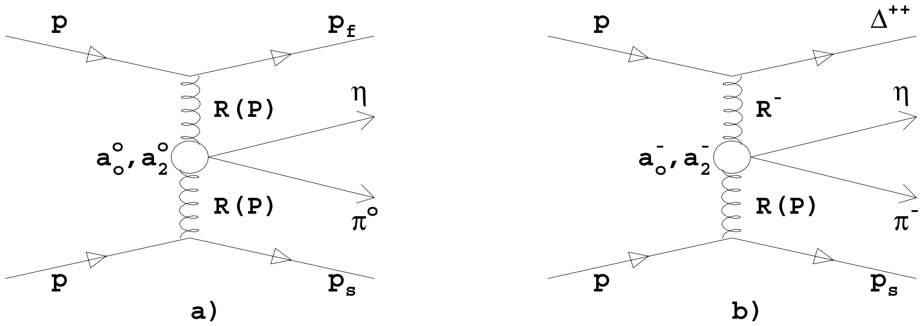

Figure 7.1: The diagrams of $a_0(980)$ and $a_2(1320)$ production in the reactions 5.1 a) and 6.1 b).

The intensity of the $a_0^0(980) - f_0(980)$ mixing can be estimated using the ϕ_{pp} dependence for the $a_0^0(980)$. In the figures 5.13 a), b) and 6.6 a), b) one can see the ϕ_{pp} dependences for the $a_0^0(980)$, $a_2^0(1320)$, $a_0^-(980)$ and $a_2^-(1320)$, respectively. We see that all of them are flat except for the distribution for the $a_0^0(980)$. It has a shape which is very close to ϕ_{pp} for the $f_0(980)$ (see figure 7.2 b)). If the $a_0^0(980)$ forms in a Reggeon-Pomeron exchange only it would have a flat distribution of ϕ_{pp}, as well as the $a_0^-(980)$ which can be produced by $a_0\mathrm{P} \to a_0$. The contribution of a Reggeon-Reggeon exchange $\pi b_1 \to a_0$ in the $a_0^-(980)$ production in reaction 7.1 b) is not eliminated, and it also has a flat ϕ_{pp} distribution [102]. To estimate a contribution of the $a_0^0(980)$ produced by an $a_0^0(980) - f_0(980)$ mixing the parametrization of the ϕ_{pp} dependence for the $a_0^0(980)$, a non-coherent sum of two functions was made: a constant describing the $a_0^0(980)$ production in a Reggeon-Pomeron exchange and a function $(4 + \cos\phi_{pp})^2$ which describes the ϕ_{pp} dependence for the $f_0(980)$. In the figure 7.2 a) the result of the parametrization is presented. It was found that 80±25% of the $a_0^0(980)$ comes from an $a_0^0(980) - f_0(980)$ mixing. Combining this result with the relative total cross sections for the $a_0^0(980)$ and the $f_0(980)$ production, the mixing intensity is found in [102] to be 8±3% . This value, based on the results of this thesis, closely agrees with the theoretical predictions for an $a_0^0(980) - f_0(980)$ mixing obtained in [103].

The abnormally large ratio R for the $a_0^0(980)$ production at small and large dP_T can also be explained by the large fraction of the $a_0^0(980)$ produced from $f_0(980)$ by $K\bar{K}$ mixing. As it was found in the chapter 6.3, this ratio for $a_0^-(980)$ is equal to 0.29 ± 0.09 which closely matches double Pomeron exchange produced particles. At the same time for the $a_0^0(980)$ R=0.57 ± 0.09 (see chapter 5.3). However, if we take into account that for the $f_0(980)$, R is equal to 0.88 ± 0.12 [3] and that 80±25% of the $a_0^0(980)$ should have the same value of R, it is possible to estimate R for a remaining part of events which are not produced by an $a_0^0(980) - f_0(980)$ mixing. For these events R=0.18 ± 0.07, which matched R for the resonances whose production in DPE is forbidden.

In the next chapter the possibility of studying the central pp collisions will be considered for the future experiment CMS(CERN) at energy of the LHC $7 + 7$ TeV. At such energies the double Pomeron exchange will dominate completely. In this case the $a_0^0(980)$ can be formed by an $a_0^0(980) - f_0(980)$ mixing only at a level 8±3% coming from the $f_0(980)$ production.

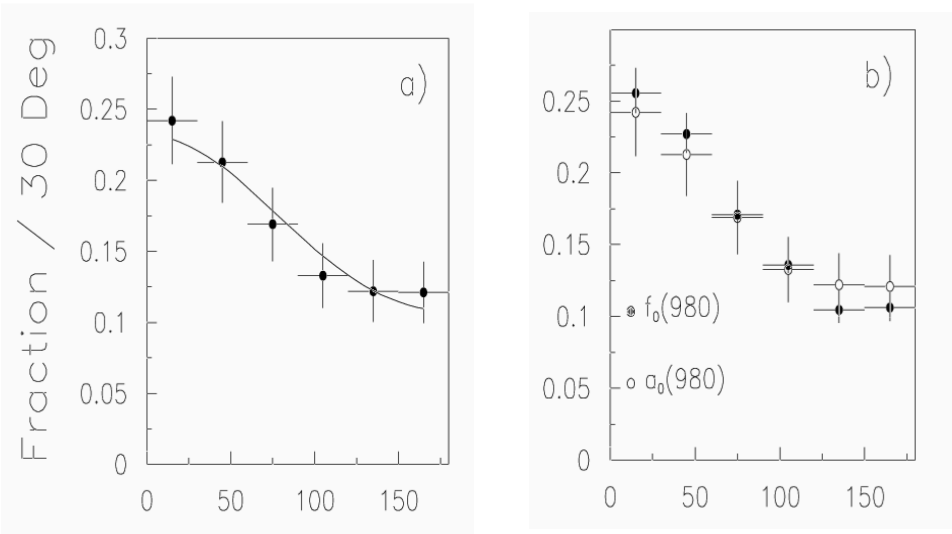

Figure 7.2: a) A parametrization of the angle ϕ_{pp} for the $a_0^0(980)$; b) ϕ_{pp} for the $a_0^0(980)$ and the $f_0(980)$. Figures from [102].

Chapter 8

Perspectives of central production study at LHC energy with CMS

The recent developments in the study of the hadronic interactions show that the central production is a mechanism which can be used to a great advantage in the study of the hadronic spectra. New effects observed in the *pp* collisions were discussed in detail in the introduction. It would be of a great interest to extend these studies to higher energies, where it should be much easier to disentangle the production mechanism.

These studies have been performed in a fixed target experiment at $\sqrt{s}$ <30 GeV. The theoretical calculations of the evolution of the different exchange mechanisms with the centre of mass energy (see equations 1.2) predict that a double Pomeron exchange will be more significant at high energies, whereas the Reggeon-Reggeon and Reggeon-Pomeron mechanisms will be of decreasing importance. From 1.2 at LHC energy, where $\sqrt{s}$ =14 TeV, we can expect a pure double Pomeron exchange and no contamination from Reggeon exchange. It gives a feeling of great achievement to study the nature of the Pomeron, to solve the "glueball puzzle" and to understand the underlying dynamics of the reaction.

In this chapter we try to substantiate the scopes for the study of the central production reactions at the LHC energy in the CMS experiment. As CMS alone cannot trigger on central production (that requires the measurement of the protons scattered with small angles) to study this physics the TOTEM detector integrated in CMS is needed.

8.1 The CMS detectors

The CMS detector has been designed to exploit the physics of proton-proton collisions at a centre-of-mass energy of 14 TeV over the full range of luminosities expected at the LHC. To reach this objective it will identify and precisely measure muons, electrons and photons over a large energy range; by determining the signatures of quarks and gluons through the measurement of jets of charged and neutral particles (hadrons) with a moderate precision; and by measuring the missing transverse energy flow, which will enable the signatures of noninteracting new particles as well as neutrinos to be identified.

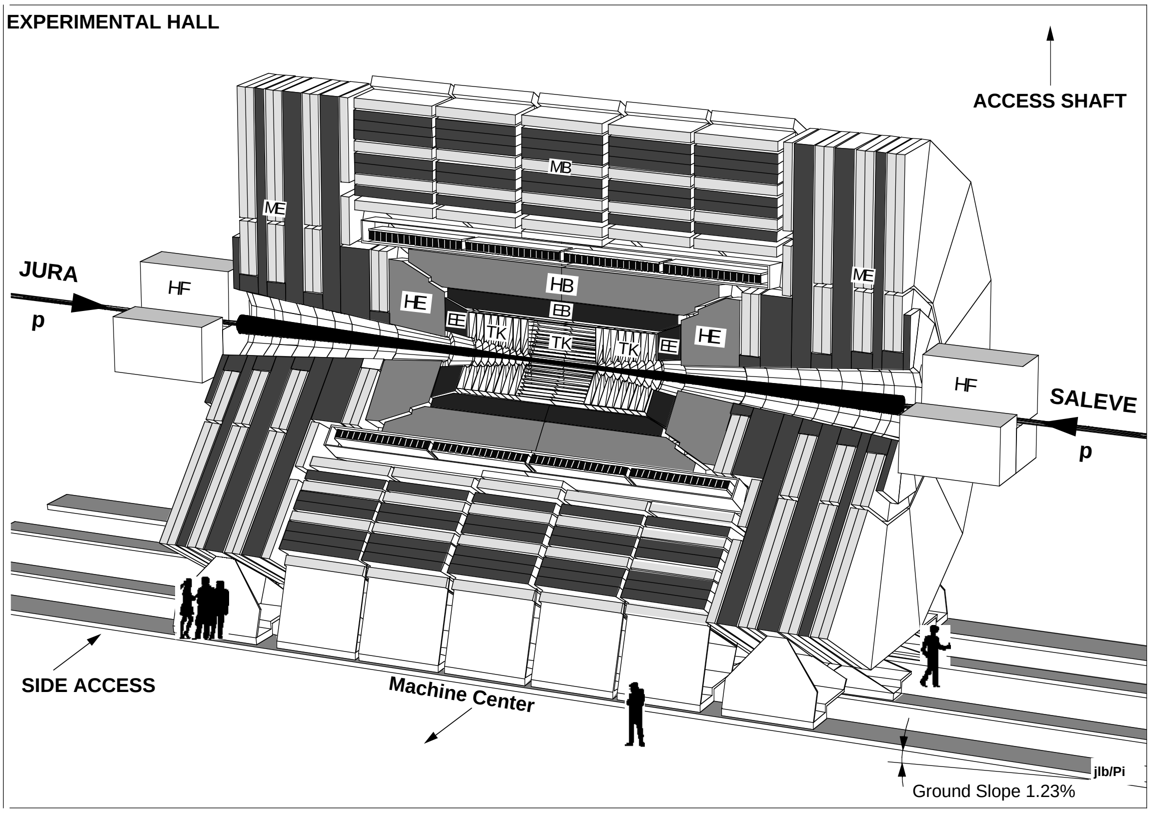

Figure 8.1: Overall view of the CMS detector.

The CMS detector is shown in the figure 8.1. It consists of a 4 Tesla, 13.0 m long Solenoidal Superconducting Magnet with an inner diameter of 5.9m. It is surrounded by 5 "wheels" (cylindrical structures) (MB) and 2 endcaps (disks) (ME) of muon absorber and muon tracking chambers, giving a total length of 21.6m and an outer diameter of 14.6m (the return yoke is indicated in the figure 8.1 by dark grey shaded areas, where muon chambers are indicated by light dotted areas). This system forms the "Compact Muon Solenoid" which gives to the detector its name. The Solenoid Magnet and everything located inside its cryostat are supported by the central wheel. Inside the magnet cryostat are placed three sets of charged particle tracking devices (TK) and a calorimeter divided in two parts, each one closing at best the solid angle and measuring the energy of different particles. This set forms an electromagnetic (EE,EB) and hadron calorimeter (HE,HB). A forward hadron calorimeter (HF) completes the pseudorapidity coverage up to a value of $|\eta| = 5$ ($\theta \approx 0.8^o$). For our purposes, i.e. for the study of the central production reaction 1.1, the assemblage of the precise tracking system and electromagnetic calorimeter allows the measurement of neutral as well as of charged decay modes of the central particle.

The CMS detectors are described in detail in the CMS Technical Proposal [104]. In this section a brief description of the detectors, which are important for a central production measurement, is only given.

Tracking

The central tracking will play a major role in all physics searches. The goal of the tracking system is to provide precision momentum measurements and ensure efficient pattern recognition at high LHC luminosities over the rapidity range $|\eta| < 2.5$. The CMS tracker is completely made of silicon detectors, which are the best choice for tracking purposes in the LHC environment. In the present and past experiments, large-volume gas detectors were an alternative to silicon ones, but they have a slower response time, so that the LHC timing requirements (with a bunch crossing events 25 ns) do not allow their usage.

The tracker consists of a central (barrel) part with three pixel and ten strip layers and the disk and endcap sections with two pixel layers and twelve strip layers [105]. A cross-section of one quadrant is shown in the figure 8.2. The pixel layers in the barrel and endcap parts are placed in the region with $r < 200$ mm and $z < 500$ mm, the strip layers are outside of this region. The strip part of the tracker consists of single-sided and double-sided detector modules. The double-sided detector modules are made of two single-sided detectors mounted back to back with a strip inclination of 5.7^o

with respect to each other. Thus, these ”stereo” modules deliver two-dimensional hit positions.

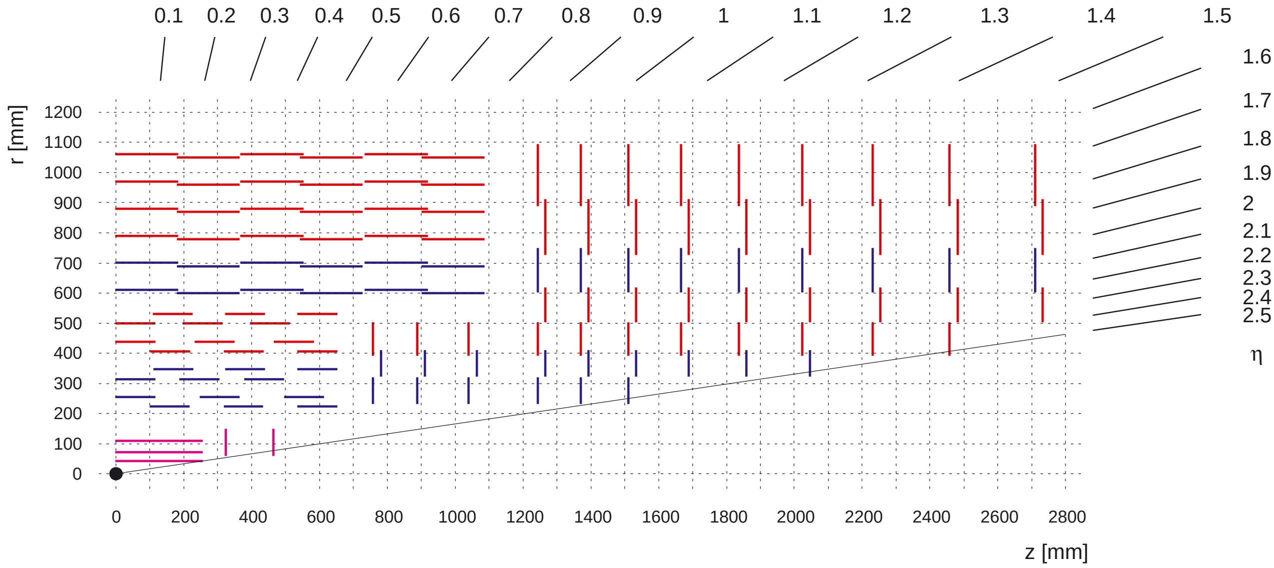

Figure 8.2: Schematic of the inner tracker.

The main performances of the CMS tracker are listed below [106]:

- high p_T isolated tracks are reconstructed with a transverse momentum resolution of better than $\delta p_T/p_T \approx (15p_T \oplus 0.5)\%$, with p_T in TeV, in the central region ($|\eta| \leq 1.6$), gradually degrading to $\delta p_T/p_T \approx (60p_T \oplus 0.5)\%$ as η approaches 2.5;

- in combination with the outer muon chamber system the muon momentum resolution above 100 GeV can be parametrised as $\delta p/p \approx (4.5\sqrt{p})\%$ (p in TeV) for rapidity extending up to η=2;

- charged hadrons with p_T above 10 GeV are reconstructed with an efficiency approaching 95% and even for hadrons with p_T as low as 1 GeV with an efficiency better than 85%;

- the reconstruction efficiency for muons is better than 98% over the full η range for values of p_T as low as 1 GeV;

- high energy electrons are reconstructed with an efficiency above 90%.

One of the important features of the tracking system is the quantity of tracker material, because it affects the propagation of gammas through the tracker volume. A lot of tracker material can cause the conversion of gammas to e^+e^- pairs. The figure 8.3 shows the quantity of tracker material in radiation length units as a function of the pseudorapidity. This data is used in Monte-Carlo simulations of double exchange processes.

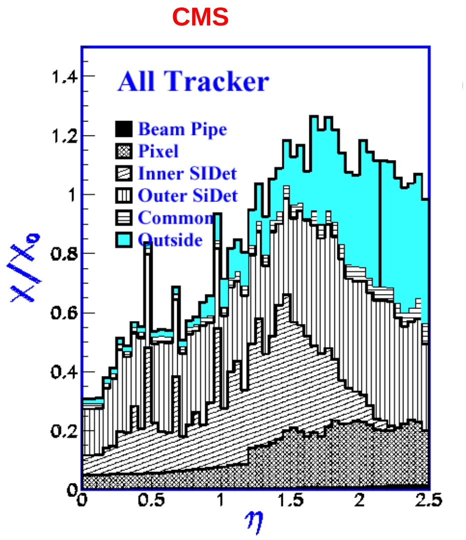

Figure 8.3: Tracker material in radiation length units as a function of η.

Calorimetry

The CMS calorimeters will play a significant role in exploiting the physics potential offered by the LHC. Their main functions are to identify and measure precisely the energy of photons and electrons, to measure the energy of jets, and to provide a hermetic coverage for measuring the missing transverse energy. In addition, a good efficiency for electron and photon identification as well as excellent background rejection in hadrons and jets are required. In CMS both, electromagnetic and hadron, calorimeters are used. The combined response of the electromagnetic and hadron calorimeters provides the raw data for the reconstruction of particle jets and the missing transverse energy. A schematic view of the calorimetry system is shown in the fig.8.4.

The CMS electromagnetic calorimeter consists [107] of about 100,000 crystals of PBWO4 (see fig.8.5), each with a truncated pyramidal shape (the front and back faces (small and large base of the pyramid frustum) are parallel; the faces are approximately 2cm×2cm, the total length is about 23 cm, corresponding to 25.8 radiation lengths).

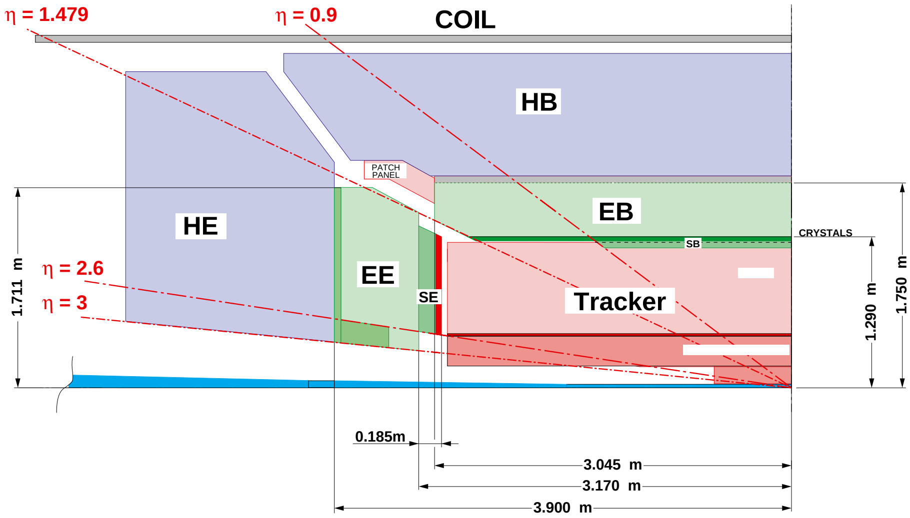

Figure 8.4: Longitudinal schematic view of one quadrant of the calorimetry system (the forward hadron calorimeter (HF in the figure 8.1) is missing in this figure).

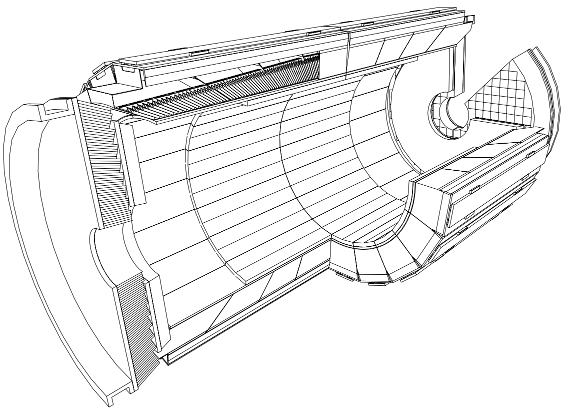

Figure 8.5: 3D-view of ECAL.

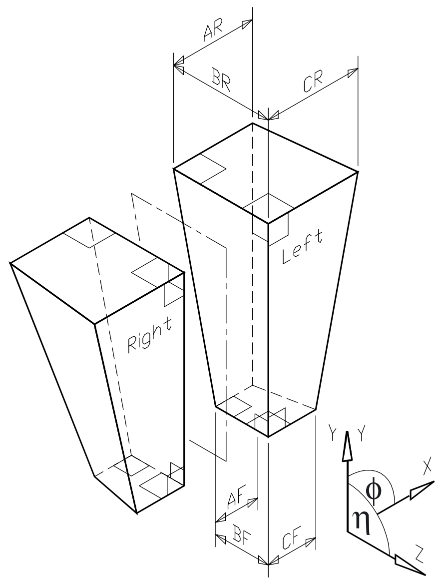

Figure 8.6: Principle of the flat-pack configuration.

The crystals are grouped by pair in phi and by five in eta in the so-called flat-pack configuration (see the figure 8.6). This group of 10 crystals contained in an alveolar structure forms what is called a submodule. To produce a non-pointing geometry in eta, and thus improve the measurement of missing energy, the crystal longitudinal axes are all inclined by 3 degrees with respect to the line joining the crystal front face centre to the interaction point.

The choice of the $PbWO_4$ crystals for the electromagnetic calorimeter was based on the following considerations: $PbWO_4$ has a short radiation length (0.89 cm) and a small Molière radius (2.19 cm); it is a fast scintillator; it is relatively easy to produce from readily available raw materials. The geometrical crystal coverage extends to $|\eta|$=3. Precision energy measurement, involving photons and electrons, will be carried out to $|\eta|$ <2.6. This limit has been determined by considerations of the radiation dose and the amount of pile–up energy, it matches the geometric acceptance of the inner tracking system.

ECAL Detector	Barrel (EB)	Endcap (EE)
Pseudorapidity range	$0 \leq \|\eta\| \leq 1.48$	$1.48 \leq \|\eta\| \leq 3.00$
Stochastic term, a	2.7%	5.7%
Constant term, b	0.55%	0.55%
Total noise term, σ_N (low luminosity)	155 MeV	205 MeV
Total noise term, σ_N (high luminosity)	210 MeV	245 MeV
Angular resolution	$\sigma_\theta \leq \frac{50mrad}{\sqrt{E}}$ for $\|\eta\| \leq 1$	not essential

Table 8.1: Performance of the electromagnetic calorimeter.

The main parameters of the electromagnetic calorimeter are the energy and coordinate/angular resolutions. The energy resolution is usually parametrized as:

$$\frac{\sigma_E}{E} = \left[\frac{a}{\sqrt{E}} \oplus b \oplus \frac{\sigma_N}{E}\right], \tag{8.1}$$

where a is the stochastic term, σ_n the noise, c the constant term, E is in GeV and $\oplus$ denotes a quadratic sum. The noise term has two sources, namely electronics noise and the pile–up energy deposition; the former is quite important at low energy, the latter is negligible at low luminosity. The stochastic term includes fluctuations in the shower containment as well as a contribution from photostatistics. The constant term can be kept down to the level of 0.55% by *in situ* calibration/monitoring using physics events. Using the preshower detectors could provide the angular resolution of about 45 mrad/$\sqrt{E}$. The main parameters of the CMS electromagnetic calorimeter are listed in the table 8.1. The noise term, presented in the table, corresponds to the energy reconstructed in a 5x5 crystal array.

The next important feature of the calorimeter is the di-photon mass resolution which depends on energy and angular resolution. It is given by the formula

$$\frac{\sigma_M}{M} = \frac{1}{2}\left[\frac{\sigma_{E_1}}{E_1} \oplus \frac{\sigma_{E_2}}{E_2} \oplus \frac{\sigma_\theta}{\tan(\theta/2)}\right], \tag{8.2}$$

where E is in GeV, and θ is in radians. For example, the mass resolution for a 100 GeV Higgs boson decaying into two gammas is calculated to be 650 MeV at low luminosity ($10^{33}\text{cm}^{-2}\text{s}^{-1}$) and 690 MeV at high luminosity ($10^{34}\text{cm}^{-2}\text{s}^{-1}$ at injection).

The Hadron Calorimeter is an essential subsystem of the CMS detector. In conjunction with the electromagnetic calorimeter and the muon system it measures quark, gluon and neutrino directions and energies by measuring the energy and direction of particle jets and of the missing transverse energy flow, and helps in the identification of electrons, photons and muons.

The Central Hadron (HE and HB) calorimeter is a sampling calorimeter: it consists of active material inserted between copper absorber plates. The absorber plates are 5cm thick in the barrel and 8cm thick in the endcap. The active elements of the entire central hadron calorimeter are 4mm thick plastic scintillator tiles read out using wavelength-shifting plastic fibers. The Central Hadron calorimeter covers the η region up to 3. Its energy resolution is $\sigma_E/E \approx 70\%/\sqrt{E[\text{Gev}]} \oplus 9.5\%$ (at η=0) and in the HF, $\sigma_E/E \approx 172\%/\sqrt{E[\text{Gev}]} \oplus 9\%$. In the general case it is a function of η [108].

To extend the hermeticity of the central hadron calorimeter system a separate forward calorimeter (HF) is located 6m downstream of the HE endcaps. HF covers the region $3 \leq \eta \leq 5$. It uses quartz fibres as the active medium, embedded in a copper absorber matrix. The energy resolution of HF is estimated as $\sigma_E/E \approx 182\%/\sqrt{E[\text{Gev}]} \oplus 9\%$ for hadrons and $\sigma_E/E \approx 138\%/\sqrt{E[\text{Gev}]} \oplus 5\%$ for γs and electrons [109].

8.2 TOTEM and its integration with CMS

The TOTEM Collaboration proposed an experiment to measure the total cross section, elastic scattering and diffraction dissociation at the LHC [110]. The integration of the TOTEM experiment into CMS was decided by the LHCC in 1999[1]. It gives the perspectives to study the double Pomeron exchange (DPE), using the CMS+TOTEM setup, in addition to the program of the TOTEM group. As you can see from the previous chapters, the study of DPE is impossible without the precise measurements of the momenta of outgoing protons by the TOTEM detectors as the decay products of the central particle by CMS.

TOTEM physical goals

- Measurement of the total cross section of pp collisions at LHC energy at the earliest stage of operation of the LHC, when it will run with a low luminosity.

- Measurement of the elastic scattering

$$pp \to pp \tag{8.3}$$

  in the largest possible interval of momentum transfer from $-t \simeq 10^{-2}$ GeV^2 (value required for the extrapolation of the elastic scattering to the optical point needed for the measurement of the total cross section) up to at least $-t \sim 10$ GeV^2.

- Study of the diffraction dissociation

$$pp \to pX \tag{8.4}$$

  by detecting with the telescope of Roman pots of one arm in coincidence with the inelastic detector of the opposite hemisphere.

[1]The detailed description of the TOTEM's physical goals, equipments and its integration into CMS can be found in [111]

The detectors

The experimental apparatus, symmetric with respect to the interaction point consists in each part of:

- three Roman pots stations RP1, RP2 and RP3 with elastic scattering detectors inside;
- some forward inelastic detectors located inside two telescopes (T1 and T2, see the figures 8.9 and 8.10).

Three Roman pot stations with a dipole magnet in between will be used to detect the proton which scattered quasielastically in the diffraction dissociation and to measure its momentum. A layout of Roman pots in the underground area inside the LHC tunnel is shown in the figure 8.7. Two roman pot units are combined in a single mechanical structure. Above the sketch 8.7 there is a 3D view of a station of two Roman pot units. The two roman pot stations RP1 and RP2 located between D1 and D2 provide a precise initial angular measurement while the third roman pot station RP3 located behind D2 measures the deflection angle. In order to study the diffraction dissociation, one needs to measure the momentum of the scattered proton by using D2 as a spectrometer analysis dipole. The RP1 station is intended for the measurements of large-t elastic scattering, RP2 for low-t scattering and RP3 for the forward magnetic spectrometer, naturally implemented taking advantage of the strong bending power of the dipole D2, in conjunction with RP1 and RP2.

Inside the pots the tracking detectors of small size (only few cm^2) are located very close (few mm) to the beam. In order to achieve a space resolution of 30 microns, needed to fulfill the physical goals, three variants are considered at present: silicon detectors with (x,y,z) strips or of drift type, scintillating fibres, optoelectronic detectors. Assuming that each station will be composed of several planes of 10μm pitch microstrip detectors then the outgoing proton could be measured with a precision of $\delta p_T \approx$ 50MeV and $\delta p_L \approx$ 7GeV. These values would be sufficient for central production measurements. The detectors inside the Roman pots are placed close to the beam up to $10 \div 15$ σ profiles of the beam. At a distance of L_{eff} =150 m from the interaction point it allows protons that are scattered up to θ =10 mrad to be measured.

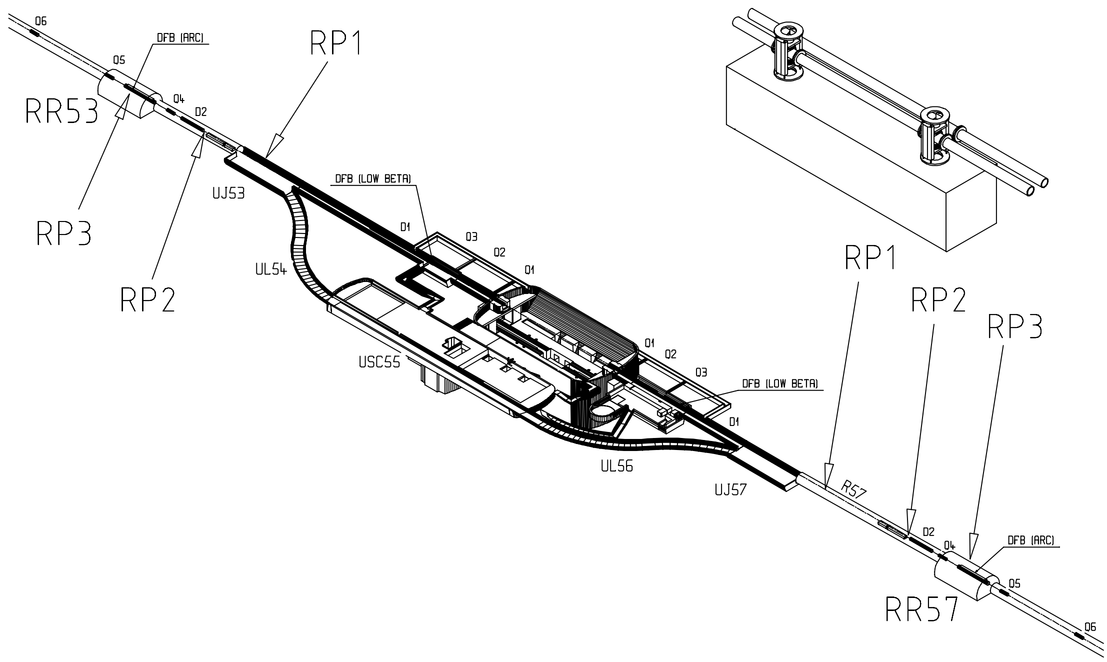

Figure 8.7: Sketch of the underground area and machine equipment inside the LHC tunnel for the measurement of elastic scattering. A station of two Roman pot units is also shown.

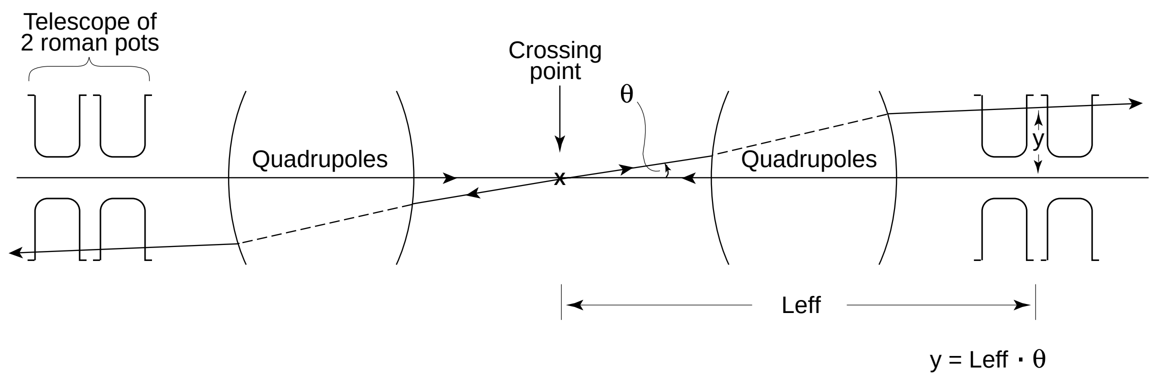

Figure 8.8: Scheme of the forward protons measurement using Roman pots stations.

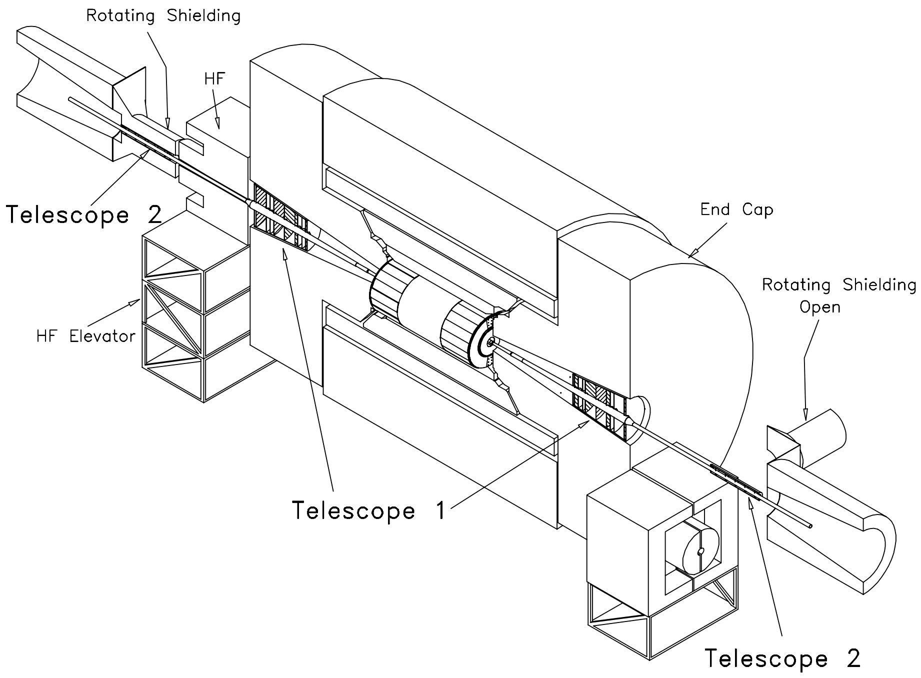

Figure 8.9: An overall view of the integration of the telescopes T1 and T2 into the CMS layout.

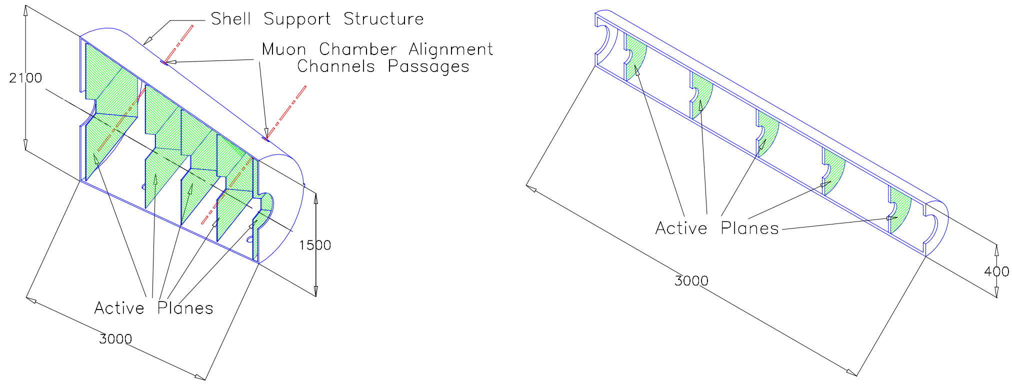

Figure 8.10: Sketch of the telescope T1 (left) and T2 (right).

The scheme of the measurement is presented in the figure 8.8. The η/θ ranges covered by the RP detectors are listed in the table 8.2. As it will be shown below, the η range covered by the RP detectors provides a good efficiency for the registration of central production events.

A forward inelastic detector covers, on both sides of the crossing, an interval of pseudorapidity $3 \leq |\eta| \leq 7$ with full azimuthal acceptance. This detector will be used for the measurement of the inelastic rate including events of diffractive type. The detector is split into two telescopes, T1 and T2. An overall view of the integration of T1 and T2 into CMS is shown in the figure 8.9. T1 is placed inside the end cap region of CMS at a distance between 7.5 m and 10.5 m from the CMS centre, covering the pseudorapidity interval from 3 to 4.9. T2 is placed at a distance between 15 m and 18 m. It covers the pseudorapidity interval from 5 to 7. It has to be installed in the rotating shielding of CMS.

Each telescope is composed of five equally spaced detector planes capable of measuring a space point, see the figure 8.10. The space resolution needed for each point is of the order of the *millimeter* since it is only required to reconstruct the collision point accurately enough to disentangle beam-beam events from background. This can be achieved by dividing each detector plane in six separate sectors. Each sector will be a MWPC-like detector with simultaneous R/O of three coordinates from the wires and from the two planes of the cathode pad strips. It is assumed that both the sense wires and the strips have 2 mm pitch. It will give the following precision of momentum measurements $\delta p_T \approx 50$MeV and $\delta p_L \approx 7$GeV.

Detector	T1	T2	RP
Pseudorapidity range	$3 \leq \|\eta\| \leq 4.9$	$5 \leq \|\eta\| \leq 7$	$9.2 \leq \|\eta\| \leq 12.2$
Corresponding θ range, mrad	$13 \leq \theta \leq 100$	$1.8 \leq \theta \leq 13$	$0.01 \leq \theta \leq 0.2$
z position, m	7.5 - 10.5	15 - 18	≈150

Table 8.2: Parameters of the TOTEM detectors.

The operation of TOTEM

To perform successful measurements at very small scattered angles TOTEM needs some special parameters for the beam, which are different from the nominal LHC conditions. It requires:

- run with high-β optics ($\beta_{TOTEM} = 1000 \div 1500$m), instead of nominal LHC $\beta_{nom} = 0.5$m;
- decrease the number of bunches, $n_{TOTEM}/n_{nom} \approx 10^{-2}$.

Such conditions led to the decreasing of the luminosity from $L_{nom} = 10^{34}$cm^{-2}s^{-1} to $L_{TOTEM} = 10^{28}$cm^{-2}s^{-1}. The measurements can be performed in special runs during the early running-in phase of the LHC, taking periods of a few days. As it will be shown below the conditions suggested by the TOTEM group are well-suited for the measurements of double exchange processes.

8.3 Simulation tools

CMSJET

For the numerical simulations the program CMSJET[112] was used. This program provides a fast non-GEANT [113] simulation of the CMS detector response. The program is exploited in studies of Standard Model heavy Higgs, MSSM, SISB and others and gives results which are coincident with the results of the GEANT-based program CMSIM [114] officially used by the CMS Collaboration for the detailed detector simulations. The program CMSJET is widely used when physical tasks require the generation of millions of background events. In such cases the detailed detector simulation cannot be applied, while one still needs some reasonable estimations of the detector response. The program is basically oriented on the jet physics applications, but we adopted it for the study of double exchange processes.

The main features of the program are listed below [115]:

- PYTHIA[116], ISAJET[117] and HERWIG[118] interfaces;
- full granularity HCAL (towers) and ECAL (Xtals);

- 4T magnetic field (helix parametrization);
- energy smearing parametrization based on GEANT simulations;
- longitudinal and transversal parametrization of electromagnetic and hadron shower profiles based on [119];
- noise simulation (for all cells or for only fired cells);
- "dead" cells simulation;
- CMSIM-like pile up admixture;
- some cracks description (degraded response, energy dissipation);
- smearing of charged track and muon momenta.

To the above-listed features the simulation of the gammas conversion to e^+e^- pairs was added. The calculation of the conversion probability is based on the knowledge of the quantity of material in the tracking volume in units of radiation length as a function of pseudorapidity, as shown in the figure 8.3. The TOTEM detectors were included in the simulation, and the events generator for central production at high energies was added to the program codes.

Events generator for central production at high energies

The reaction 1.1 of double Pomeron exchange, at $\sqrt{s}$ =14 TeV, has been generated using a modified version of the WA102 event generator. The distribution on x_F of outgoing protons and on t, the four momentum transfer squared of the proton vertices, measured and parametrised by the WA102 experiment are used in the generation. The s dependences of these variables were taken into account according to [120]. The x_F distribution has been assumed to scale as $1/\sqrt{s}$:

$$\left(\frac{dN}{dx_F}\right)_{CMS} = e^a \left(\frac{dN}{dx_F}\right)_{WA102}, \quad a = \sqrt{\frac{s_{WA102}}{s_{CMS}}} = 0.002 \tag{8.5}$$

The slope parameter b of the proton vertex is parameterised as

$$b_{CMS} = b_{WA102} + 2\alpha' ln\left(\frac{s_{CMS}}{s_{WA102}}\right), \tag{8.6}$$

where $\alpha' = 0.25$ [121], $b_{WA102} = 6 \div 8$ GeV^{-2} was measured at $\sqrt{s} = 28$ GeV by the WA102 experiment. Then b_{CMS} at $\sqrt{s}$ =14 TeV is equal to $12 \div 14$ GeV^{-2}. The x_F and t dependences of the outgoing protons at CMS energy ($\sqrt{s}$ =14 TeV) and WA102 energy ($\sqrt{s}$ =28 GeV) are presented in the figure 8.11.

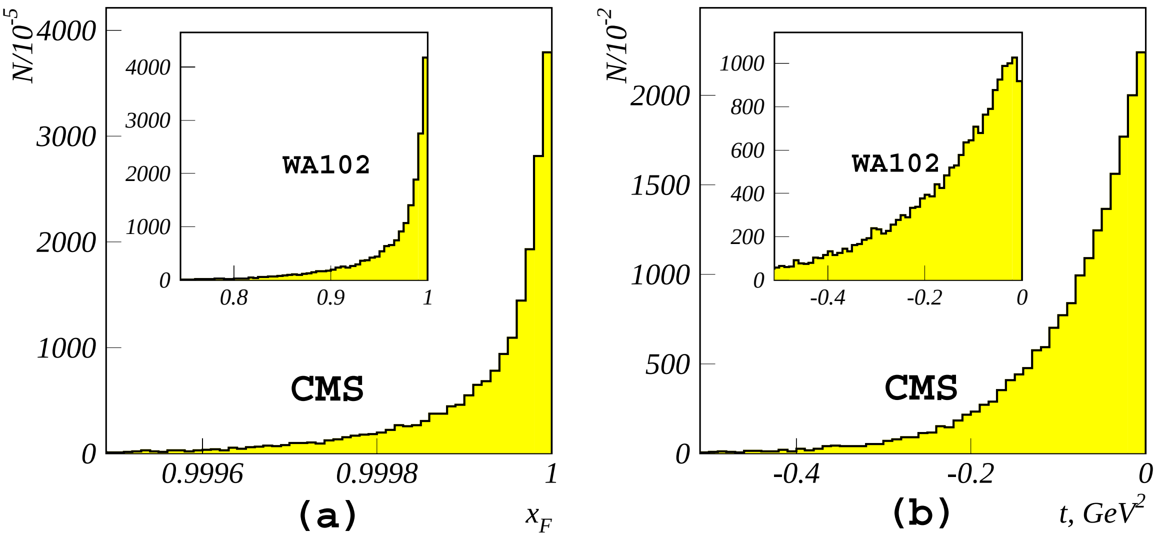

Figure 8.11: x_F (a) and t (b) dependences of outgoing protons for central production at CMS and WA102 energies.

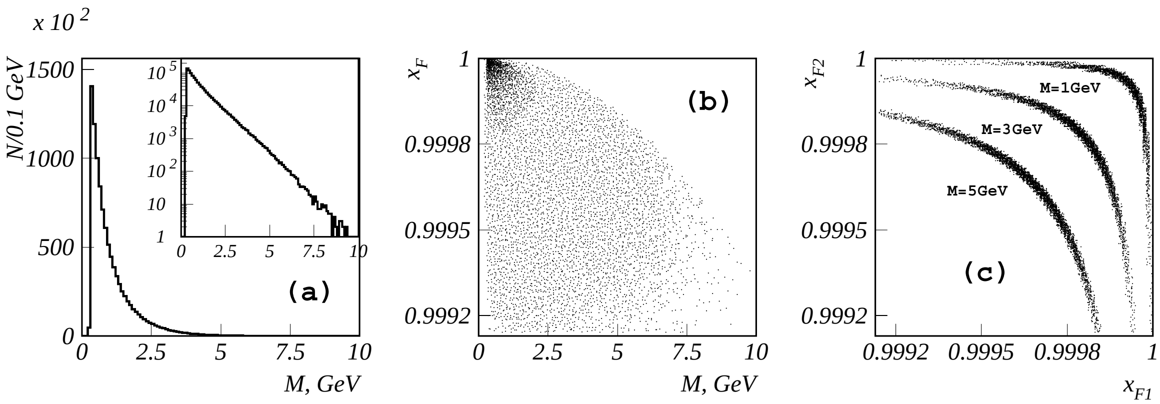

Figure 8.12: (a) distribution on the mass M of the central particle, (b) two-dimensional distribution on M and x_F and (c) two-dimensional distribution on x_{F1} and x_{F2} for several fixed masses for central production at CMS energy.

x_F and t define the longitudinal and transversal components of the protons momenta accordingly and therefore the full kinematics of the reaction 1.1. The mass M of the central particle and the variables x_{F1} and x_{F2} are connected by the relation:

$$M^2 = s(1 - x_{F1})(1 - x_{F2}). \tag{8.7}$$

The distribution of the mass M of the central particle (a) and two-dimensional distributions (b) and (c), illustrating the relation 8.7, are presented in the figure 8.12. From the figure 8.12 (b) and (c) it is seen that small X masses are produced at x_F close to 1 dominantly.

8.4 Efficiency and mass resolutions

The reaction 1.1 has been generated for different decay channels of the central particle X^o to estimate an efficiency of the registration of neutral as well as of charged decay modes.

Neutral decays

First, we consider the neutral decay of X^o to $\pi^o\pi^o$, where each π^o decays to 2γ. Thus, in the final state of the reaction 1.1 we have 2 protons and 4γ. The outgoing protons must be detected in the Roman pot detectors and the gammas must be detected in the central calorimeter (EE or EB). The gammas conversion in the tracking system is taken into account. The energy and the momentum resolution of the detectors are also included in the simulation.

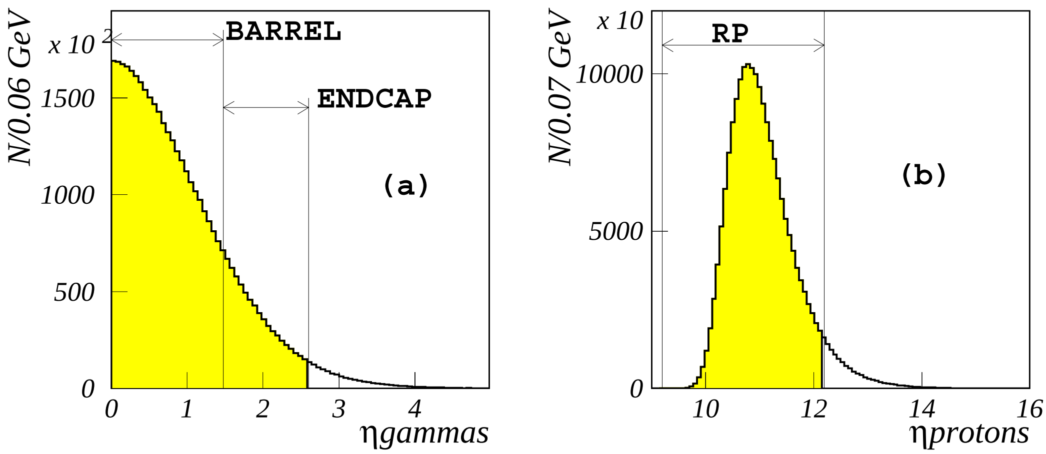

Figure 8.13: Distributions of pseudorapidity η for γs (a) and protons (b). The η-sizes of the calorimeters (EB and EE) and of the Roman pot (RP) are shown.

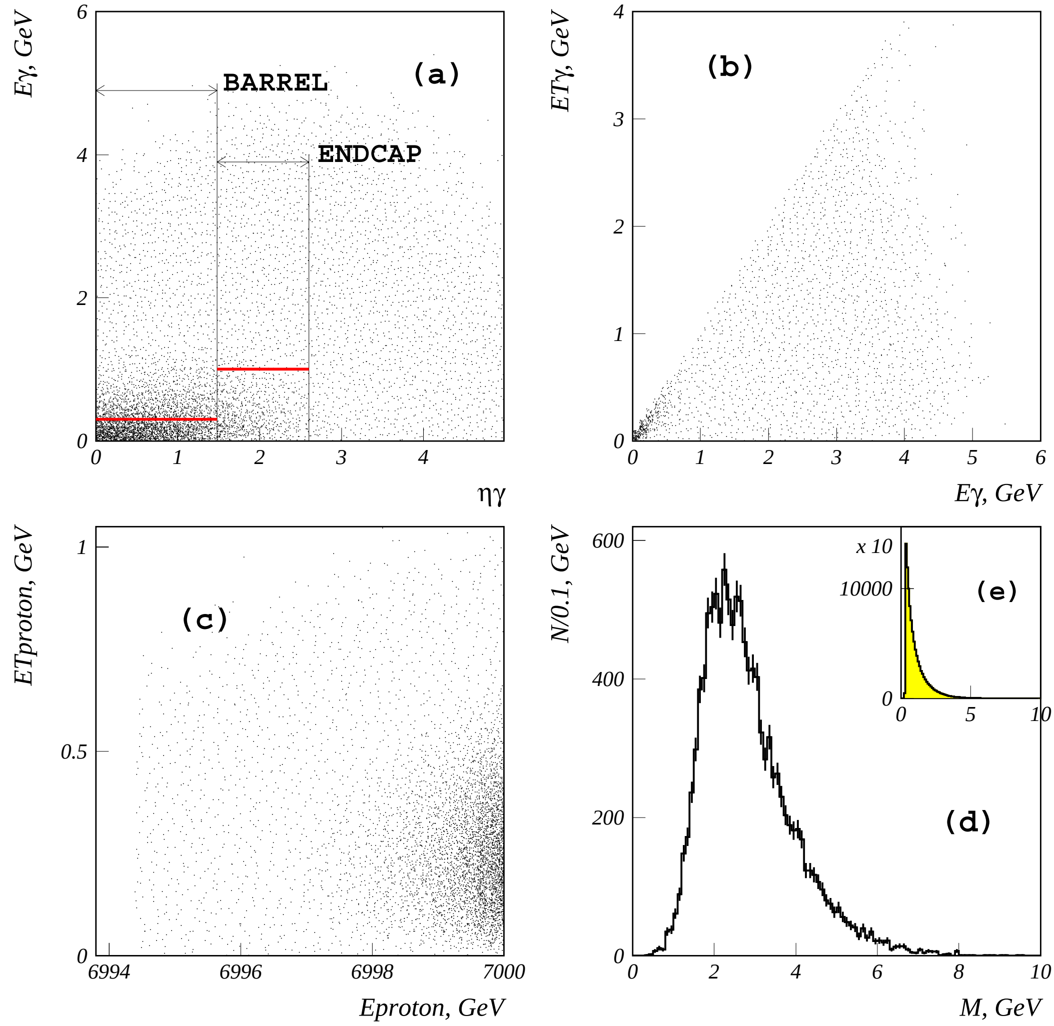

Figure 8.14: (a) – two-dimensional distribution of η and gamma's energies. The vertical lines show the η-sizes of EB and EE, the horizontal lines show the cuts on the gamma energies in EB and EE. (b) – two-dimensional distribution of gamma energies and gamma transversal energies. (c) – two-dimensional distribution of protons momentum and transversal momentum. (d) – distribution of the "measured" X mass. In the insert (e) the simulated X mass is shown.

The figure 8.13 shows the distributions of the pseudorapidity η for the simulated gammas and protons. A good acceptance is seen for gammas as for protons. The figure 8.14 shows the distributions of the gammas and protons energy. It is seen that the gammas have very low momenta with a large contribution of transversal component. The outgoing protons are scattered with small transversal and large longitudinal momenta, which are close to the beam momentum. In contrast to the WA102 fixed target experiment, where the central particle acquires a comparatively huge longitudinal component due to the boost from the centre of mass frame to the laboratory frame, in the collider the central particle forms while almost stationary. The gammas with low energy decrease the efficiency essentially because the noise terms in the resolution of the electromagnetic calorimeters, see 8.1, are rather big. The two horizontal lines in the figure 8.14 (a) show the related low limits of the measured gamma energies.

Required cut	Events percentage after cut, %
η size of calorimeter	87.3
γ's conversion in tracker	24.6
Cut on γ's energy in EB	12.7
Cut on γ's energy in EE	64.2
Total γ's efficiency	1.4
Total proton's efficiency	88.7
Total efficiency	1.2

Table 8.3: Contributions of different factors to the efficiency of the reaction $pp \rightarrow pX^o p, X^o \rightarrow 2\pi^o \rightarrow 4\gamma$.

The calculated efficiencies are listed in the table 8.3. As it can be seen from the table, the gamma conversion in the tracker and the energy cut in the Barrel ECAL strongly suppress the detection of the events. This, with the other factors taken in account, is the reason of a small total efficiency, 1.2%. The distribution of the X mass "measured" with an efficiency 1.2% is shown in the figure 8.14 (d). The insert (e) shows the simulated X mass. It is seen that the detectors parameters allow measurements in the range of X mass from 1 to 6 GeV to be performed. This mass region is of interest for the meson spectroscopy and the search for exotic states.

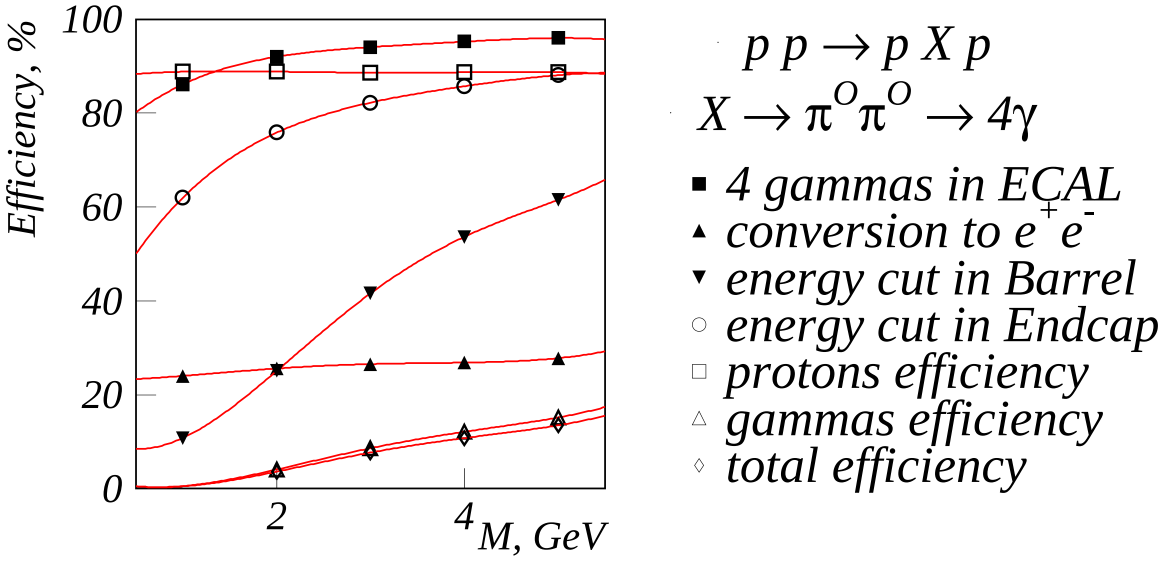

Figure 8.15: Mass dependence of the efficiency for the reaction $pp \to pX^o p, X^o \to 2\pi^o \to 4\gamma$. The curves show the contribution of the different factors (described in the table 8.3 and in the text), suppressing the registration of events, to the total efficiency.

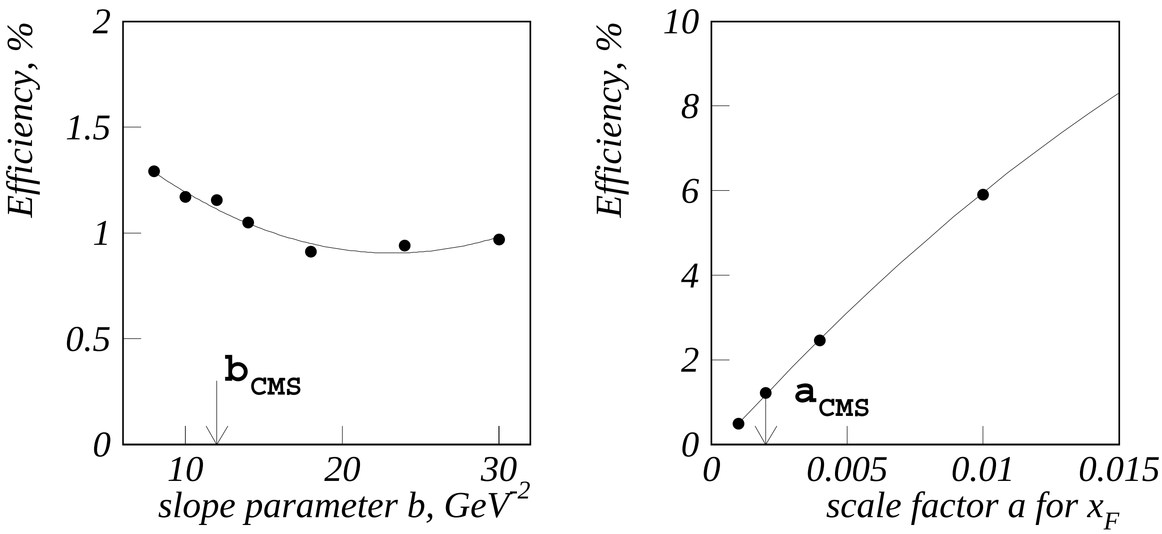

Figure 8.16: Efficiency as a function of the scaling factor a for x_F (a) and as a function of the slope parameter b of the t distribution (b).

The efficiency as a function of the X mass is shown in the figure 8.15. The contribution to the total efficiency of the different factors, suppressing the registration of events, is also shown. One can see that the γ conversion and the protons registration are stable and do not depend on the X mass. The other contributions become stable in the mass region above 2 GeV and the suppression of the events by an energy cut in ECAL decreases with the mass.

As mentioned above, in the events generator two important parameters are used, the slope parameter b of the t distribution and the scaling factor a of x_F. The calculations rely on values measured by WA102 and on theoretical assumptions of the s dependences, see equations 8.5 and 8.6. The efficiency as a function of a and b has been studied. The figure 8.16 (b) shows a weak dependence on b, so we do not have to worry about our assumption about the b value. The a-dependence of the efficiency, fig.8.16 (a), is approximately linear.

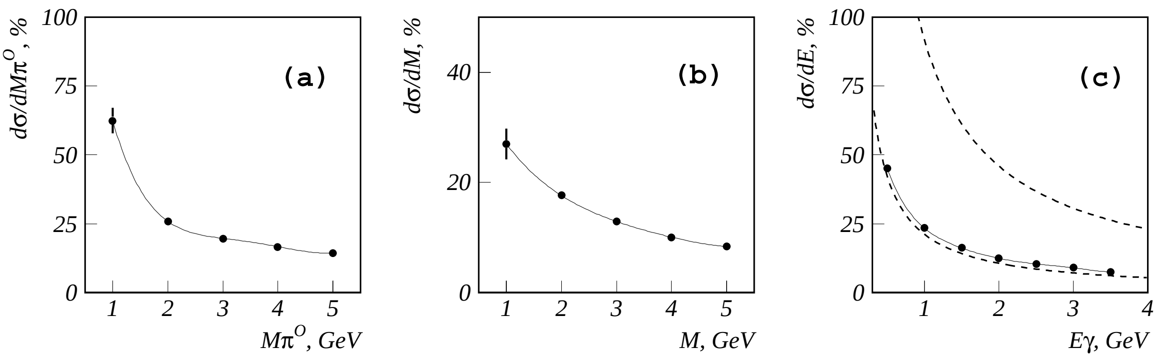

Figure 8.17: The relative mass resolution on 2γ from π^o decay $d\sigma_{M_{\pi^o}}/dM$ (a) and of the X mass $d\sigma_M/dM$ (b) as a function of M and the resolution of γ's energy (c) $d\sigma_{E_\gamma}/dE_\gamma$ measured by ECAL. The dotted curves show the energy resolution on γ detected by the ECAL Barrel (bottom curve) and the ECAL Endcap (top curve).

The mass resolution of the calorimetr has been studied as a function of the X mass. The relative resolution on the X mass, $d\sigma_M/dM$, is shown in the figure 8.17 (b). It decreases from 25% at 1 GeV to 10% at 5 GeV. The relative mass resolution of 2γ from π^o decay, $d\sigma_{M_{\pi^o}}/dM_{\pi^o}$ (fig.8.17 (a)), is equal ≈20% in a X mass region above 2 GeV and increases exponentially below 2 GeV. The figure 8.17 (c) shows the resolution on γ's energy $d\sigma_{E_\gamma}/dE_\gamma$. It is a little higher than the curve of the relative energy resolution in the ECAL Barrel (the top curve in the figure 8.17 (c) shows the relative energy resolution in the ECAL Endcap). It reflects the fact that gammas are detected by the Barrel dominantly, as it can be seen in the figure 8.18 (a), showing the percentage of gammas detected by the Barrel and the Endcap.

To estimate the efficiency for different γ's multiplicity in the final state, the X decays to 2γ and to $3\pi^o \to 6\gamma$ have been generated. The result is shown below:

X decay	Efficiency, %
$X \to 2\gamma$	2.4
$X \to 2\pi^o \to 4\gamma$	1.2
$X \to 3\pi^o \to 6\gamma$	0.2

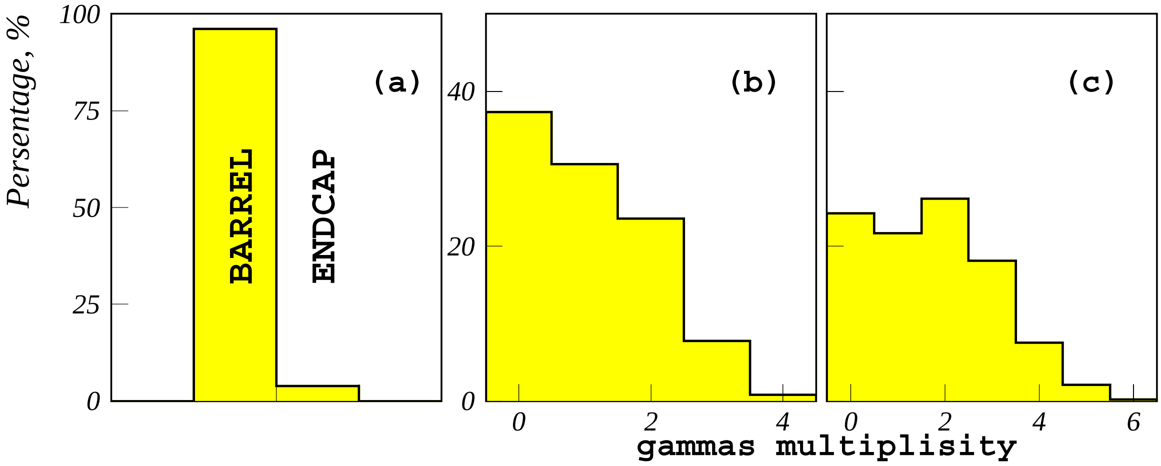

Figure 8.18: Percentage of γs detected by the ECAL Barrel and the ECAL Endcap (a), and percentage of events with different gamma multiplicity in the final state for decays $X \to 2\pi^o \to 4\gamma$ (b) and $X \to 3\pi^o \to 6\gamma$ (c).

Due to the small efficiency of the gamma detection, the gamma multiplicity in the final state of the recorded event is very different of the physical original event. The figures 8.18 (b) and (c) show how the gamma multiplicity of the recorded event changes its original value after a selection of the X decays to 4γ and 6γ respectively. Thus one has to expect a huge background in the gammas spectrum from events with higher multiplicity. The estimation and the suppression of such a background is an individual task for each of the decay modes. In general one can use the balance of the total transversal momentum P_T. In order to do this we need: the spread in the transverse momentum of the incident beam momentum to be small, and small measurement errors on the outgoing protons. The first condition is in agreement with the plans to run TOTEM with the maximum β possible in order to reduce the luminosity, which will give $\delta P_T \leq$ 10MeV. The second condition is provided by high precisions Roman pot's detectors which will give $\delta P_T \approx$ 50MeV. These conditions allow the losses of the π^os to be ignored.

Charged decays

In order to investigate the efficiency of the charged decays registration, the decay $X^o \rightarrow \pi^+\pi^-$ has been generated. In this case there are 2 protons and 2 π mesons in the final state of the reaction. The outgoing protons are required to be detected in the Roman pots. The tracks are required to have geometrical acceptance within the CMS tracking system ($|\eta| \leq 2.6$). The trajectory of the $\pi^\pm$ is bent by the field, it is also required that the track hits one of the calorimeters to measure its energy. The energy and the momentum resolution of the detectors are included in the simulation.

The distribution of the pseudorapidity η for the simulated $\pi^\pm$ mesons, figure 8.19 (a), shows a good acceptance of the track registration. The figure 8.19 (b) shows the distribution of the pseudorapidity of the final points of the detected tracks, i.e. the pseudorapidity of the hits in the calorimeters. It is seen that the field changes the original distribution of η and a major part of the tracks is detected by the Endcap calorimeters. The dip in the distribution at $\eta \approx$1.5 is due to the crack between the Barrel and the Endcap. The figure 8.19 (c) illustrates the range of tracks momentums and transversal momentums. In contrast to neutral decays $\pi^\pm$ mesons are well detected in the full range of X mass, which is illustrated by the figure 8.19 (d) and (e) (that have to be compared with the figure 8.13 (d) and (e)).

The calculated efficiencies are listed in the table 8.4. It is seen that the total efficiency is higher than the efficiency for neutral decays by approximately 10 times. The efficiency as a function of the X mass has been studied and the result is shown in the figure 8.20. The efficiency of the tracks registration increases fast and becomes higher than the efficiency of the proton registration above 2.5 GeV. Thus, above 3 GeV we have a very high efficiency (close to 90%) which is only limited by the efficiency of the proton registration.

The mass resolution of the tracker has been studied as a function of the X mass. The relative resolution on the X mass $d\sigma_M/dM$ is shown in the figure 8.21 (a). It is

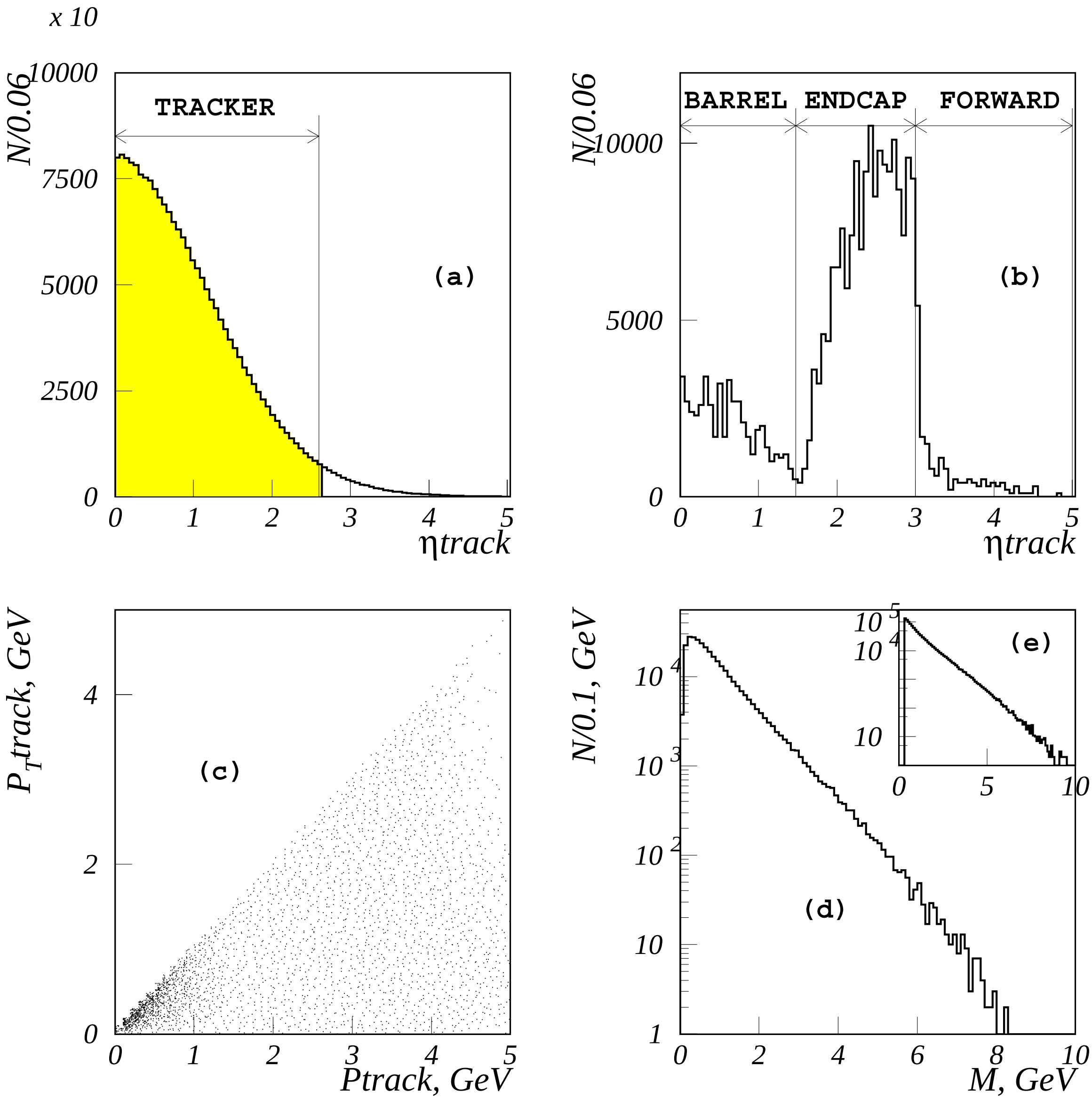

Figure 8.19: (a) distribution of the pseudorapidity η for $\pi^{\pm}$ mesons. The η-limit of the tracker system is shown. (b) distribution of the pseudorapidity of track's hits in the calorimeters. The η-limits of the calorimeters are shown. (c) distribution of the track's momentum and the track's transversal momentum. (d) distribution of the "measured" X mass. In the insert (e) the simulated X mass is shown.

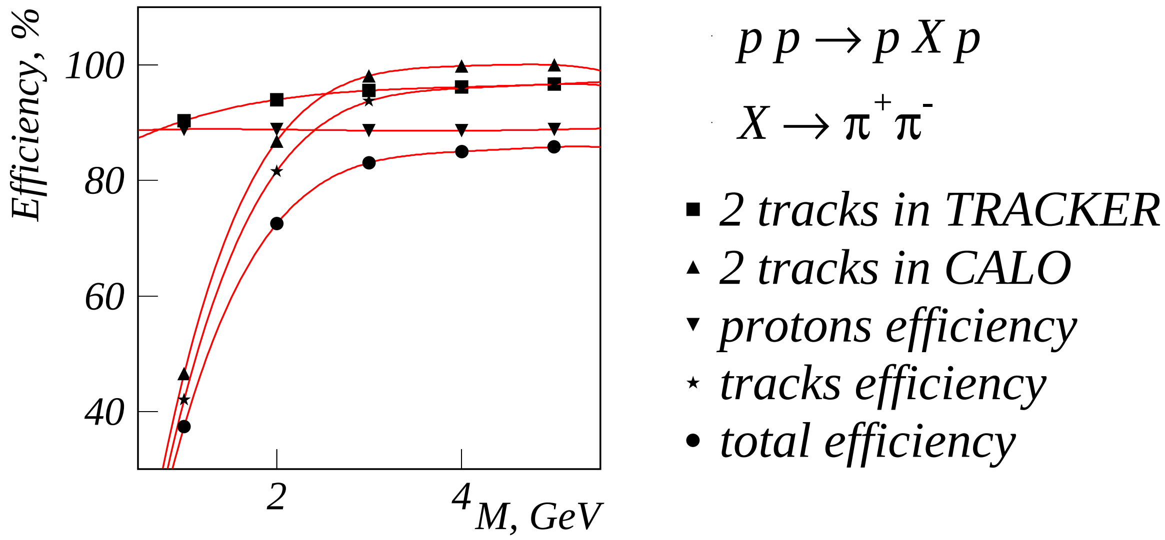

Figure 8.20: Mass dependence of the efficiency for the reaction $pp \to pX^o p, X^o \to \pi^- \pi^+$. The curves show the contribution of the different factors, (described in the table 8.4 and in the text), suppressing the registration of events, to the total efficiency.

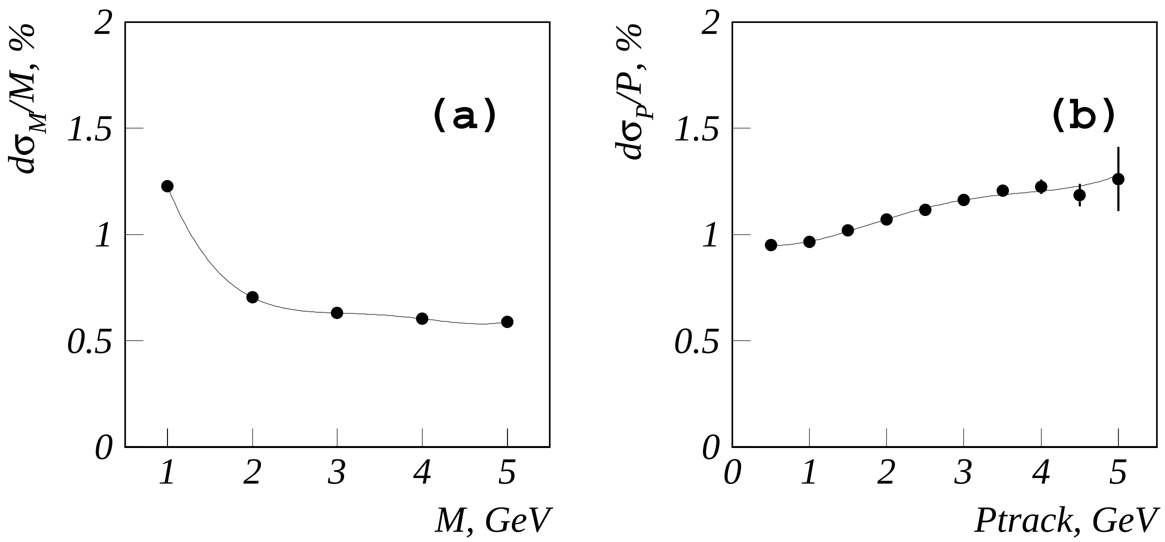

Figure 8.21: Tracker mass resolution, $d\sigma_M/dM$ (a), and momentum resolution, $d\sigma_P/dP$ (b).

Required cut	Events percentage after cut, %
η size of tracker	90.3
hit in calorimeter	39.5
Total track's efficiency	35.7
Total proton's efficiency	88.8
Total efficiency	31.7

Table 8.4: Contributions of the different factors to the efficiency of the reaction $pp \to pX^o p, X^o \to 2\pi^-\pi^+$.

equal to ≈0.7% above 2 GeV and rises up to ≈1.2% at 1 GeV, which is a lot better than in the case of neutral decays. The tracker momentum resolution is shown in the figure 8.21 (b).

In order to estimate the efficiency of the registration of charged decays with a final multiplicity higher than 2, the decay $X \to \rho\rho \to \pi^+\pi^-\pi^+\pi^-$ has been generated and an efficiency of 12.3% has been obtained.

Summarizing the results of the simulations for neutral and charged decays, one can conclude that charged modes are preferable for the study of central production with regard to the efficiency of registration and to the mass resolution. As mentioned above, the precision of the outgoing protons measurements allows decays that involve a π^o to be excluded by using momentum balance and, thus, charged decay modes to be selected for study.

8.5 Study of the background and requirements for DPE selection

In order to investigate the background to the central production, we use the standard set of PYTHIA's parameters for the minimum bias [116]. In addition the processes which have a similar kinematics with double Pomeron exchange (DPE), such as elastic scattering, single diffraction, double diffraction, are included in the background.

The cross section for DPE at the LHC energy can be estimated using the results of WA102. The cross section of DPE at $\sqrt{s}$ = 28 GeV is σ_{DPE}=0.14 mb. From equations 1.2 one can see that σ_{DPE} is a constant approximately in terms of s. To be more precise, σ_{DPE} depends on s as $s^{0.08}$, that is predicted by the theory [120] and confirmed by the WA102 measurements [4]. Thus, we can assume that at $\sqrt{s} = 14$TeV σ_{DPE}=0.37 mb. The DPE process is generated with the minimum bias processes jointly. To give an example, we consider one fixed decay channel of the central particle X: $X \to \eta\eta$, where each η decays to $\pi^+\pi^-\pi^o$. Thus, we have as gammas (4γ) as charged mesons ($2\pi^+2\pi^-$) in addition to 2 protons in the final state of the central production reaction.

All processes, generated for the background study, are listed in the table 8.5. We included the process of DPE to PYTHIA, using the above mentioned generator, and numbered it as 200. The relative cross-sections of the processes are shown graphically in the figure 8.22 (a) and also listed in the table 8.5. The figure 8.23 shows the flux of gammas and charged particles in the calorimeters, in the tracking system and in the TOTEM detectors.

Process	Number in PYTHIA	Cross-section, mb
$ff' \to ff'$ (QCD)	11	1.0880
$f\bar{f} \to f'\bar{f}'$	12	0.0193
$f\bar{f} \to gg$	13	0.0142
$fg \to fg$	28	15.1700
$gg \to f\bar{f}$	53	1.0800
$gg \to gg$	68	37.8500
Elastic scattering $pp \to pp$	91	22.2100
Single diffractive $pp \to Xp$	92	7.1513
Single diffractive $pp \to pX$	93	7.1513
Double diffractive $pp \to X_1X_2$	94	9.7800
Low-p_T scattering	95	0.0002
DPE $pp \to pXp$	200	0.3700
All included processes		101.4000

Table 8.5: Processes generated for the background study.

The main kinematical feature of central production reactions is the presence in the final state of two low-p_T scattered protons, moving in opposite directions. So the first requirement for DPE selection should be the detection of one track in the forward

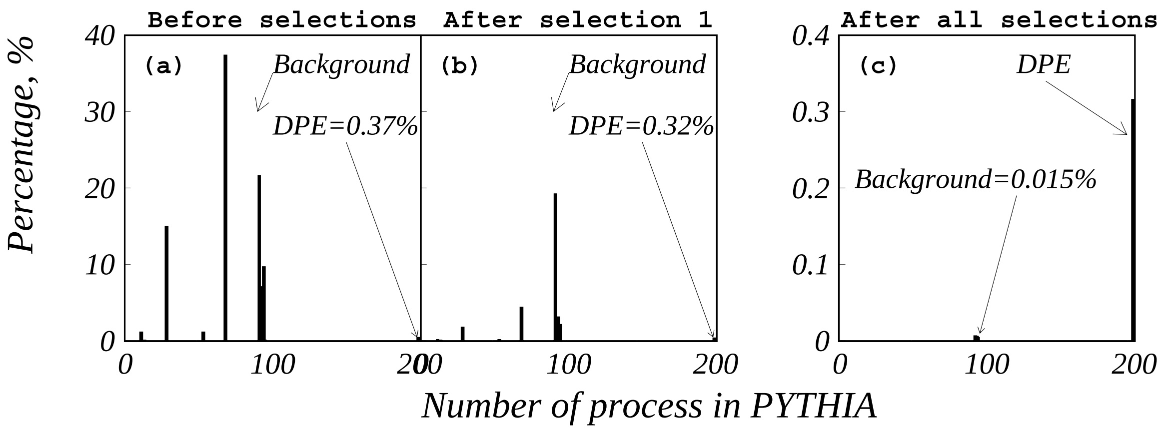

Figure 8.22: Percentage of different background processes and DPE production before the selections (a), after the selection 1 (b) and after all selections (c). See table 8.6 and text.

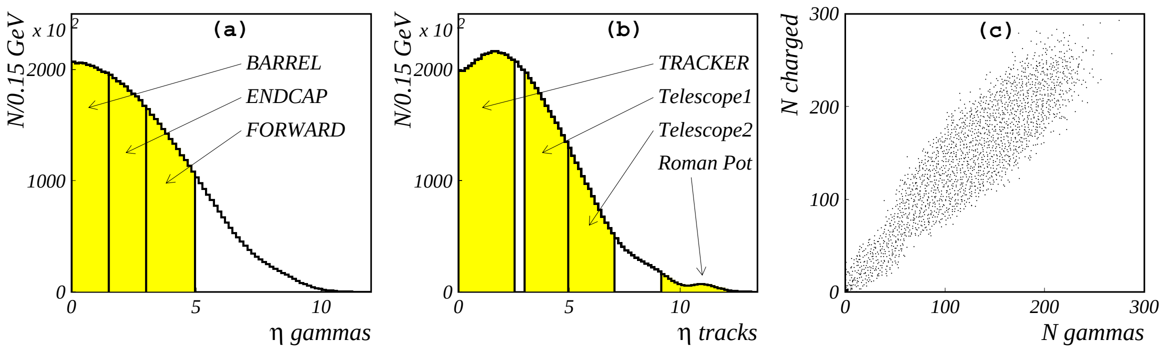

Figure 8.23: Distributions of the pseudorapidity of γ's (a) and tracks (b) for the minimum bias events. The η-limits of the detectors are shown. (c) – distribution of the multiplicities of γs and tracks for the minimum bias events.

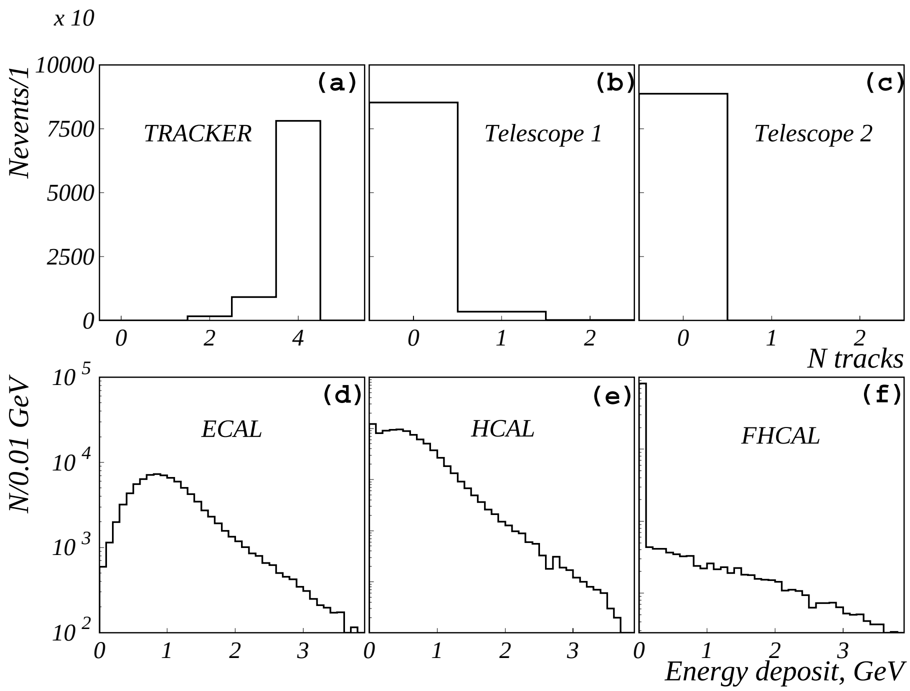

Figure 8.24: Energy deposit and number of tracks in the CMS and the TOTEM detectors for DPE production.

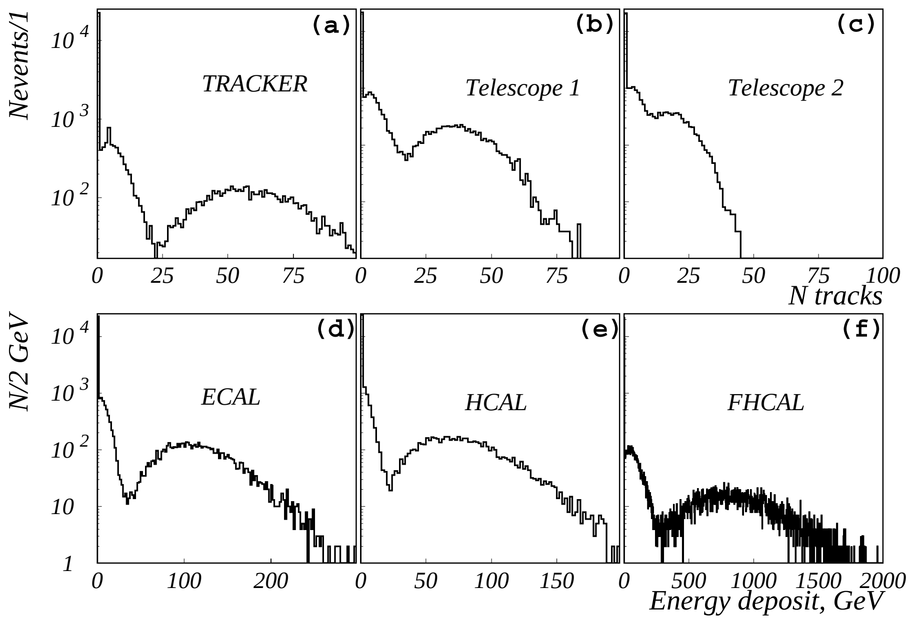

Figure 8.25: Energy deposit and number of tracks in the CMS and the TOTEM detectors for the background.

Roman pot and one track in the backward one. This requirement decreases the number of background events by more than twice, down to ≈34%. The percentage of background processes after the first selection is shown in the figure 8.22 (b). It is seen that processes 11÷68 from the table 8.5 are suppressed and the main contribution to the rest of the background is given by the elastic scattering and the diffractive processes.

Selection	Requirement	Bg, %	DPE, %
	No selections	99.63	0.365
1	two opposite tracks in Roman pots	34.02	0.323
2	1 * (0 < Energy deposit in ECAL < 4 GeV)	5.26	0.319
3	1 * (Energy deposit in HCAL < 4 GeV)	32.10	0.323
4	1 * (Energy deposit in FCAL < 10 GeV)	21.49	0.322
5	1 * (Tracks in Telescope1 ≤ 2)	23.13	0.323
6	1 * (No tracks in Telescope2)	21.03	0.323
Total	All selections	0.015	0.315

Table 8.6: Selection requirements for a central production study.

The figures 8.24 and 8.25 show the energy deposit in the CMS calorimeters and the number of tracks in the TOTEM tracking detectors for DPE production and the background processes after the selection 1. The elastic scattering has two protons in the final state only and can be rejected by the requirement of signals in one of the calorimeters or tracker. To suppress the rest of the background from the other processes one can use the low energy deposit of the DPE events in the calorimeters in comparison with the background events. In the table 8.6 are listed the software conditions on the energy deposit in the CMS calorimeters and the selection requirements in the TOTEM detectors which allow the background to be very effectively suppressed, less than 0.02% of the initial background events. And, at the same time, these requirements save more than 85% of the DPE events. The ratio of DPE to background before and after selections is shown in the figure 8.22 and is presented below:

$$\left(\frac{N_{DPE}}{N_{bg}}\right)_{before\ selections} \approx 0.004, \qquad \left(\frac{N_{DPE}}{N_{bg}}\right)_{after\ selections} \approx 20.$$

8.6 Summary

New results from central production show that this is a mechanism which can be used to a great advantage in the study of the hadronic spectra. New effects are observed in *pp* central collisions, such as a kinematical filter, which can select out glueball candidates, and a non-flat azimuthal distribution of outgoing protons, which can be explained by the non-zero spin of the Pomeron. It would be of great interest to extend these studies to the LHC energies, where a pure double Pomeron exchange (DPE) is predicted. It gives a feeling of great achievement to study the nature of the Pomeron, to solve the "glueball puzzle" and to understand the underlying dynamics of the DPE.

The assembly of the CMS and TOTEM detectors gives the unique opportunity to study DPE at the LHC energies. TOTEM allows low-p_T scattered protons to be measured and the CMS detectors can measure the decay products of the central particle. The DPE study is in the frame of the TOTEM physical program. The trigger for elastic protons scattering, which should be studied in the frame of the TOTEM program, can be applied for DPE selection. The elastic scattering and the diffraction dissociation, which will be measured by TOTEM, are the main background processes for DPE. So, we will have a good opportunity to select these processes from DPE.

One of the major requirements of DPE measurement is that we are able to reconstruct exclusive events. TOTEM is going to perform measurements with high-β beam, which gives small δP_T for beam protons. The Roman pot stations also provide a good momentum resolution for outgoing protons. They allow to exclude the losses of particles with masses higher than 120 MeV and obtain a much better ratio "signal/background" comparing with inclusive reactions.

For high-β runs the reference luminosity is L=$10^{28} cm^{-2} s^{-1}$. The elastic trigger rate is expected to be of the order of 300 events/s. Then the expected number of DPE events will be 5 events/s. Taking into account the efficiency of the total trigger this would give an integrated data sample of $\approx$ 350000 DPE events per day.

Conclusion

The main results of this study are listed below.

- For the first time the partial-wave analysis of the centrally produced $\eta\pi^o$ system in the reaction $pp \to p(\eta\pi^o)p$ has been performed. The $a_0^0(980)$ and $a_2^0(1320)$ resonances have been observed in the S and D_+ waves respectively. The other waves, including exotic P-wave, are statistically insignificant.

- Also for the first time the partial-wave analysis of the centrally produced $\eta\pi^-$ system in the reaction $pp \to p(\eta\pi^-)\Delta^{++}$ has been performed. The obtained results are similar to the results of the partial-wave analysis of the neutral $\eta\pi$ system: the $a_0^-(980)$ and $a_2^-(1320)$ resonances have been observed in the S and D_+ waves respectively; the other waves are statistically insignificant.

- The masses and the widths of the observed resonances have been measured. The production of the $a_0(980)$ resonance relatively to the $a_2(1320)$ production has also been measured for the neutral and charged channels. The difference in the relative cross-section of the $a_0(980)$ and $a_2(1320)$ productions for the neutral and charged channels can be explained by a mixing of the $a_0^0(980)$ and $f_0(980)$ resonances via the $K\bar{K}$ system. The intensity of the $a_0^0(980) - f_0(980)$ mixing is equal to 8±3%.

- The observation of the scalar $a_0(1450)$ and the tensor $a_2(1650)$, made by some experimental groups, has not been confirmed in the central production in pp collisions. The exotic P wave, seen by all experimental groups that studied the $\eta\pi$ system earlier, has not been observed in the central production in pp collisions. The possible phenomenological explanation of this fact, that requared some assumptions, has been given in the chapter 7.

- The dependences of the resonance production on the kinematical variables dP_T, t and ϕ_{pp}, carring out the information about the mechanism of the central production in pp collisisons, have been measured for the $a_0^0(980)$, $a_0^-(980)$, $a_2^0(1320)$ and $a_2^-(1320)$ states. These dependences are consistent with the hypothesis of a dominant Reggeon-Pomeron exchange in the production of the above-mentioned resonances.

- Numerical simulations of central production with the CMS+TOTEM facility at the LHC energy have been performed. The perspectives of central production measurements with the CMS and TOTEM detectors have been studied:

  - the efficiencies of the events registration for some neutral and charged decay channels of the central particle are calculated;

  - the dependences of the efficiency on the important kinematic variables are studied;

  - the resolution of the detector on the mass of the central particle are calculated;

  - the probable background processes are studied;

  - the conditions to select the events of the double Pomeron exchange and to suppress the background are suggested.

We can conclude that the CMS+TOTEM facility give the unique opportunity to study the double Pomeron exchange at the LHC energies, where a pure double Pomeron exchange is predicted. It gives a feeling of great achievement to study the nature of the Pomeron, to solve the "glueball puzzle" and to understand the underlying dynamics of the double Pomeron exchange. The number of double Pomeron events, which could be measured, is estimated about 350000 per day at a luminosity of $10^{28}\mathrm{cm}^{-2}\mathrm{s}^{-1}$.

The project of the double Pomeron exchange study at the LHC required further MC simulations for more detailed investigations of the trigger requirements and background.

Acknowledgment

Numerous people have contributed to the making of this thesis. The experiment WA102, described in this thesis, has been performed together with these Russian colleagues: A.Blick, A.V.Dolgopolov, S.V.Donskov, A.V.Inyakin, G.V.Khaustov, V.N.Kolosov, A.A.Kondashov, A.A.Lednev, S.A.Polovnikov, V.A.Polyakov, V.Romanovsky, V.Samoylenko, A.Soloviev, P.M.Shagin, V.P. Sougonyaev; these British colleagues: F.E.Close, B.C.Earl, D.Evans, J.B.Kinson, O.Villalobos-Baillie, M.F.Votruba; these Japanese colleagues: T.Hino, S.Inaba, H.Shimizu, Y.Yasu and colleagues from Switzerland, Norway, Belgium, Greece: F.G.Binon, K.M.Danielsen, B.R.French, A.Jacholkowski, T.Jacobsen, V.Lenti, M.Stassinaki. I would like to express my gratitude to all these colleagues for the fruitful joint work during many years.

Many thanks to all my French colleagues from LAPP, Annecy-le-Vieux, for their help in the Monte-Carlo simulations for CMS: Y.Baek, D.Boget, M.Maire, J.P.Mendiburu, P.Nedelec and D.Sillou.

I would like to thank Dr. A.Kirk, the WA102 spokesperson, who has never been too busy to answer to my questions very kindly and patiently. My special thanks must also go to Dr. A.Singovsky, the WA102 contactperson, who has given me a lot of crucial guidance. Without the help of these two persons my thesis would never have been completed.

I would like to express my great appreciation to Pr. T.Tsuru and Pr. K.Takamatsu, to Pr. J.P.Peigneux and Pr. J.P.Stroot for supporting me in my scientific activity in different periods. I will never forget the memory of Pr. Yu.Prokoshkin, who was my first supervisor in high energy physics and gave me an opportunity to participate in research on meson spectroscopy as a member of the WA102 Collaboration.

My thanks also go to my scientific supervisor from Russia, Dr. V.Obraztsov, and from France, Dr. J.P.Guillaud, who supported and advised me during this work.

I would also like to thank Dr. S.A.Sadovsky, who passed on to me his great experience in partial-wave analysis technique.

Many thanks to my friends and colleagues S.Slabospitsky, Yu.Gouz, D.Amelin, Yu.Khokhlov, A.Kurnosenko, O.Solovianov, A. and N. Emelyanenko, S.Sadilov, O. and. A. Karakulin, A. Vlasov and others who helped and advised me during my thesis.

My heart warmly thanks go to my family: my wife Svetlana, my mother Nelli and my brother Vladimir who gave countenance to me during the thesis.

Finally, my special thanks to my colleague from Scotland L.Haughney, who spent a lot of time reading the draft making language corrections to this thesis.

Thank you.

Bibliography

[1] S.Okubo Phys. Lett. **5** (1963) 165;
G.Zweig CERN-TH/401, 402, 412 (1964);
J.Iizuka *et al.* Prog. Theor. Phys. Suppl. **37-38** (1966) 21.

[2] S.N.Ganguli and D.P.Roy Phys.Rep. **67** (1980) 203.

[3] A.Kirk Phys. Lett. **B489** (2000) 29.

[4] D.Barberis *et.al.* Phys. Lett. **B422** (1998) 399;
D.Barberis *et.al.* Phys. Lett. **B427** (1998) 398;
D.Barberis *et.al.* Phys. Lett. **B432** (1998) 436;
D.Barberis *et.al.* Phys. Lett. **B436** (1998) 204;
D.Barberis *et.al.* Phys. Lett. **B440** (1998) 225;
D.Barberis *et.al.* Phys. Lett. **B446** (1999) 342;
D.Barberis *et.al.* Phys. Lett. **B453** (1999) 305;
D.Barberis *et.al.* Phys. Lett. **B453** (1999) 316;
D.Barberis *et.al.* Phys. Lett. **B453** (1999) 325;
D.Barberis *et.al.* Phys. Lett. **B462** (1999) 462;
D.Barberis *et.al.* Phys. Lett. **B467** (1999) 165;
D.Barberis *et.al.* Phys. Lett. **B471** (2000) 429;
D.Barberis *et.al.* Phys. Lett. **B471** (2000) 435;
D.Barberis *et.al.* Phys. Lett. **B471** (2000) 440;
D.Barberis *et.al.* Phys. Lett. **B474** (2000) 423;
D.Barberis *et.al.* Phys. Lett. **B479** (2000) 59;
D.Barberis *et.al.* Phys. Lett. **B484** (2000) 198;
D.Barberis *et.al.* Phys. Lett. **B485** (2000) 357;

D.Barberis *et.al.* Phys. Lett. **B488** (2000) 225.

[5] F.E.Close and A.Kirk Phys. Lett. **B397** (1997) 333.

[6] F.E.Close Phys. Lett. **B419** (1998) 387.

[7] F.E.Close Phys. Lett. **B419** (1998) 387;
P.Castoldi *et.al.* Phys. Lett. **B425** (1998) 359;
N.I.Kochelev, hep-ph/9902203;
N.I.Kochelev *et.al.* Phys. Lett. **B457** (1999) 202;
F.E.Close and G.Schuler Phys. Lett. **B458** (1999) 127.

[8] F.E.Close and G.Schuler Phys. Lett. **B464** (1999) 279.

[9] F.E.Close, A.Kirk and G.Schuler Phys. Lett. **B477** (2000) 13.

[10] C.Defoix *et al.* Phys. Lett. **B28** (1968) 353.

[11] R.Ammar *et al.* Phys. Rev. Lett. **21** (1968) 1832.

[12] R.Armenteros *et al.* Phys. Lett. **17** (1965) 344.

[13] R.Baldi *et al.* Phys. Lett. **B74** (1978) 413.

[14] M.J.Corden *et al.* Nucl. Phys. **B136** (1978) 77.

[15] T.Barnes Nucl. Phys. **B158** (1979) 171.

[16] J.Weinstein and N.Isgur Phys. Rev. **48** (1982) 659.

[17] F.E.Close and H.J.Lipkin Phys. Lett. **B196** (1987) 245.

[18] D.M.Alde *et al.* Yad. Phys. **59** (1996) 1027.

[19] D.M.Alde *et al.* Phys. Lett. **B205** (1988) 397.

[20] C.Caso *et al.* Eur. Phys. J. **C3** (1998) 1.

[21] G.M.Beladidze *et al.* Phys. Lett. **B313** (1993) 276.

[22] H.Aoyagi *et al.* Phys. Lett. **B314** (1993) 246.

[23] D.M.Alde *et al.* Phys.Atom.Nucl. **62** (1999) 421; Yad.Fiz. **62** (1999) 462.

[24] D.R.Thompson *et al.* Phys. Rev. Lett. **79** (1997) 1630.

[25] P.Eugenio for E852 Collaboration, Proc. of 7th Conf. on Intersections between Particle and Nuclear Physics, Canada, (2000) 233.

[26] G.S.Adams *et al.* Phys. Rev. Lett. **81** (1998) 5760.

[27] A.Abele *et al.* Phys. Lett. **B423** (1998) 175.

[28] A.Abele *et al.* Phys. Lett. **B446** (1999) 275.

[29] A.Amsler *et al.* Phys. Lett. **B333** (1994) 277.

[30] A.Abele *et al.* Eur. Phys. J. **C8** (1999) 67.

[31] S.F.Tuan *et al.* Phys. Lett. **B213** (1988) 537.

[32] M.J.Emms *et al.* Phys. Lett. **B58** (1975) 117.

[33] M.J.Corden *et al.* Nucl. Phys. **B144** (1978) 253.

[34] V.D.Apel *et al.* Yad. Phys. **31** (1980) 1967.

[35] Yu.D.Prokoshkin and S.A.Sadovsky Phys. Atom. Nucl. **58** (1995) 606.

[36] Yu.D.Prokoshkin and S.A.Sadovsky Phys. Atom. Nucl. **58** (1995) 853.

[37] S.A.Sadovsky Nucl. Phys. **A655** (1999) 131.

[38] D.Alde *et al.* KEK-Preprint-95-160; Talk at HADRON'95, Manchester, (1995) 454.

[39] A.C.Irving and R.P.Worden Phys. Rep. **34** (1977) 117.

[40] C.Zemach Phys. Rev. **140** (1964) 97 and 109.

[41] T.Barnes Nucl. Phys. **B224** (1983) 421.

[42] F.E.Close and P.R.Page Nucl. Phys. **B443** (1995) 233.

[43] T.Barnes Phys. Rev. **D25** (1995) 5242.

[44] P.Lacock *et al.* Nucl.Phys.Proc.Suppl. **73** (1999) 261;
C.Bernard *et al.* Nucl.Phys.Proc.Suppl. **73** (1999) 264.

[45] R.L.Jaffe Phys. Rev. **D15** (1977) 267.

[46] A.Abele *et al.* Phys. Lett. **B404** (1997) 179.

[47] D.Morgan Phys. Lett. **B51** (1974) 71.

[48] J.Weinstein and N.Isgur Phys. Rev. **D41** (1990) 2236.

[49] S.Ishida *et al.* Talk at HADRON'95, UK, (1995) 454.

[50] V.N.Gribov Lund preprints, LU-TP-91-7 and LU-TP-91-15 (1991).

[51] N.A.Tornqvist Phys. Rev. Lett. **49** (1982) 624.

[52] M.N.Achasov *et al.* Phys. Lett. **B438** (1998) 441.

[53] M.N.Achasov *et al.* Phys. Lett. **B440** (1998) 442.

[54] D.Antreasyan *et al.* Phys. Rev. **D33** (1986) 1847.

[55] T.Oest *et al.* Z. Phys. **C47** (1990) 343.

[56] L.Köpke and N.Wermmes Phys. Rep. **174** (1989) 67.

[57] M.N.Achasov Phys.Usp. **41** (1998) 1149; Usp.Fiz.Nauk **168** (1998) 1257

[58] N.N.Achasov and V.N.Ivanchenko Nucl. Phys. **B315** (1989) 465.

[59] N.N.Achasov and V.V.Gubin Phys. Rev. **D56** (1997) 4084.

[60] N.N.Achasov, S.A.Devyanin and G.N.Shestakov Phys. Lett. **B108** (1982) 134.

[61] V.M.Budnev and A.E.Kaloshin Phys. Lett. **B86** (1979) 351.

[62] T.Barnes Phys. Lett. **B165** (1985) 434.

[63] N.N.Achasov, V.V.Gubin and V.I.Shevchenko Phys. Rev. **D56** (1997) 203.

[64] I.J.R. Aitchison Nucl. Phys. **A417** (1972) 189.

[65] C.Amsler *et.al.* Phys. Lett. **B355** (1995) 425.

[66] A.Abele *et.al.* Phys. Rev. **D57** (1998) 3860.

[67] M.Boutemeur, J.P.Peigneux Nucl. Phys. (Proc. Suppl.) **B21** (1991) 1.

[68] R.Spighi for the OBELIX Collaboration Nucl. Phys. **A655** (1999) 35.

[69] P.Weidenauer *et al.* Z. Phys. **C47** (1990) 353.

[70] K.Maltman Phys. Lett. **B462** (1999) 14.

[71] D.Black *et.al.* Phys. Rev. **D61:074001** (2000).

[72] .Aderholz *et.al.* Phys. Lett. **10** (1964) 226.

[73] S.U.Chung and V.L.Korotkih BNL-Preprint BNL-QGS-99-401.

[74] A.Popov Private communication, work to be published soon.

[75] D.Amelin *et.al.* Yad. Phys. **62** (1999) 487.

[76] F.Antinori *et al.* Lett. Nuovo Cimento **A107** (1994) 1857.

[77] T.A.Armstrong *et al.* Nucl. Instr. and Meth. **A274** (1989) 165.

[78] F.Binon *et al.* Nucl. Instr. and Meth. **A248** (1986) 86.

[79] F.Binon *et al.* Nucl. Instr. and Meth. **A256** (1987) 444.

[80] J.C.Lassalle *et al.* Nucl. Instr. and Meth. **176** (1980) 371.

[81] A.A.Lednev Nucl. Instr. and Meth. **A366** (1995) 292.

[82] A.A.Lednev Preprint IFVE 93-153, Protvino (1993).

[83] A.B.Wicklund *et al.* Phys. Rev. **D17** (1978) 1197.

[84] G.Costa *et al.* Nucl. Phys. **B175** (1980) 402 .

[85] A.Etkin *et al.* Phys. Rev. **D25** (1982) 1786.

[86] R.S.Longacre *et al.* Phys. Lett **B177** (1986) 223.

[87] B.V.Bolonkin *et al.* Nucl. Phys. **B309** (1988) 426.

[88] S.U.Chung CERN Yellow Report, CERN 71-8, 1971.

[89] S.U.Chung and T.L.Trueman Phys. Rev **D 11** (1975) 633.

[90] S.A.Sadovsky IHEP 91-75, Protvno, 1991.

[91] S.U.Chung Phys.Rev. **D56** (1997) 7299.

[92] K.Gottfried and J.P.Jackson Nuovo Cim. **33** (1964) 309.

[93] L.D.Landau and E.M.Lifshits "Quantum mechanics" (in russian). Moskva, "Nauka", 1989.

[94] A.Gersten Nucl.Phys. **B12** (1969) 537.

[95] Eadie W.T. *et al.* Statistical Methods in Experimental Physics. North-Holl. Publ. Comp. Amsterdam–London, 1971.

[96] James F., Ross M. MINUIT (long writeup), CERN Program Library, D506, Geneva, 1987.

[97] V.S.Kurbatov, A.A.Tyapkin, "Background subtraction at estimation of parameters by the method of maximum of likelihood function" in "Statistical Methods in Experimental Physics" (in russian), Moskva, Atomizdat, 1976.

[98] T.Hino Doctor thesis, Department of Physics, Tohoku University, 1998.

[99] Svec M. Phys.Rev. **D53** (1996) 2343.

[100] K.L.Au, D.Morgan and M.R.Pennington Phys. Rev. **D35** (1987) 1633.

[101] A.Kondashov Doctor thesis, Institute for High Energy Physics, Protvino, 1997.

[102] F.E.Close and A.Kirk Phys.Lett. **B489** (2000) 24.

[103] N.N.Achasov, S.A.Devyanin and G.N.Shestakov Phys. Lett. **B88** (1979) 367.

[104] CMS Technical Proposal, CERN/LHCC 94-38, December 1994.

[105] A.Duccio The Tracker Layout, http://cern.ch/duccio/layout/whole.html

[106] CMS "The Tracker Project. Technical Design Report", CERN/LHCC 98-6, April 1998.

[107] CMS "The Electromagnetic Calorimeter Project. Technical Design Report", CERN/LHCC 97-33, December 1997.

[108] CMS "The Hadron Calorimetr Project. Technical Design Report", CERN/LHCC 97-31, June 1997, Fig. 1.43, p.60.

[109] CMS Internal Note/1996-003.

[110] TOTEM "Letter of Intent", CERN/LHCC 97-49, August 1997.

[111] TOTEM Technical Proposal, CERN/LHCC 99-7, March 1999.

[112] S.Abdullin *et.al.* CMS TN/1994-180.

[113] R.Brun *et.al.* Geant 3 User Guide, CERN DD/EE/84-1, 1986.

[114] C.Charlot *et.al.* CMS TN/1993-63.

[115] S.Abdullin Talk at "Fast MC CMS Workshop", April, 2001.

[116] T.Sjöstrand Computer Physics Commun. **82** (1994) 74.

[117] F.Paige and S.Protopopescu in Supercollider Physics, p. 41, ed. D. Soper (World Scientific, 1986); H.Baer, F.Paige, S.Protopopescu and X.Tata, in Proceedings of the Workshop on Physics at Current Accelerators and Supercolliders, ed. J.Hewett, A.White and D.Zeppenfeld (Argonne National Laboratory, 1993).

[118] G.Marchesini *et.al.* Computer Physics Commun. **67** (1992) 465.

[119] G.Grindhammer *et.al.* SLAC-PUB-5072, Nucl.Instrum.Meth. **A290** (1990) 469.

[120] G.Schuler and T.Sjöstrand Phys.Rev. **D49** (1994) 2257-2267.

[121] A.Donnachie and P.V.Landshoff Nucl.Phys. **B267** (1986) 690.